Discovery of non-zero neutrino mixing angle θ_{13} using Daya Bay Antineutrino Detectors

Thesis by

Raymond Hei Man Tsang

In Partial Fulfillment of the Requirements

for the Degree of

Doctor of Philosophy

California Institute of Technology

Pasadena, California

2013

(Defended May 28, 2013)

Acknowledgments

First of all I would like to thank every one of my collaborators - it is their blood, sweat and caffeine, which made this experiment a great success and this thesis possible.

I am indebted to my advisor Bob McKeown who gave me the opportunity to take part in this journey of scientific discovery. It has been a unique experience from which I will benefit over the rest of my life. I am also thankful to Jianglai Liu for his teaching and guidance since the day I joined the group, and for serving as my role model. I also owe Dan Dwyer my thanks for his generous help and useful advice on many aspects. I also need to thank Xin Qian for helping me through in the writing of this thesis. My thanks also go to Chao Zhang, Fenfang Wu, Wei Wang, and Jiajie Ling from whom I have learnt a lot.

During my stay at Daya Bay, the patience shown by Gaosong Li, Wenqiang Gu, and Bob Carr in working with me is what I must appreciate. Let me also thank Daniel Ngai, Joseph Hor, Yue Meng, Shih-Kai Lin, Bei-Zhen Hu, Yung-Shun Yeh, Raymond Kwok, Xiaocong Chen, our driver Jun Liu, and many others for making my stay at Daya Bay much more pleasant. I would also like to thank the "Daya Bay youth group". Without them, I might never know what *baijiu* is.

I appreciate all my friends at Caltech, especially those of HKSA, for keeping me company and sane. I would also like to express my gratitude to my former and current roommates: Heywood Tam, Benjamin Li, Kawai Kwok, Michio Inoue, and Reed Scharff for tolerating my irregular sleep-wake hours and the mess I leave all over the place.

I must thank my family for giving me strength despite all the things that have happened while I was away from home. Finally, I want to give my most heartfelt thanks to my parents and my brother for all of their love and support.

Abstract

The Daya Bay Reactor Antineutrino Experiment observed the disappearance of reactor $\bar{\nu}_e$ from six 2.9 GW_{th} reactor cores in Daya Bay, China. The Experiment consists of six functionally identical $\bar{\nu}_e$ detectors, which detect $\bar{\nu}_e$ by inverse beta decay using a total of about 120 metric tons of Gd-loaded liquid scintillator as the target volume. These $\bar{\nu}_e$ detectors were installed in three underground experimental halls, two near halls and one far hall, under the mountains near Daya Bay, with overburdens of 250 m.w.e, 265 m.w.e and 860 m.w.e. and flux-weighted baselines of 470 m, 576 m and 1648 m. A total of 90179 $\bar{\nu}_e$ candidates were observed in the six detectors over a period of 55 days, 57549 at the Daya Bay near site, 22169 at the Ling Ao near site and 10461 at the far site. By performing a rate-only analysis, the value of $sin^2 2\theta_{13}$ was determined to be 0.092 ± 0.017.

Contents

List of Figures

List of Tables

Chapter 1

Introduction

The neutrino is among the most intriguing fundamental particles. Over fifty years since its discovery, some of its properties are known while many mysteries still remain. In this chaper, I will discuss the current knowledge about the neutrino, and then I will briefly summarize previous endeavors of understanding this elusive particle, and describe the role of the Daya Bay reactor antineutrino experiment in this big puzzle.

1.1 The Theory of the Neutrino

In the Standard Model of particle physics, the neutrino is a neutral fermion with spin $\frac{1}{2}$. Being electrically neutral, the neutrino does not interact electromagnetically nor through strong interaction. It only interacts weakly[1], through the coupling with $W^{\pm}$ (charged current) and Z^0 (neutral current). Therefore, neutrinos can only be detected through the feeble weak interaction. This is why the neutrino is considered elusive. The neutrino comes in three flavors [36], the electron neutrino (ν_e), the muon neutrino (ν_μ) and the tau neutrino (ν_τ). They form doublets with their respective charged lepton counterparts:

$$\begin{pmatrix} e^- \\ \nu_e \end{pmatrix}, \begin{pmatrix} \mu^- \\ \nu_\mu \end{pmatrix}, \begin{pmatrix} \tau^- \\ \nu_\tau \end{pmatrix}.$$

Each pair can be assigned a lepton number corresponding to its flavor: the particle is assigned +1 while the antiparticle is assigned -1. The Standard Model asserts that each of these flavor lepton

[1] Also gravitationally, but only does so extremely feebly.

numbers is always individually conserved.

The neutrinos are prescribed as massless in the Standard Model, which implies that they always travel at the speed of light. However, neutrino oscillation experiments over the decades have provided strong evidence against a massless neutrino. In the following sections, I will describe some implications of a massive neutrino, loosely following the discussions in [1] and [37].

1.1.1 The Massive Neutrino

1.1.1.1 Majorana or Dirac

For charged particles, their antiparticles always have opposite charge. Since the neutrino is neutral, it is possible for the neutrino to be its own antiparticle. In such a case, the neutrino would be called a Majorana particle, otherwise a Dirac particle. A particle's antiparticle partner is its CPT conjugate, meaning that by applying charge conjugation (C), parity (P) and time reversal (T) operators to the particle, one gets the antiparticle. Suppose we have a left-handed neutrino (ν_L) and we apply CPT conjugation on it. We will get a right-handed antineutrino ($\bar{\nu}_R$). (As an empirical fact, only left-handed neutrinos and right-handed antineutrinos have ever been observed.) On the other hand, since the neutrino is massive, there exists an inertial reference frame which travels at a higher speed than ν_L. In such a reference frame, ν_L would appear to be traveling backwards. However, since the spin direction is unchanged by this change of reference frames (or Lorentz boost), the helicity would change from left-handed to right-handed, and we get a right-handed neutrino (ν_R). Now, are ν_R and $\bar{\nu}_R$ the same particle? If they are the same particle, then we have Majorana neutrinos. This means that the neutrino and "antineutrino" that we are seeing are simply neutrinos in two different helicity states (ν_L and ν_R). If they are distinct particles, then we have Dirac neutrinos. In this case, we can apply CPT conjugation to ν_R, obtaining its antiparticle the left-handed antineutrino ($\bar{\nu}_L$). So, we would have four distinct states (ν_L ν_R, $\bar{\nu}_L$ and $\bar{\nu}_R$). This is illustrated in Figures 1.1 and 1.2.

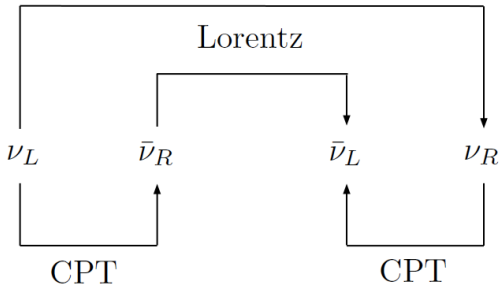

Figure 1.1: The four distinct states of a Dirac neutrino (adapted from [1]).

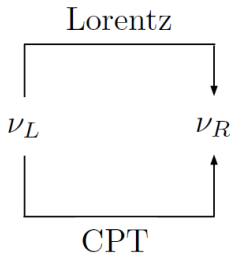

Figure 1.2: The two distinct states of a Majorana neutrino (adapted from [1]).

1.1.1.2 Neutrino Oscillation

Another phenomenon enabled by non-zero neutrino mass is neutrino oscillation. As mentioned earlier, lepton numbers for each flavor are conserved individually. Direct violation has never been observed. However, if neutrinos of various flavors are, in fact, superpositions of different mass eigenstates, neutrino oscillation become possible. Mathematically,

$$\mid \nu_l \rangle = \sum_i U_{li} \mid \nu_i \rangle$$

where $\mid \nu_l \rangle$ is the flavor eigenstate for the neutrino corresponding to lepton l, $\mid \nu_i \rangle$ is the ith mass eigenstate and U_{li} specifies the composition of the ith mass eigenstate in the lepton l eigenstate. The unitary matrix $\mathbf{U} = (U_{li})$ is known as the Pontecorvo-Maki-Nakagawa-Sakata (PMNS) matrix, or simply, the mixing matrix. As the neutrino propagates, the relative compositions of the mass eigenstates will change as the mass eigenstates propagate differently:

$$\mid \nu_{final} \rangle = \sum_i U_{li} e^{-iE_i t} \mid \nu_i \rangle$$

The probability that the neutrino after propagation to be detected as the original flavor can be calculated as:

$$P(\nu_l \to \nu_l) = |\langle \nu_l \mid \nu_{final} \rangle|^2 = |\sum_i U_{li}^* U_{li} e^{-iE_i t}|^2 < 1$$

This gives rise to neutrino oscillation. Notice that if neutrinos were all massless or had the same mass, E_i would be all equal and hence $P(\nu_l \to \nu_l) = 1$ (i.e. no oscillation) since $\mathbf{U}$ is unitary. Thus, neutrino oscillation occurs only if neutrinos have mass.

Currently, the model with 3 flavors and 3 mass eigenstates best describe observed data. Such a model is described by a 3x3 mixing matrix $\mathbf{U}$ which is often decomposed into four matrices as follows:

$$U = \begin{pmatrix} 1 & 0 & 0 \\ 0 & c_{23} & s_{23} \\ 0 & -s_{23} & c_{23} \end{pmatrix} \begin{pmatrix} c_{13} & 0 & s_{13}e^{-i\delta} \\ 0 & 1 & 0 \\ -s_{13}e^{-i\delta_{CP}} & 0 & c_{13} \end{pmatrix} \begin{pmatrix} c_{12} & s_{12} & 0 \\ -s_{12} & c_{12} & 0 \\ 0 & 0 & 1 \end{pmatrix}$$

$$\times \begin{pmatrix} e^{-i\alpha_1/2} & 0 & 0 \\ 0 & e^{-i\alpha_2/2} & 0 \\ 0 & 0 & 1 \end{pmatrix}$$

where $s_{ij} = \sin\theta_{ij}$, $c_{ij} = \cos\theta_{ij}$; θ_{ij} are the mixing angles, δ_{CP} is the CP violating phase and α_i are the Majorana phase factors. Also relevant to neutrino oscillation are $\Delta m_{ij}^2 = m_i^2 - m_j^2$, the difference between the neutrino masses squared, also known as mass splittings. The ordering of the neutrino masses is referred to as the mass hierarchy. Under the current understanding of the mixing parameters, there are two possible mass hierarchies: normal ($m_1 < m_2 < m_3$) or inverted ($m_3 < m_1 < m_2$).

Matter effect The discussion above describes neutrino oscillation in vacuum. However, when neutrinos propagate through matter, their interactions with matter will modify the effects of neutrino oscillation. This is referred to as Mikheyev-Smirnov-Wolfenstein effect (MSW effect) or matter effect [1, 38].

Matter is made of quarks and electrons. As neutrinos propagates in matter, they interact with these particles through the neutral current (Z^0) or the charged current ($W^{\pm}$). Muon neutrinos and tau neutrinos interact with quarks and electrons only through the neutral current, which is identical for all flavors. However, in addition to the neutral current, electron neutrinos also interact with electrons through the charged current. This asymmetry would skew the apparent mixing angle and mass splitting. In the two-flavor scenario,

$$\Delta m^2_M = \Delta m^2 \sqrt{sin^2 2\theta + (cos2\theta - x)^2} \text{ and}$$
$$sin^2 2\theta_M = \frac{sin^2 2\theta}{sin^2 2\theta + (cos2\theta - x)^2}$$

where

$$x \equiv \pm \frac{2\sqrt{2} G_F N_e E}{\Delta m^2}$$

(positive sign for neutrinos and negative sign for antineutrinos), G_F is the Fermi coupling constant, N_e is the electron density in the material, E is the energy of the neutrino and the parameters with subscript M are the in-matter (effective) versions of their respective in-vacuum counterparts [39].

Not only does matter effect distort mixing angles and mass splitting, it also affects meausurements of δ_{CP} [39]. The CP-violating phase δ_{CP} describes the intrinsic difference between the neutrino and the antineutrino with regard to propagation. When describing the antineutrino, the matter effect parameter x defined in the previous paragraph would have an opposite sign compared to the neutrino. This would result in different Δm^2_M and θ_M than in the neutrino case, thereby creating an apparent CP-violation even when there is none.

However, the matter effect is relevant only when the electron density is high or when the neutrino energy is high. The strength of the matter effect depends on the parameter x which can be approximated as,

$$x = \begin{cases} \dfrac{E \times n}{0.5 \text{ GeV}} & \text{for solar mixing } (\Delta m^2 = \Delta m^2_{12} \sim 7.59 \times 10^{-5} eV^2) \\ \dfrac{E \times n}{16 \text{ GeV}} & \text{for atmospheric mixing } (\Delta m^2 = \Delta m^2_{23} \sim 2.43 \times 10^{-3} eV^2) \end{cases}$$

where n is the electron number density in units of the Avogadro's number.

Given that the typical energy of an antineutrino from a nuclear reactor (such as the case for Daya Bay) is in the order of several MeV and $n \sim 1$, $x \ll 1$. Matter effect is therefore negligible. While for the center of the sun, since n can be as high as 100 [40], matter effect becomes important in this regime.

1.2 A Brief History of the Neutrino

1.2.1 From Postulation to Discovery

The story of the neutrino began in 1914, when Chadwick [41] discovered that the energy spectrum of the electron produced in a beta decay is in fact a continuum, despite the discrete energy levels expected of the nucleus. Pauli proposed in 1931 that along with the electron, a neutral, highly penetrating particle is also emitted, which carries a variable fraction of the total decay energy, which can produce a continuum. Built upon Pauli's hypothesis, in 1933, Fermi [42, 43] formulated the theory of beta decay and named this "invisible" particle the neutrino.

Two decades later, in 1953, Reines and Cowan [44] attempted to detect antineutrinos ($\bar{\nu_e}$) produced by the Hanford nuclear reactor using a 300-liter tank of cadmium loaded scintillator equipped with photomultiplier tubes (PMTs). *Herr Auge*, as the detector was nicknamed, made use of inverse beta decay to detect antineutrinos from the reactor:

$$\bar{\nu_e} + \mathrm{p} \rightarrow \mathrm{e}^+ + \mathrm{n}$$

The positron would annihilate, producing two 0.511 MeV gamma rays, while the neutron would be captured by some cadmium nucleus, emitting some gamma rays with a total energy of about 9 MeV. The positron and the neutron signals would form a clear timing signature. Unfortunately, due to the high background rate, they didn't produce convincing proof of the existence of the (anti-)neutrino. In 1956, Reines and Cowan [45] made a second attempt at the Savannah River nuclear facility. This time, they used, as detectors, a total of 4200 liters of scintillator separated in three layers and two layers of cadmium loaded water as targets inserted in between (like a Big Mac), as shown in Figure 1.3. With better background suppression, convincing evidence for the existence of

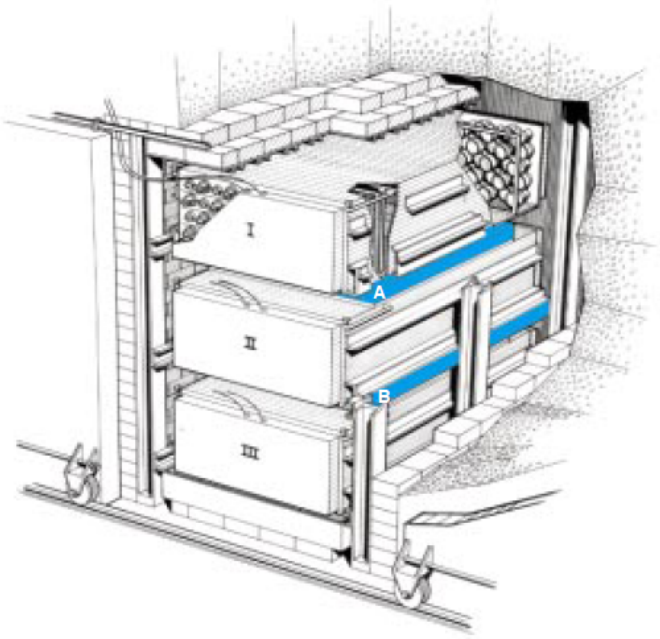

Figure 1.3: Savannah River neutrino detector [2]

the (anti-)neutrino was finally found. [45]

1.2.2 Missing Neutrinos from the Sun

The sun produces energy predominantly by nuclear fusion of protons, known as proton-proton cycle (*pp*). The *pp* cycle consists of several steps. First, two protons are fused into deuterium, giving a positron and a neutrino in addition to some energy:

$$\mathrm{p} + \mathrm{p} \rightarrow \mathrm{D} + \mathrm{e}^{+} + \nu_e + 0.42 \text{ MeV}$$

The deuterium nucleus would then combine with another proton to become ^{3}He:

$$\mathrm{D} + \mathrm{p} \rightarrow {}^3\mathrm{He} + \gamma + 5.49 \text{ MeV}$$

From here, ^{4}He would be produced via four possible branches, some of which would produce additional neutrinos. Table 1.1 shows the neutrino fluxes from various recent solar models, and Figure 1.4 shows the neutrino energy spectrum predicted by the solar model BS05(OP).

In the late 1960s, Davis, motivated by Bahcall's calculations, attempted to detect these solar neutrinos with 380 m^3 of tetrachloroethlyene (CCl_2=CCl_2), a common dry cleaning fluid. They placed

Model	pp	pep	hep	^{7}Be	^{8}B	^{13}N	^{15}O	^{17}F
BP04(Yale)	5.94	1.40	7.88	4.86	5.79	5.71	5.03	5.91
BP04(Garching)	5.94	1.41	7.88	4.84	5.74	5.70	4.98	5.87
BS04	5.94	1.40	7.86	4.88	5.87	5.62	4.90	6.01
BS05(^{14}N)	5.99	1.42	7.91	4.89	5.83	3.11	2.38	5.97
BS05(OP)	5.99	1.42	7.93	4.84	5.69	3.07	2.33	5.84
BS05(AGS,OP)	6.06	1.45	8.25	4.34	4.51	2.01	1.45	3.25
BS05(AGS,OPAL)	6.05	1.45	8.23	4.38	4.59	2.03	1.47	3.31

Table 1.1: Neutrino fluxes from seven solar models [3]. The units are 10^{10}(pp), 10^{9}(^{7}Be), 10^{8}(pep, ^{13}N,^{15}O), 10^{6}(^{8}B,^{17}F), and 10^{3}(hep) $cm^{-2}s^{-1}$.

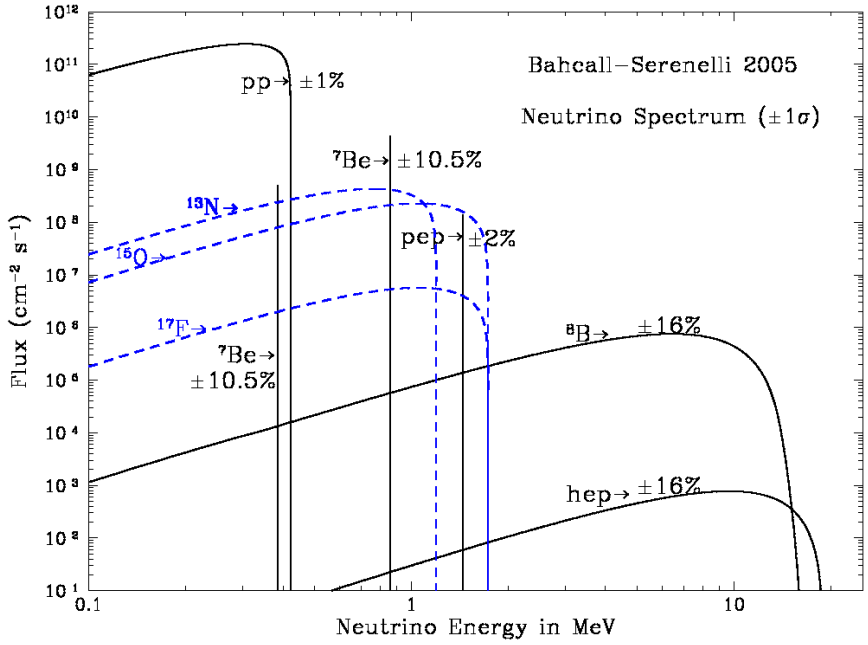

Figure 1.4: Neutrino energy spectrum predicted by the solar model BS05(OP). [3]

it 1478 m underground in the Homestake mine [46] to shield against cosmic radiations. Chlorine nuclei in the chemical could capture neutrinos, converting into a radioactive isotope of argon.

$$^{37}\mathrm{Cl} + \nu_e \rightarrow {}^{37}\mathrm{Ar} + \mathrm{e}^-$$

The number of detected neutrinos can be deduced by counting the number of ^{37}Ar atoms in the periodically drawn samples from the detector. However, they only detected about one third of what the Standard Solar Model predicted. This is known as the solar neutrino problem.

1.2.3 Confirmations of the Solar Neutrino Deficit

There were three possible explanations for such discrepancy:

1. The prediction of the solar model was not accurate.
2. Detector calibrations were flawed.
3. The behavior of the neutrino was not fully understood.

In fact, the Homestake experiment was sensitive only to a tiny fraction of solar neutrinos. The threshold for neutrino capture on ^{37}Cl is 0.814 MeV which lies above the endpoint energy of the *pp* cycle, as seen in Figure 1.4. In order to increase the fraction of detectable neutrinos, the next generation of experiments in the 1990s made use of ^{71}Ga which can capture neutrinos in a similar manner:

$$^{71}\mathrm{Ga} + \nu_e \rightarrow {}^{71}\mathrm{Ge} + \mathrm{e}^-$$

but with a lower energy threshold of 0.233 MeV, so that *pp* neutrinos could also be detected. The SAGE experiment (Soviet-American Gallium Experiment) located in Baksan, Russia used metallic gallium as the target, whereas the GALLEX experiment (GALLium EXperiment) in LNGS (Laboratori Nazionali del Gran Sasso), Italy chose gallium trichloride-hydrochloric acid solution ($GaCl_3$) as detector. These two experiments were consistent with each other, but both measured only about one half of the neutrino flux predicted by the solar model. Inaccurate solar model still remained a possibility. In 1994, GALLEX used a ^{51}Cr neutrino source to calibrate the their detector and found

that it measured 97% ± 11% of the expected neutrino rate. This suggested that imperfections in detector calibration could not account for the discrepancy. The puzzle then became whether our understanding about the sun was wrong, or our understanding about the neutrino was. (Of course, in hindsight, we know the culprit was the neutrino.)

1.2.4 Searches on the Reactor Front

Over the years, measurements of reactor antineutrinos were also made in order to look for neutrino oscillation. On the other hand, they could also see if there were similar deficits, which could provide clues to the solar neutrino problem.

1.2.4.1 Institut Laue-Langevin and Gösgen

In the late 1970s at Institut Laue-Langevin (ILL), a scintillator and ^{3}He based detector was built [4]. It aimed to detect the antineutrinos generated by a 57 MW fission reactor 8.76 m away. The inverse beta decay reaction was used for detecting antineutrino: $\bar{\nu}_e$ + p $\rightarrow$ n + e^+. However, the observed flux was consistent with the expected flux with no oscillation. Later, the upgraded ILL detector was relocated to Gösgen, which was home to a much more powerful reactor with $2.8 GW_{th}$ [47]. Measurements were made at three different distances (37.9 m, 45.9 m and 64.7 m) from the reactor. All were consistent with the no oscillation scenario.

1.2.4.2 Rovno

Using a detector consisted of Gd-loaded scintillator, measurements of the antineutrino flux was made at the Rovno nuclear power plant in 1987 [48]. The antineutrino flux were measured at 18 m and 25 m from the core. These results were combined as one measurement, and was consistent with the no oscillation scenario. Another measurement involved two separate detectors placed at 12 m and 18 m from the core [49]. Reactor-related uncertainties can be reduced by looking at the relative rates at the two detectors. However, the result was still consistent with no oscillation.

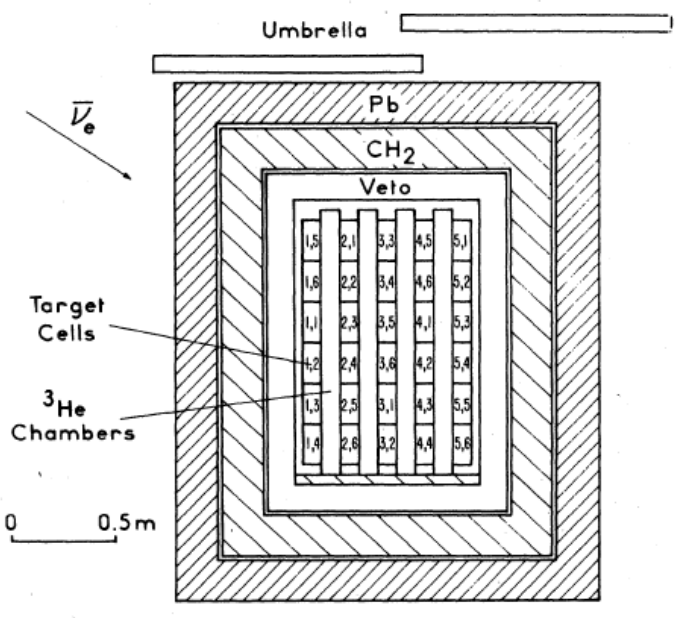

Figure 1.5: ILL and Gösgen detector [4]

1.2.4.3 Bugey

To further reduce systematic uncertainties, the Bugey experiment used three identical detectors, consisting of 600 liters of ^{6}Li-loaded liquid scintillator, to detect antineutrinos produced by a $2800 MW_{th}$ reactor. One detector was placed at 15 m from the core, the other two at 40 m [50, 51]. The ^{6}Li was used to detect the delayed neutron:

$$\mathrm{n} + {}^6Li \rightarrow {}^4He + {}^3H + 4.8 \text{ MeV}$$

Although Bugey accumulated much higher statistics than the previous experiments, no breakthrough was seen: the result was consistent with no oscillation.

1.2.4.4 Krasnoyarsk

The Krasnoyarsk experiment [5] used 513 liters of water/heavy water as antineutrino target and ^{3}He filled proportional tubes were used for neutron detection. The detector was placed 34 m from the Krasnoyarsk reactor under an overburden of 600 m.w.e. Water (H_2O) was used in the first (testing) phase. Since only neutrons were detected, the detector was sensitive only to charged current events:

$$\bar{\nu}_e + \mathrm{p} \rightarrow \mathrm{n} + e^+ \text{ (CC)}$$

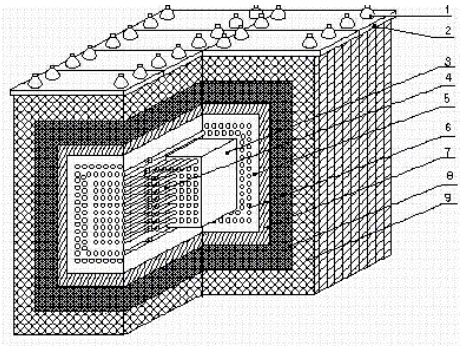

Figure 1.6: Krasnoyarsk detector [5]. 1: photomultipliers, 2: muon veto system, 3: tank with water (target), 4: proportional counters, 5: Teflon, 6: channel for counters, 7: steel shots, 8: graphite, 9: boron polyethylene.

In the second phase, heavy water (D_2O) was used. Now both charged current and neutral current events could be seen by the detector, and were discriminated by neutron multiplicity.

$$\bar{\nu}_e + \mathrm{d} \rightarrow \mathrm{n} + \mathrm{n} + e^+ \text{ (CC)}$$

$$\bar{\nu}_e + \mathrm{d} \rightarrow \mathrm{p} + \mathrm{n} + \bar{\nu}_e \text{ (NC)}$$

The results of both phases were consistent with theoretical calculations assuming no oscillation.

1.2.5 On the Verge of Discovery

Over the decades, reactor based experiment did not show any solid evidence of neutrino oscillation. Using kiloton scale detectors, the search continued on the solar frontier. These experiments were eventually proven to be fruitful.

1.2.5.1 Kamiokande

Kamiokande (Kamioka Nucleon Decay Experiment) was a 2.14-kt water Cherekov detector placed 1 km underground, originally intended for proton decay studies [52, 53]. However, it was later realized that it could be used to detect solar neutrinos. Neutrinos from the sun can elastically scatter on the electrons and the recoiled electron would produce Cherenkov radiation that could be observed.

$$\nu_x + e^- \rightarrow \nu_x + e^-$$

Kamiokande's huge volume means that it can capture a far greater number of neutrinos than previous experiments. Besides, neutrinos could now be studied event-by-event, which was not possible in previous radiochemical experiments. Unfortunately, the 2079-day worth of data Kamiokande took between 1987 and 1995 showed only about one half of the flux predicted by the standard solar model [53], and hence it did not resolve the solar neutrino problem. One important limitation of Kamiokande was that although neutrinos of all flavors can elastically scatter on electrons, their cross-sections were different [54], so there was no easy way to deduce the total number of neutrinos of any flavor. Moreover, it could only detect neutrinos of energy above 7 MeV due to background radiation, therefore only a tiny fraction of the solar neutrinos could be observed.

Kamiokande was also sensitive to atmospheric neutrinos. Using the technique of "ratio of ratios" (See Section 1.2.5.4 below), the atmospheric neutrino rate was observed to be less than theoretical prediction. This was known as the atmospheric neutrino anomaly.

1.2.5.2 CHOOZ

The CHOOZ experiment [6, 55] aimed to tackle the atmospheric neutrino anomaly using reactor neutrinos: an absence of $\bar{\nu_e}$ deficit would indicate that $\nu_\mu \leftrightarrow \nu_e$ oscillation is not the dominant cause of the anomaly.

Previous reactor based experiments typically had shorter baselines (detector-reactor distance < 100 m). In order to probe longer baselines while maintaining decent statistics, detectors with a larger target mass or more powerful reactors were needed. CHOOZ had both. The CHOOZ experiment used a detector consisting of 5 ton Gd loaded liquid scintillator. It was located 1 km from two reactors with a total thermal power of 8.5 GW. The detector was placed underground with an overburden of 300 m.w.e. to reduce the effects of cosmogenic background.

Over the 8210 hours of data-taking which included times with 0, 1 or 2 reactors running, 2991 neutrino events were seen. The result showed good agreement with the expected spectrum assuming no oscillation. This removed the possibility of explaining the atmospheric neutrino anomaly by $\nu_\mu \leftrightarrow \nu_e$ oscillations.

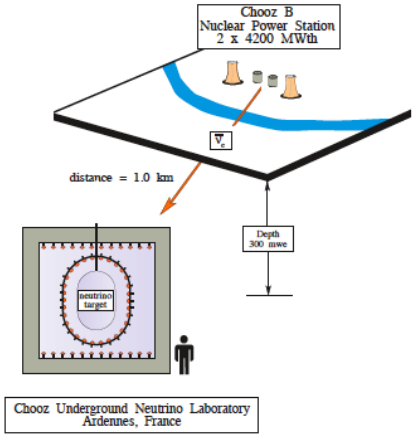

Figure 1.7: Location of CHOOZ detector and reactor [6].

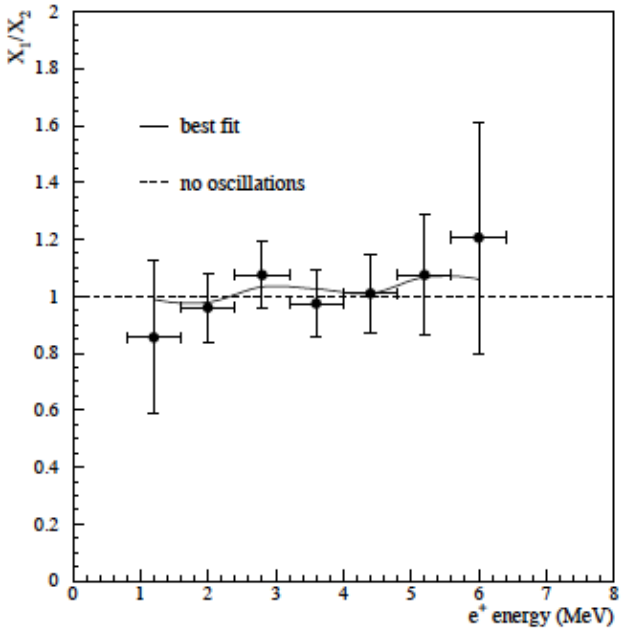

Figure 1.8: The CHOOZ result showed good agreement with expected positron spectrum [6].

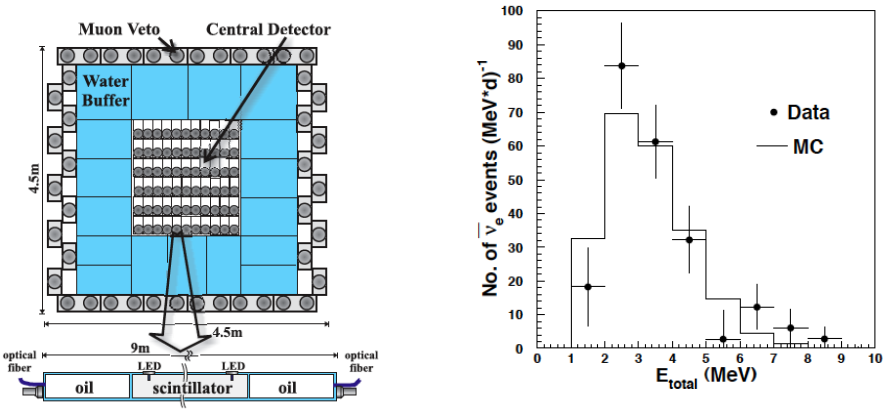

Figure 1.9: The left shows the Palo Verde detector, and the right shows the result by Palo Verde [7].

1.2.5.3 Palo Verde

Similar to CHOOZ, the Palo Verde experiment [7, 56, 57] also aimed to tackle the atmospheric neutrino anomaly. The Palo Verde experiment had a more powerful antineutrino source than CHOOZ and used an even bigger detector. The experiment was located near the Palo Verde Nuclear Generating Station in Arizona which was home to three reactors with a total thermal power of 11.6 GW. The Palo detector was a 11.34 ton detector consisting of Gd loaded liquid scintillator, placed at 750 m from one reactors and 890 m from the other two. After analyzing 350 days worth of data, no evidence of neutrino oscillation was found. This indicates that $\nu_\mu \leftrightarrow \nu_e$ oscillations was not responsible for the atmospheric neutrino anomaly.

1.2.5.4 Super-Kamiokande

Being the successor of Kamiokande, Super-Kamiokande (Super-K) was a scaled up version of Kamiokande, consisting of 50 kt ultra-pure water located 1 km underground [8, 58, 59, 60, 61, 62]. Although the energy threshold had been lowered to 5 MeV, Super-K suffered from the problem of unequal sensitivity to neutrino of different flavors, like Kamiokande. Super-K measured about a half of the expected flux.

In addition to solar neutrinos, Super-K was also sensitive to atmospheric neutrinos produced by cosmic rays. Atmospheric neutrinos can, for example, be produced in the following way:

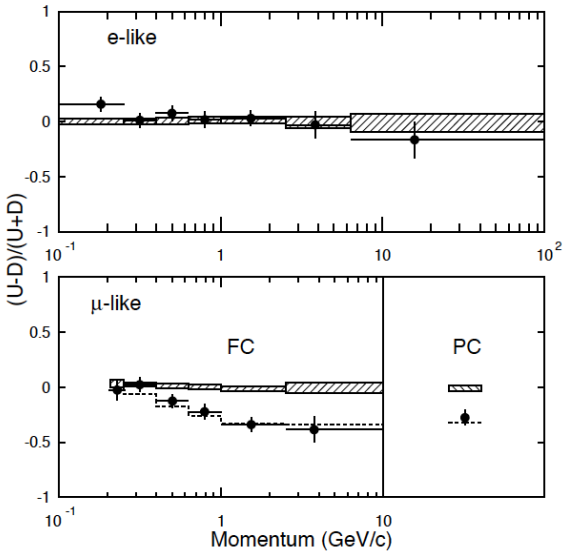

Figure 1.10: Up-down asymmetry in neutrino flux observed by Super-K [8].

$$\pi^+ \rightarrow \mu^+ + \nu_\mu$$

$$\mu^+ \rightarrow \mathrm{e}^+ + \bar{\nu}_\mu + \nu_e$$

A neutrino of flavor l can produce its corresponding lepton upon interaction with a nuclei ${}^A_Z X$ in the detector:

$$\nu_l + {}^A_Z X \rightarrow l^- + {}^A_{Z+1} X$$

$$\bar{\nu}_l + {}^A_Z X \rightarrow l^+ + {}^A_{Z-1} X$$

Therefore, the flavor of the incoming neutrino could be deduced by identifying the resulting charged lepton. The ratio of detected $\bar{\nu}_\mu + \nu_\mu$ to $\bar{\nu}_e + \nu_e$, N_μ/N_e, was compared with the expected ratio predicted by Monte Carlo simulation, forming the following "ratio of ratios" R.

$$R = \frac{(N_\mu/N_e)_{data}}{(N_\mu/N_e)_{MC}}$$

This ratio R was found to be significantly smaller than 1. To investigate, they looked into the up-down asymmetry of $\bar{\nu}_\mu + \nu_\mu$ and $\bar{\nu}_e + \nu_e$ flux. It was found that the up-down asymmetry of the μ-like events deviated significantly from 0.

This data was found to be consistent with a two-flavor ($\nu_\mu \leftrightarrow \nu_\tau$) oscillation model with parameters ($sin^2 2\theta = 1.0$, $\Delta m^2 = 2.2 \times 10^{-3} eV^2$). This was the first convincing evidence for the existence

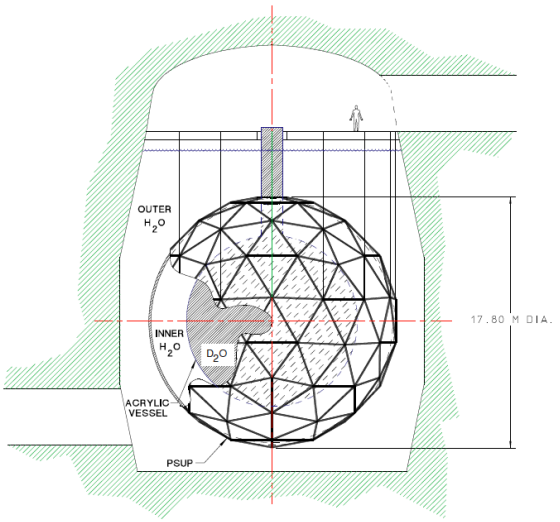

Figure 1.11: The Sudbury Neutrino Observatory detector [9].

of neutrino oscillation. This also strongly suggest that the atmospheric neutrino anomaly is due to $\nu_\mu \leftrightarrow \nu_\tau$ oscillations (assuming no sterile neutrinos).

1.2.5.5 Sudbury Neutrino Observatory (SNO)

The breakthrough to the solar neutrino problem came in 2002 from the Sudbury Neutrino Observatory (SNO) [9, 10, 63, 64, 65, 66]. SNO used 1 kt D_2O placed at a depth of about 6 km water equivalent. SNO detected neutrinos using three reactions:

$$\nu_e + \mathrm{d} \rightarrow \mathrm{p} + \mathrm{p} + e^- \text{ (CC)}$$

$$\nu_x + \mathrm{d} \rightarrow \mathrm{p} + \mathrm{n} + \nu_x \text{ (NC)}$$

$$\nu_x + e^- \rightarrow \nu_x + e^- \text{ (ES)}$$

The charged current (CC) reaction is sensitive only to electron neutrinos. Both the neutral current (NC) reaction and elastic scattering (ES) are sensitive to all three flavors. While elastic scattering has different sensitivities to neutrinos of different flavors, neutral current reaction is equally sensitive to all three flavors. Therefore, the neutral current channel serves as a unique tool for testing whether solar neutrinos oscillate. In 2002, SNO observed a 5.3σ excess of non-electron neutrino, and the total number of observed neutrinos of all flavors agreed with the prediction of the standard solar model as shown in Fig 1.12. This resolved the solar neutrino problem by confirming that solar neutrinos

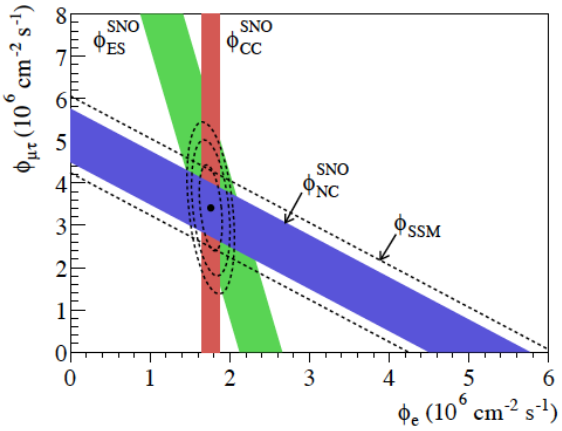

Figure 1.12: The final result from the Sudbury Neutrino Observatory detector showing agreement between the total neutrino flux detected through the neutral current channel and the flux predicted by the Standard Solar Model [10].

undergo flavor transformation, which can be interpreted as the result of neutrino oscillation, and suggested that the standard solar model was accurate.

1.2.6 Precision Era

After the discovery of some convincing evidence for the neutrino oscillation phenomenon, the natural next step was to perform precise measurements on the neutrino mixing parameters which characterize the phenomenon. Two of the three mixing angles (θ_{12} and θ_{23}) and the two mass splittings were the first to be precisely measured.

1.2.6.1 Solar Mixing Angle θ_{12} and Mass Splitting Δm^2_{12}

A global analysis [11] which included data from Homestake, SAGE, GALLEX/GNO, Kamiokande and Super-Kamiokande, suggested four regions where the oscillation parameters (Δm^2_{12}, θ_{12}) were likely to be found (Table 1.2). KamLAND aimed at probing the so-called LMA region which was considered to be the most promising (as shown in Figure 1.13).

KamLAND was charged to measure δm^2 and $tan^2\theta_{12}$. KamLAND consists of a 1 kt liquid scintillator enclosed in a 13 m diameter balloon, placed among 55 reactor cores with an average distance of 180 km, under an overburden of 2700 m.w.e. [13, 14, 67, 68]. KamLAND used the inverse

Solution	δm^2 $[eV^2]$	$tan^2\theta_{12}$	χ^2_{pull}	$\Delta\chi^2_{pull}$
LMA	5.5×10^{-5}	0.42	73.4	0 (global minimum)
LOW	7.3×10^{-8}	0.67	83.8	10.4
QVO	6.5×10^{-10}	1.33	81.2	7.8
SMA	5.2×10^{-6}	1.1×10^{-3}	96.9	23.5

Table 1.2: Position and values of the global minimum (LMA) and three local minima (LOW, QVO, SMA). [11]

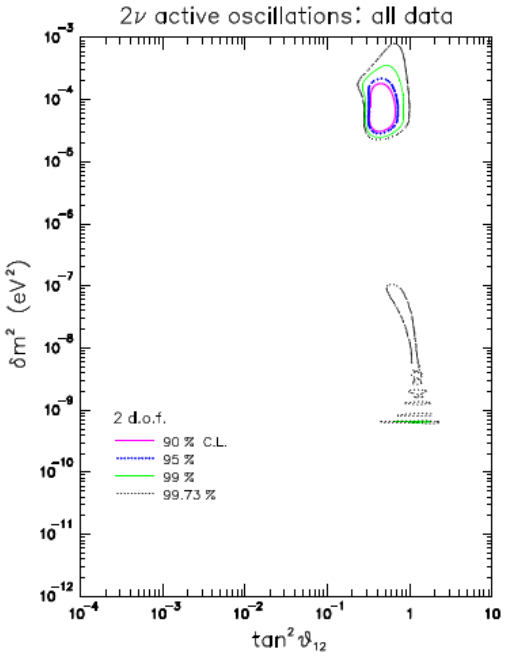

Figure 1.13: Confidence level contours in the (δm^2,$tan^2\theta_{12}$) parameter space [11]. The blob near the top right hand corner correspond to the LMA solution. Note that the SMA solution does not appear in this figure because of its low confidence level.

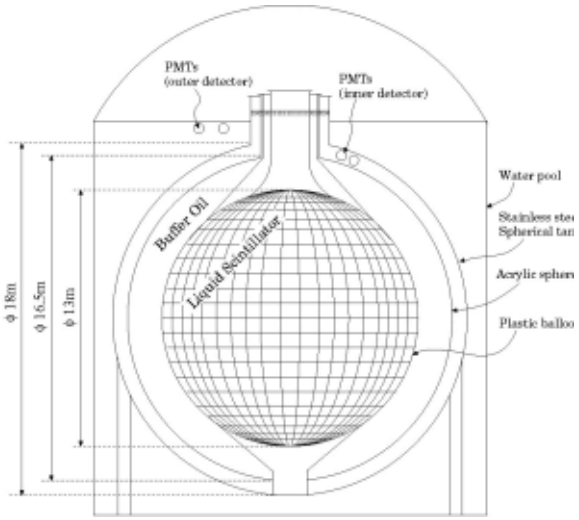

Figure 1.14: KamLAND detector [12].

beta decay process to detect antineutrinos and the delayed neutron was captured by hydrogen atom which gave out a 2.2 MeV gamma ray.

$$^1H + n \rightarrow {}^2D + \gamma(2.2MeV)$$

The energy in the gamma ray would be transferred to a charged particle, mainly to an electron through Compton scattering. The charged particles would produce scintillations in the liquid scintillator, which would be detected by the 1879 PMTs lined the inner part of the detector.

After accumulating 162 ton-yr worth of data, a significant deficit in the observed neutrino rate was found:

$$\frac{N_{obs}-N_{BG}}{N_{exp}} = 0.611 \pm 0.085(stat) \pm 0.041(syst)$$

This suggested that reactor neutrinos also undergo oscillation. On the other hand, the result of a two-flavor analysis strongly favors the LMA solution, rejecting the other three (Figure 1.15). KamLAND was also the first to observe spectral distortion in antineutrino energy [68]. With more data, in 2008, KamLAND produced an improved measurement of the solar mixing parameters (Figure 1.16).

1.2.6.2 Atmospheric Mixing Angle θ_{23} and Mass Splitting Δm^2_{23}

As described in the previous section, Super-K was the first experiment to provide convincing evidence for the oscillation of atmospheric neutrinos. However, θ_{23} and Δm^2_{23} were not very precisely measured

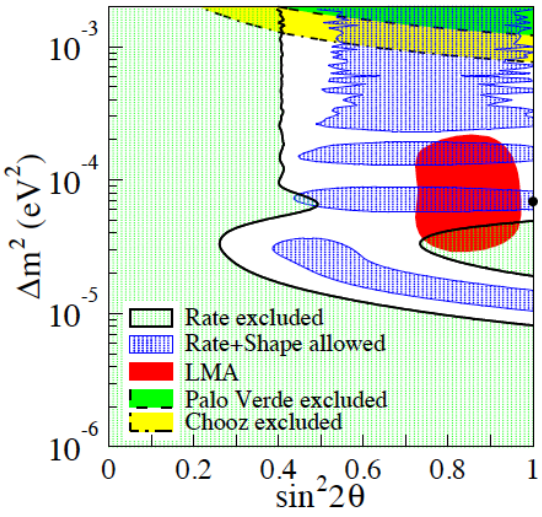

Figure 1.15: First result from KamLAND [13]

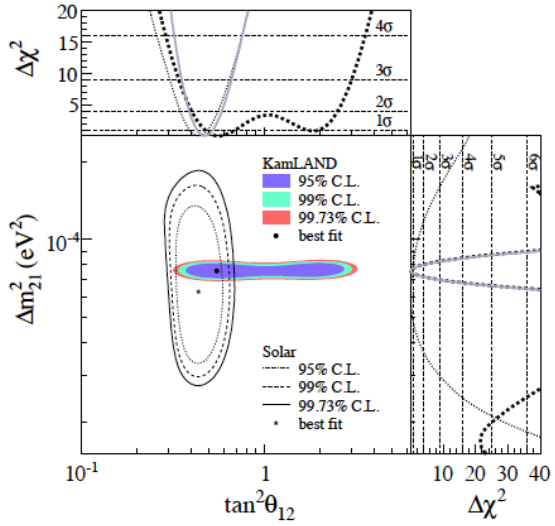

Figure 1.16: Latest result from KamLAND [14]

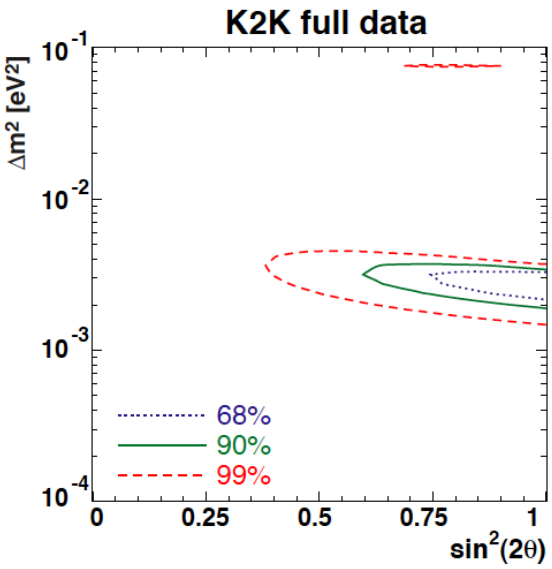

Figure 1.17: Result from K2K [15]

[8]. To increase statistics and to gain more control over neutrino source, in collaboration with the High Energy Accelerator Research Organization (Kou Enerugi Kasouki Kenkyuu Kikou, KEK), the KEK-to-Kamioka (K2K) experiment was established [15, 69, 70, 71, 72, 73]. K2K used the 12 GeV proton synchrotron at KEK to generate a ν_μ beam, which passes through a near detector at KEK. The beam would reach Super-K, located 250 km away, which served as the far detector. Disappearance of ν_μ was measured. With the analysis of 0.922×10^{20} protons-on-target (POT) worth of data, the value of θ_{23} was not tied down, but $sin^2 2\theta_{23}$ was expected to be close to 1, while $|\Delta m^2_{23}|$ was estimated to be between 1.9 and $3.5 \times 10^3 eV^2$ at the 90% CL.

Another accelerator-based experiment Main Injector Neutrino Oscillation Search (MINOS) also aimed at improving the measurements of θ_{23} and Δm^2_{23} [16, 74, 75]. The Neutrinos at the Main Injector (NuMI) ν_μ beam produced by 120 GeV protons from the Main Injector at Fermilab would first passes through the 0.98 kt near detector located 1 km away and would then reach the 5.4 kt far detector located 735 km away in the Soudan Iron Mine in Minnesota. Both the near and the far detector were tracking calorimeters, composed of alternating layers of steel and scintillator. Over six years of data taking, 7.25×10^{20} POT were collected. By looking for ν_μ disappearance, the experiment produced more precise estimate of Δm^2_{23} ($2.32^{+0.12}_{-0.08} \times 10^{-3} eV^2$) and a lower bound for

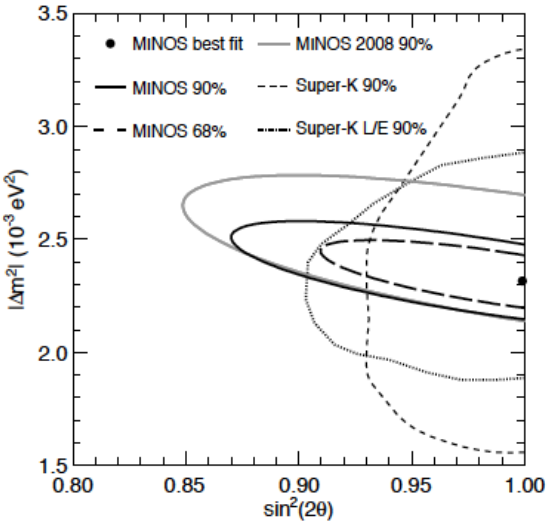

Figure 1.18: Result from MINOS [16]

$sin^2 2\theta_{23}$ ($sin^2 2\theta_{23} > 0.9$ at 90% C.L.). To date, these are the best measurements of these two oscillation parameters.

1.2.7 The Last Mixing Angle θ_{13}

Being the last unknown mixing angle, θ_{13} is, of course, important in its own right. In fact, having a precise measurement of θ_{13} would enable us to study the other parameters in the MNSP matrix, for example, the CP-violating phase δ_{CP}, which is essential to understanding CP-violation in lepton sector. The matter effect, which also depends on θ_{13}, is important for determining the mass hierarchy. From a broader perspective, this mass mixing model for neutrino oscillation would serve as useful inputs to the building of the next Standard Model of particle physics, and a precise measurement of θ_{13} would open the door to all these.

1.2.7.1 Tokai-to-Kamioka (T2K)

T2K [17], the successor to K2K, aims at measuring θ_{13} by looking for the appearance of ν_e in a ν_μ beam. Like K2K, T2K uses Super-K as the far detector which is 295 km away, but rather than KEK it uses the more powerful main synchrotron at J-PARC as the source of ν_μ. In 2011, with 1.43×10^{20} protons on target, T2K observed 6 ν_e candidates, in excess of the expected 1.5 ± 0.3

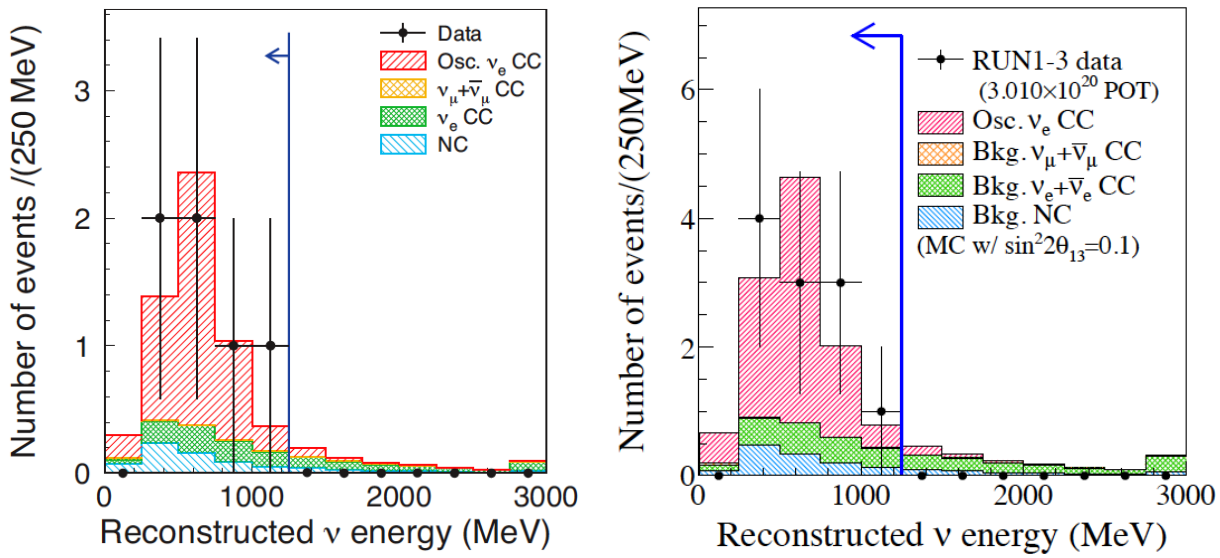

Figure 1.19: The left plot shows 6 ν_e events seen by T2K in 2011 [17], and the right plot is an update in 2013 with 11 events [18]. The blue arrow in both plots represents the selection criterion $E_\nu^{rec} < 1250$ MeV, which aimed to minimize the intrinsic ν_e background.

assuming no oscillation [17]. This translates into $0.03 < sin^2 2\theta_{13} < 0.28$ at 90% C.L. for normal hierarchy. A recent update [18] reported that a total of 11 events have been observed, yielding $sin^2 2\theta_{13} = 0.088^{+0.049}_{-0.039}$.

1.3 The Daya Bay Experiment

The Daya Bay Experiment aimed to improve the precision of the θ_{13} measurement using a relative flux measurement of reactor neutrinos. The following simplified example illustrates this strategy.

1.3.1 An Illustration: One-reactor Two-detector Case

It is instructive to consider the simplified situation where we only have one detector at a far site and one detector at a near site observing antineutrinos from one reactor core. In this situation, we have the following equation which describes how our measurements relates to $\sin^2 2\theta_{13}$, the quantity that we want to determine.

$$N_n = \frac{\Phi}{L_n^2} n_n \epsilon_n P_{sur}(E, L_n)$$
$$N_f = \frac{\Phi}{L_f^2} n_f \epsilon_f P_{sur}(E, L_f)$$

where

N_n/N_f is the number of detected antineutrinos by the near/far detector.

Φ is the total 4π antineutrino flux from the reactor core.

L_n/L_f is the distance between the reactor core and the near/far detector.

n_n/n_f is the number of target protons in the near/far detector.

ϵ_n/ϵ_f is the detection efficiency of the near/far detector.

$P_{sur}(E, L)$ is the survival probability of the antineutrino of energy E over a distance L.

From this equation, we can identify some sources of uncertainty. First, notice that $\sin^2 2\theta_{13}$ is buried inside the factor $P_{sur}(E, L)$. The first factor on the left hand side of the equation, $\frac{\Phi}{L_d^2}$ (where d = n or f), is related to reactor flux and reactor location while the factor $n_d\epsilon_d$ (where d = n or f) stems from detector properties. N_d (where d = n or f), on the right hand side, will be determined with the data. So, in addition to statististical uncertainty in N_d, uncertainty due to background subtraction would also contribute.

If we take the ratio of these two equations, we can obtain the following equation.

$$\frac{N_f}{N_n} = \left(\frac{n_f}{n_n}\right)\left(\frac{L_n}{L_f}\right)^2\left(\frac{\epsilon_f}{\epsilon_n}\right)\left[\frac{P_{sur}\left(E, L_f\right)}{P_{sur}\left(E, L_n\right)}\right]$$

Now the dependence on reactor flux has been completely eliminated, and those factors are replaced with their near/far ratios. That means instead of the absolute uncertainty in those factors, our concern now should be the uncertainty in their ratios, or the relative uncertainty.

1.3.2 Other Contemporary θ_{13} Experiments

There are two other reactor-based experiments that are similar to Daya Bay: Double CHOOZ and RENO. Both of them employ strategies similar to Daya Bay's for measuring θ_{13}. They will be briefly discussed in the next chapter.

Chapter 2

The Experiment

The Daya Bay reactor neutrino experiment aims to determine $\sin^2 2\theta_{13}$ with a sensitivity of 0.01 at the 90% confidence level by comparing relative neutrino rates and spectra at various baselines.

2.1 Sites

The Daya Bay Nuclear Power Complex is located at Daya Bay, about 50 km northeast of Hong Kong and about 40 km east of Shenzhen. It consists of 6 reactor cores, located at 3 power plants as shown in Figure 2.1: Daya Bay Nuclear Power Plant, Ling Ao I Nuclear Power Plant and Ling Ao II Nuclear Power Plant; each having 2 cores. Each core produces a thermal power of about 2.9 GW, emitting roughly 6×10^{20} $\bar{\nu_e}$ per second. This is a good source of reactor neutrinos that the Experiment can make use of. On the other hand, the hilly terrain in the region provides adequate overburden for shielding against cosmogenics. This makes Daya Bay an attractive location for establishing a reactor neutrino experiment.

To maximize the disappearance effect in the antineutrino flux, the locations for the two near sites and the far site had to be carefully chosen. As seen in Figure 2.2, the probability of disappearance due to θ_{13} attains a maximum at about 2 km, which indicates that this is a good location to establish the far site. When combined with a measurement of the antineutrino flux in close proximity to the reactors (near site), the uncertainty in reactor antineutrino flux can be greatly reduced, enabling a precise measurement of $\sin^2 2\theta_{13}$.

Optimizing the site locations requires balancing different factors, for example, reactor neutrino

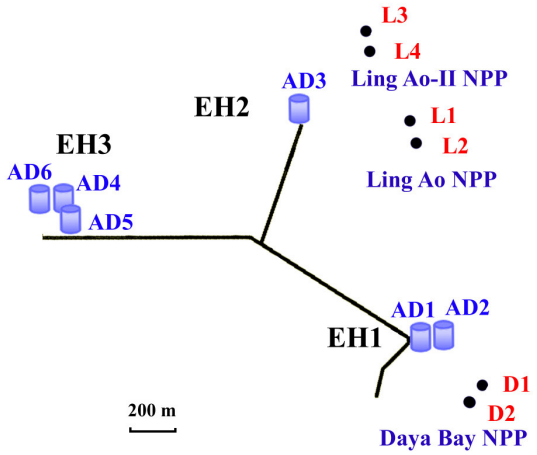

Figure 2.1: Site map showing the Daya Bay Reactor Cores, Ling Ao Reactor Cores and the antineutrino detectors.

	Daya Bay Near (EH1)	Ling Ao Near (EH2)	Far (EH3)
Overburden [m.w.e.]	250	265	860
Muon rate [Hz]	1.27	0.95	0.056
Mean muon energy [GeV]	57	58	137
Distance from D1/D2 [m]	364	1348	1912
Distance from L1/L2 [m]	857	480	1540
Distance from L3/L4 [m]	1307	528	1548

Table 2.1: Site information including baselines and overburdens.

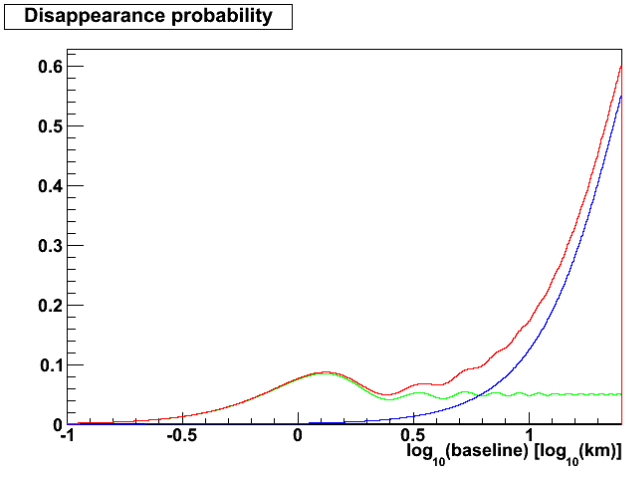

Figure 2.2: Antineutrino disappearance probability as a function of distance from reactor core. The blue and the green lines show respectively the contribution from θ_{12} and θ_{13} while the red line shows the sum of the two.

flux, amount of overburden, systematics and other uncertainties. For the near sites, apart from placing them as close to the reactors as possible while having good overburden, each of them should also be situated such that it is equidistant from the cores it monitors, so that the uncorrelated part of the reactor-related uncertainties could be minimized. While for the far site, it is best to locate it at the distance of about 2 km from all cores where the disappearance attains a maximum. However, at such a location, the overburden is only 200 m. To gain more overburden, the far site was, instead, positioned about 500 m east of that equidistant point. The site locations were optimized by using a global χ^2 analysis. Their amounts of overburden are shown in Table 2.1.

2.2 Reactor

The Daya Bay and Ling Ao reactor cores are used as sources of antineutrinos. These reactor cores generate heat and hence electricity mainly from the fission of ^{235}U, ^{238}U, ^{239}Pu and ^{241}Pu, and the fission fragments of these isotopes can often beta-decay producing antineutrinos:

$$\text{“n”} \rightarrow \text{p} + \text{e}^- + \bar{\nu_e}$$

where “n” indicates a bound neutron. The emitted antineutrinos would then propagate away from the core, a tiny fraction of which would be detected by our detectors.

2.3 Detector

Eight movable, modular, functionally identical antineutrino detectors (ADs) are constructed for observing the antineutrinos. The ADs detect antineutrinos via inverse beta decay (IBD). When traversing matter, an antineutrino can, with a very small cross-section (Figure 2.3), weakly-interact with a proton, giving a positron and a neutron.

$$\bar{\nu_e} + \text{p} \rightarrow \text{e}^+ + \text{n}$$

The AD designed to capture both the positron and the neutron from inverse beta decay. The target volume in the AD composes of a LAB-based liquid scintillator loaded with 0.1% Gd (GdLS).

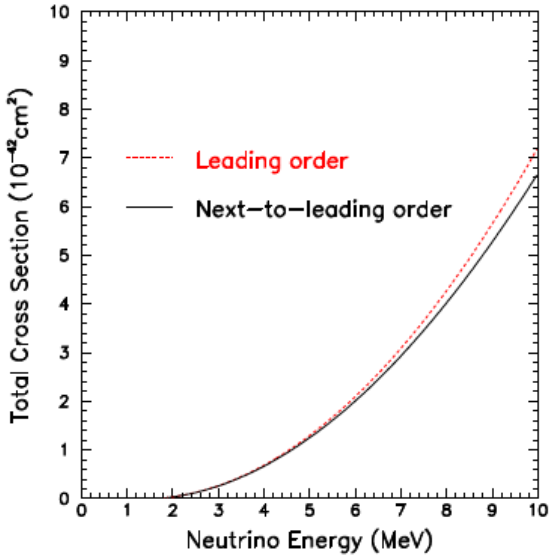

Figure 2.3: Inverse beta decay cross-section as a function of antineutrino energy. [19]

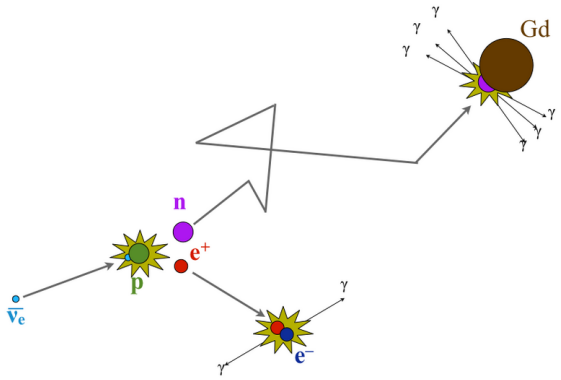

Figure 2.4: Diagram illustrating the inverse beta decay (IBD).

When an IBD occurs in GdLS, the positron would promptly annihilate with an electron, giving out some 511 keV annihilation photons (prompt signal). Some of the neutrons would eventually be captured by Gd nuclei, giving out characteristic capture gammas with a total energy of about 8 MeV (delayed signal). With the designed Gd concentration the two signals would occur about 30 μs apart.

$$\text{Prompt signal: } e^+ + e^- \rightarrow \gamma + \gamma$$

$$\text{Delayed signal: } n + {}^{n}\text{Gd} \rightarrow {}^{n+1}\text{Gd}^* \rightarrow {}^{n+1}\text{Gd} + \Sigma\gamma$$

Both the prompt and the delayed signal would produce scintillations and are viewed by photomultiplier tubes (PMTs) lined along the inner wall of the AD. There would be two phases of operation: Phase 1 would be a partial configuration with 6 ADs, and Phase 2 would be the full configuration with all 8 ADs. In the first phase, 2 ADs are placed at the Daya Bay Near Site, 1 at the Ling Ao Near Site and 3 at the Far Site (2-1-3 arrangement). In the second phase, one more will be placed at the Ling Ao Near Site and another at the Far Site (2-2-4 arrangement).

2.4 Background

Given the timing structure of the IBD signal (prompt + delayed), backgrounds can be categorized into two types: correlated and uncorrelated. Correlated background refers to backgrounds, originating from a single source, which can mimic the IBD timing structure, while uncorrelated (or accidental) backgrounds refer to those originating from different sources, which can only mimic the timing structure accidentally.

There are four major sources of correlated backgrounds in the current experiment: ^{9}Li/^{8}He, fast neutrons, ^{241}Am-^{13}C and natural radioactivity.

^{9}Li/^{8}He, which are produced by cosmogenic muons, have significant branching fraction for beta-neutron decay. The emitted beta can mimic a prompt signal, while the neutron produces a delayed signal.

Fast neutrons are also produced by cosmogenic muons through spallation in matter. One scenario of correlated background is when the neutron produced in the surrounding rock diffuses into the detector, and generates a proton recoil signal in the detector which, mimics the prompt signal. Then the neutron is later captured on a Gd nucleus, which produces a delayed signal.

^{241}Am-^{13}C (or simply AmC) is a neutron source intended to be used for detector calibration. Neutrons from the AmC can inelastically scatter in the stainless steel vessel, which contains the detector, and are eventually captured by some nuclei in the the stainless steel, giving out energetic gamma rays. This could mimic the prompt-delayed timing signature if both gamma rays enter the AD.

Natural radioactive isotopes outside the detector can normally only contribute to accidental background through gamma emissions. However, if the there are radioactive contaminants present in the detector, alpha emitters in the decay chains can cause (α,n) reaction, e.g. ^{13}C(α,n)^{16}O. In addition to the neutron, the resulting isotope can sometimes emit a gamma almost immediately ($< 1ns$) after neutron emission. This additional gamma can mimic a prompt signal, while the neutron produces a delayed signal.

Accidental background is produced by single hits (or simply singles) of the detector. An accidental coincidence is formed when a pair of singles happen to survive all selection cuts and is (mis-)categorized as an IBD candidate. Due to its stochastic nature, accidental background can be precisely estimated with measured singles rate and is then statistically subtracted.

2.5 Uncertainties

There are two types of uncertainties: statistical and systematic. Due to the proximity to the reactor cores, we anticipate copious amount of antineutrinos. This allows us to collect high statistics, hence, limiting the effect of statistical uncertainty. In the long run, however, systematic uncertainties dominate.

The experiment is designed to make relative flux and spectral measurements among detectors at various sites. Hence we are more concerned with relative systematic uncertainies among detectors. In other words, systematic uncertainties that are correlated among detectors are more "benign" because they tend to "cancel" each other out in the case of a relative measurement.

Systematic uncertainties can be further classified according to their source. Below is a brief description of these categories of systematic uncertainties.

2.5.1 Reactor-related Uncertainty

The placement of the experimental halls, by design, should have largely cancelled the correlated uncertainty in antineutrino flux from reactor cores, though some residual uncorrelated uncertainty remains. For example, fluctuations in power, fission fractions, and the amount of spent fuel nearby

could be uncorrelated among reactor cores. The accuracy in locating the reactor cores relative to the detector also contributes albeit small. The uncorrelated uncertainty in the reactor flux is estimated to be 0.8%. The residual uncertainty in $\sin^2 2\theta_{13}$ is about 0.05 of this value. (See Chapter 3)

2.5.2 Detector-related Uncertainty

The ADs are designed to be functionally identical, which means that the properties of the detector, mechanical, chemical or optical, should be "as identical as possible". As discussed above, relative difference in the number of target protons and the detection efficiency is the main source of uncertainty. The detector-related uncertainty is estimated to be 0.2%. (See Chapter 4 and Chapter 8)

2.5.3 Background-related Uncertainty

As mentioned in Section 2.4, there are several major sources of background. Accidental background ranges from about 3 per day per AD in the far site and about 10/7 per day per AD in the Daya Bay/Ling Ao near sites. The uncertainties are very small due to the relatively high singles rates. The rates of the correlated backgrounds are low, often in the order of 1 per day which is about 0.1%/1% of the expected IBD rate at a near/far detector. Due to the complex production mechanism of some backgrounds, it is sometimes not easy to determine the systematic uncertainty of their rates. (See Chapter 9 for details)

2.6 Other Contemporary θ_{13} Experiments

2.6.1 Double CHOOZ

In fact, CHOOZ, the predecessor of Double CHOOZ [76], was among the earliest to produce an upper limit for $sin^2 2\theta_{13}$ by comparing the observed $\bar{\nu}_e$ flux with expected $\bar{\nu}_e$ flux from the reactor core. ($sin^2 2\theta_{13} < 0.17$ for large Δm^2_{23})

In addition to the original CHOOZ detector, a near detector was planned to be constructed 280 m

from the reactor cores. Double CHOOZ would look for $\bar{\nu}_e$ disappearance by comparing $\bar{\nu}_e$ fluxes the near detector and the far detector. But before the completion of the near detector, a measurement of $sin^2 2\theta_{13}$ was made, using only the data from its far detector. In this far-only phase, the sensitivity was limited by the uncertainty in the average IBD cross-section $\langle\sigma_f\rangle$ which is defined as the sum of the average IBD cross-section of all fission isotopes $\langle\sigma_f\rangle_k$ weighted by the respective fission fractions α_k; and the average IBD cross-section of each fission isotopes is defined as the convolution of its $\bar{\nu}_e$ spectrum $S_k(E)$ and the IBD cross-section $\sigma_{IBD}(E)$. This can be written as,

$$\langle\sigma_f\rangle = \sum_k \alpha_k \langle\sigma_f\rangle_k = \sum_k \alpha_k \int_0^\infty dE S_k(E)\sigma_{\mathrm{IBD}}(E)$$

The main source of uncertainty, which is about 3%, comes from $S_k(E)$. The effect of this uncertainty was reduced by a technique referred to as "anchoring". The rate measurement of Bugey4 [77] is used as an anchor for calculating the average IBD cross-section for reactor R in the following way:

$$\langle\sigma_f\rangle^R = \langle\sigma_f\rangle^{\mathrm{Bugey}} + \sum_k (\alpha_k^R - \alpha_k^{\mathrm{Bugey}})\langle\sigma_f\rangle_k$$

The Bugey4 anchor point has a relatively small uncertainty of 1.4%. Together with the smallness of the difference in fission fractions $(\alpha_k^R - \alpha_k^{\mathrm{Bugey}})$, the uncertainty in $\langle\sigma_f\rangle^R$ can be reduced. In July 2012, Double CHOOZ published a measurement of $sin^2 2\theta_{13}$, using the anchoring technique:

$$sin^2 2\theta_{13} = 0.109 \pm 0.030 \text{ (stat)} \pm 0.025 \text{ (syst)}$$

2.6.2 RENO

RENO is reactor based experiment located near the Yonggwang Nuclear Power Plant in Korea [20, 78]. Compared with Double Chooz, RENO's design more closely resembles Daya Bay's. It has two identical detectors, one located at 294 m from the reactor cores and the other 1383 m. Each detector contains 16 t of Gd-loaded liquid scintillator as the target. The detectors also have a similar three-zone design, but instead of reflective panels on the top and bottom of the detector, additional PMTs are installed there. There are a total of 354 10"-PMTs per detector giving a 14% photocoverage. Taking everything together, RENO would have a similar $\bar{\nu}_e$ detection rate per

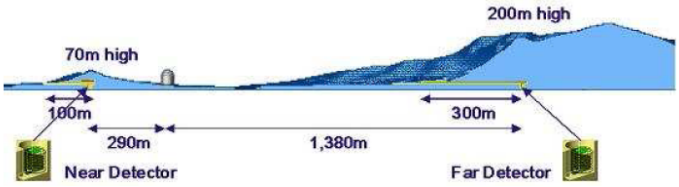

Figure 2.5: Layout of the RENO experiment. [20]

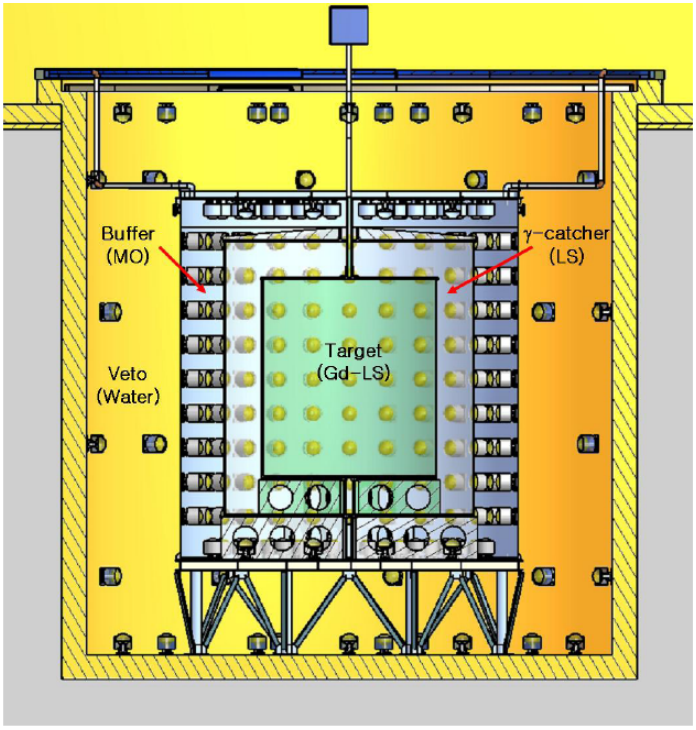

Figure 2.6: RENO detector. [20]

detector as Daya Bay. In April 2012, using 229 days worth of data, RENO published a measurement of $sin^2 2\theta_{13}$:

$$sin^2 2\theta_{13} = 0.113 \pm 0.013 \text{ (stat)} \pm 0.019 \text{ (syst)}$$

2.6.3 Summary

The following table shows the comparison among Daya Bay, Double CHOOZ and RENO.

Experiment	Total Reactor Thermal Output (GW_{th})	Detector Distance Near/Far (m)	Overburden Near/Far (m.w.e.)	Target Mass (Near/Far) (t)
Daya Bay	17.4	364(480)/1912(1540)	250/860	20×2/80
Double CHOOZ	8.7	260/1050	115/300	10/10
RENO	16.4	292/1380	110/450	16/16

Chapter 3

The Reactor Cores

Although the experiment is set up so that the reactor-related uncertainties that are correlated can be neglected, there are still some residual uncorrelated uncertainties originating from reactors that cannot be neglected. This prompted us to better understand how neutrinos are produced in the reactors and how this would affect the accuracy in estimating the expected flux and energy spectrum of the anti-neutrinos passing through our detectors.

3.1 Antineutrino Production at the Reactor Cores

The Daya Bay reactors cores are Pressurized Water Reactors (PWR) (Figure 3.1), which generally produce electricity using nuclear fissions of heavy isotopes, e.g. ^{235}U, ^{238}U, ^{239}Pu and ^{241}Pu. Heat is first generated from fission products, mainly through neutrons. The pressurized water in which the fuel rod are immersed, are passed to the steam generator, which in turn produces steam (the primary loop). The steam then drives a turbine which is connected to a generator that eventually produces electricity (the secondary loop).

Typically for a fresh fuel rod, 69% of the fissions come from ^{235}U, 7% from ^{238}U, 21% from ^{239}Pu and 3% from ^{241}Pu [34]. As the reactor runs, fuel composition would change and the fission fragment would gradually build up. The fission fragments can often beta-decay: $n \rightarrow p + e^- + \bar{\nu_e}$. These fission fragments beta-decay at various energies and half-lives, and hence the antineutrino spectra differ. Therefore, we expect that the overall energy spectrum of antineutrinos produced would evolve over time. Mathematically [79],

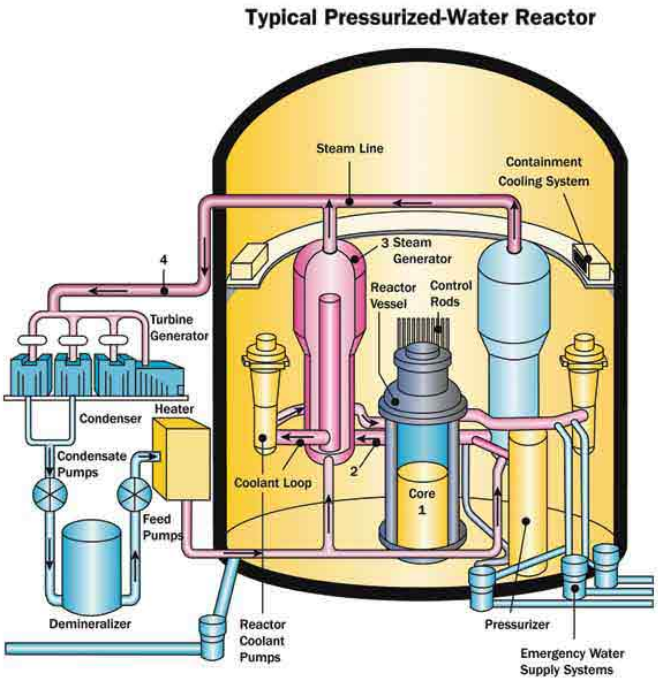

Figure 3.1: An illustration of a Pressurized Water Reactor (PWR). [21]

$$S(E_\nu, t) = \frac{W_{th}}{\Sigma_i f_i(t) e_i} \sum_i f_i(t) S_i(E_\nu)$$

where

e_i: Energy produced by one fission of isotope i

W_{th}: Total heat generated by the reactor core

$f_i(t)$: Fractional contribution of isotope i to the total number of fissions

$S_i(E_\nu)$: Antineutrino energy spectrum of isotope i

3.2 Estimating the Expected Antineutrino Spectrum

In order to estimate the antineutrino spectrum, there are several parameters that we need to determine: Energy produced by one fission of isotope i, e_i; the total thermal power generated by the reactor core, W_{th}; the fractional contribution of isotope i to the total number of fissions, $f_i(t)$; the antineutrino energy spectrum of isotope i, $S_i(E_\nu)$.

Isotope	Energy per Fission [MeV]
^{235}U	201.92 ± 0.46
^{238}U	205.52 ± 0.96
^{239}Pu	209.99 ± 0.60
^{241}Pu	213.60 ± 0.65

Table 3.1: Energy produced by one fission of isotope each isotope (e_i). [34]

3.2.1 Energy Produced by One Fission of Isotope i (e_i)

The energy produced in the fission of these isotopes has been calculated in [34] and is tabulated in Table 3.1. This is expected to contribute a 0.2% correlated uncertainty.

3.2.2 Total Thermal Power Generated (W_{th})

The daily thermal power measurement is provided by the nuclear power plant. There are two systems that measures the heat balances in the core, namely, the KIT/KDO system and the KME system. The thermal power data that the power plant provides comes from the KIT/KDO system, which based on the measurement of the temperature, pressure, and the input water flow rate in the primary loop. The KME system, which measures similar quantities in the secondary loop and has a higher accuracy than the KIT/KDO system, serves as a monthly calibration benchmark for the KIT/KDO system. The uncorrelated uncertainty of such measurements are estimated to be 0.5% [80].

3.2.3 Fractional Contribution of Isotopes ($f_i(t)$)

The evolution of isotopic composition in a fuel rod is related to how reactors operate. Generally, the ^{235}U and the ^{238}U content would decrease over time, while the ^{239}Pu and the ^{241}Pu content would increase. However, to accurately estimate the fuel composition, simulations of the reactor cores are typically performed by the power plant company. For Daya Bay, reactor core simulations were performed by the power plant company using SCIENCE [81], a simulation package developed by CEA France with APOLLO2 as its core component. The isotopic compositions from the simuation are also provided by the nuclear power plant. The fission fractions are assumed to be proportional to the isotopic compositions. The uncertainty in isotopic composition, and hence the fission fractions, is estimated to be 5% [82]. To understand the uncorrelated uncertainties between the fission fractions,

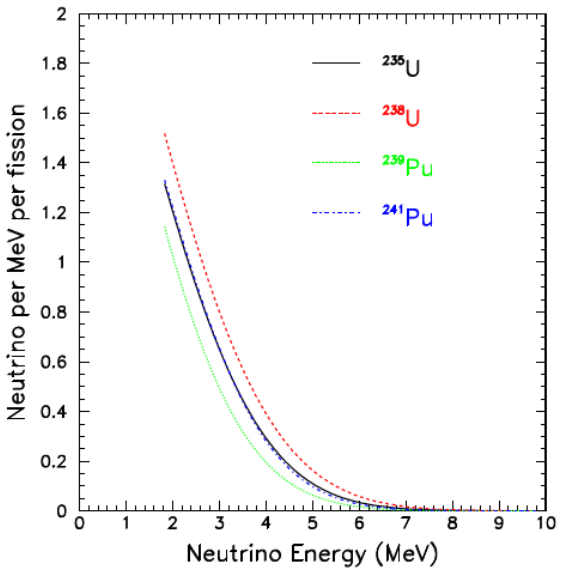

Figure 3.2: Energy spectrum of antineutrinos from fission.

a DRAGON [83] model was constructed. By varying the input fission fractions to the model, the correlation between fission fractions can be studied. The uncorrelated uncertainty in antineutrino flux between reactor cores can be calculated to be 0.6% [80]. The spatial distribution of the isotopes in the core was found to have negligible effect.

3.2.4 Antineutrino Energy Spectrum of Isotopes ($S_i(E_\nu)$)

The antineutrino energy spectrum for the isotopes ^{235}U, ^{239}Pu and ^{241}Pu were measured at ILL [84, 85, 86]. They were shown to agree with the Bugey 3 measurement [87]. Huber [88] improved the ILL-measured spectra. A theoretical calculation for ^{238}U was done by Vogel [89] and was improved by Mueller et al. with an *ab initio* calculation [90]. The reactor flux models are expected to have a correlated uncertainty of about 3%.

3.2.5 Non-equilibrium and Spent Nuclear Fuel

The duration of the ILL measurements were around 1 to 2 days. With this short duration, short-lived isotopes, which could beta-decay, would have a stronger contribution to the antineutrino spectrum than in an actual reactor. Meanwhile, the relatively long-lived isotopes would not have sufficient

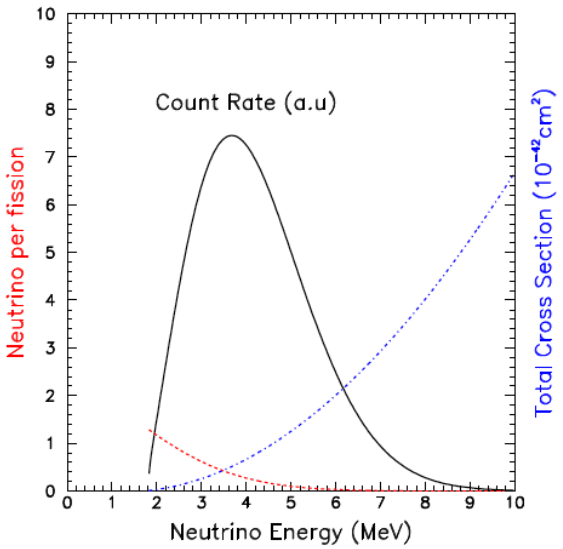

Figure 3.3: Expected antineutrino energy spectrum.

time to equilibrate. On the other hand, in the actual reactor, spent nuclear fuel, which still continues to beta decay, is stored near the reactor core. These modify the antineutrino spectrum as follows:

$$S_i(E_\nu) = S_{\text{ILL}}(E_\nu) + S_{\text{long-lived}}(E_\nu) - S_{\text{non-eq}}(E_\nu)$$

Due to the lack of information, the effect due to spent nuclear fuel cannot be easily corrected and is therefore treated as an uncertainty [91, 92]. The effect due to non-equilibrium is corrected according to [90]. The contribution by spent fuel to the antineutrino flux of each reactor core is about 0.3% and this is taken as an uncorrelated uncertainty.

3.2.6 Expected Antineutrino Spectrum

Combining the quantities obtained above, we can construct the energy spectrum of antineutrinos expected to be detected by convolving the IBD cross-section with the expected antineutrino energy spectrum (Figure 3.3).

3.3 Baselines

The coordintes of the reactor cores relative to the detectors are determined with a system of GPS and total stations to a precision of 18 mm [93]. Table 3.2 shows all the baselines between each

	D1	D2	L1	L2	L3	L4
AD1	362.377	371.759	903.470	817.162	1353.622	1265.319
AD2	357.937	368.411	903.351	816.900	1354.233	1265.890
AD3	1332.475	1358.144	467.571	489.574	557.580	499.207
AD4	1919.630	1894.335	1533.177	1533.625	1551.381	1524.937
AD5	1917.516	1891.974	1534.916	1535.029	1554.764	1528.043
AD6	1925.253	1899.859	1538.927	1539.465	1556.341	1530.076

Table 3.2: Baselines between each detector and each reactor core in meters. [35]

detector and each reactor core. Uncertainties in baselines are clearly negligible. The baselines were initally blinded before the analysis method was finalized.

3.4 Summary of Uncertainty

The reactor-related uncertainties are summarized below.

Correlated Uncertainty	[%]	Uncorrelated Uncertainty	[%]
Energy per fission	0.2	Power	0.5
$\bar{\nu_e}$ per fission	3	Fission fraction	0.6
		Spent fuel	0.3
Combined	3	Combined	0.8

The residual uncertainty in the final measurement of $sin^2 2\theta_{13}$ can be further reduced if we consider the following combination of ratios of event rates:

$$\rho = \frac{\alpha \sum_r \frac{\phi_r}{(L_r^{DYB})^2} + \sum_r \frac{\phi_r}{(L_r^{LA})^2}}{\sum_r \frac{\phi_r}{(L_r^{Far})^2}}$$

where ϕ_r is the total antineutrino flux from core r, L_r^X (X=DYB, LA, Far) are the baselines and α is a constant that can be tuned so that ρ has minimal sensitivity to antineutrino flux fluctuations. Notice that without oscillations, ρ is determined completely by geometry once α is given. For the Daya Bay configuration, α can be determined to be about 0.4. With this α, the uncertainty in ρ is about 0.05 of the original uncorrelated uncertainty in antineutrino flux. This procedure was not explicitly performed in the final analysis as the fluxes were allowed to vary in the χ^2 minimization

to achieve optimal weighting.

Chapter 4

The Antineutrino Detectors

The AD consists of three nested concentric cylindrical containers. The innermost one, known as Inner Acrylic Vessel (IAV), contains 0.1% Gd-loaded liquid scintillator (GdLS). The IAV is made of acrylic and has a diameter and a height of about 3.1 m. This region serves as the target volume, where IBD events would be detected. The Outer Acrylic Vessel (OAV), having a diameter and a height of about 4 m, contains unloaded liquid scintillator (LS) in addition to the IAV which serves as a gamma catcher. The outermost one is the Stainless Steel Vessel (SSV) which contains mineral oil (MO), used as a buffer for shielding the LS from external radiation. A total of 192 Hamamatsu 8" PMTs are mounted on removable ladders that are secured on the inner wall of the SSV with rails. A radial light shield, made of black tyvek, was installed on the PMT ladders, to simplify the light propagation in the AD, and hence, reconstruction algorithms. Inside the SSV, two reflective panels were mounted at the top and at the bottom of the MO buffer region, to enhance photo-coverage and uniformity of the detector. Three Automated Calibration Units (ACU) sit on top of each AD: one at the center of the AD, one at the edge of the target volume, and one at the gamma catcher region. Each ACU houses some radioactive sources and an LED, for periodic calibrations of the AD. The AD is also equipped with various sensors for monitoring temperature and liquid levels, etc. At each site, the ADs are submerged in an octagonal water pool (or water shield) for shielding against ambient background. The water shield is lined with some 8" PMTs (288 at each of the near sites, 368 at the far site) and is partitioned into two optically separate parts, the Inner Water Shield (IWS) and Outer Water Shield (OWS). Both the IWS and the OWS act as Cherenkov detectors for

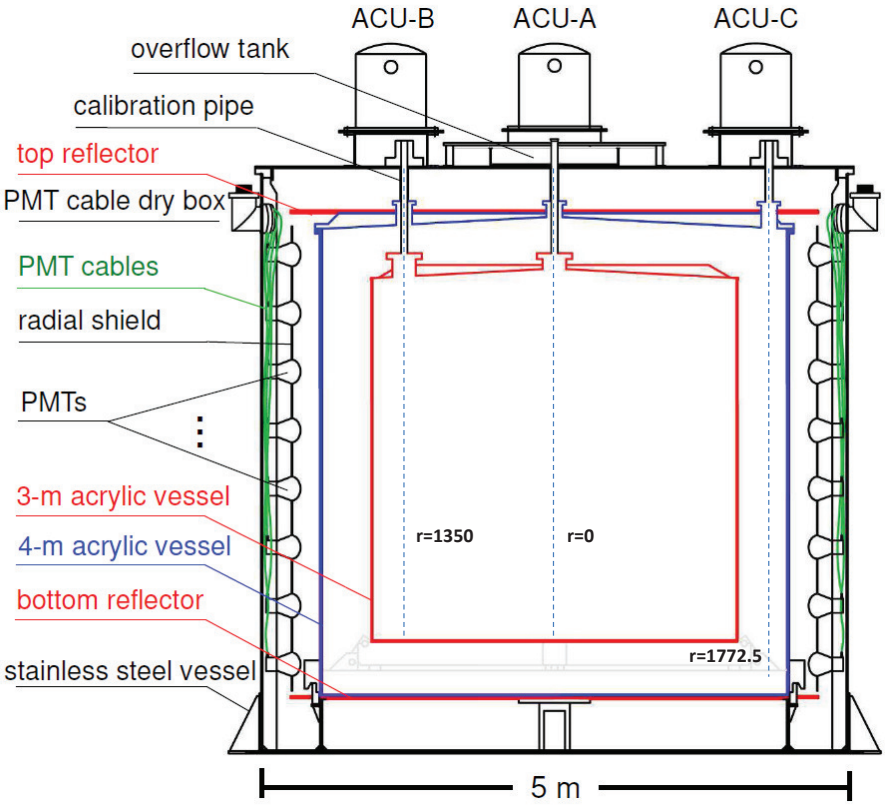

Figure 4.1: Internal structure of the Daya Bay antineutrino detector. The inner acrylic vessel (IAV) holds the Gd-loaded liquid scintillator which serves as the target. The outer acrylic vessel (OAV) holds regular liquid scintillator which serves as the gamma catcher. The outermost zone inside the stainless steel tank where PMTs are located is filled with mineral oil. The target zone is monitored by two ACUs, A (r=0 cm) and B (r=135.0 cm). ACU C (r=177.25 cm) monitors the gamma catcher zone. Three vertical source deployment axes are indicated by the dashed lines.

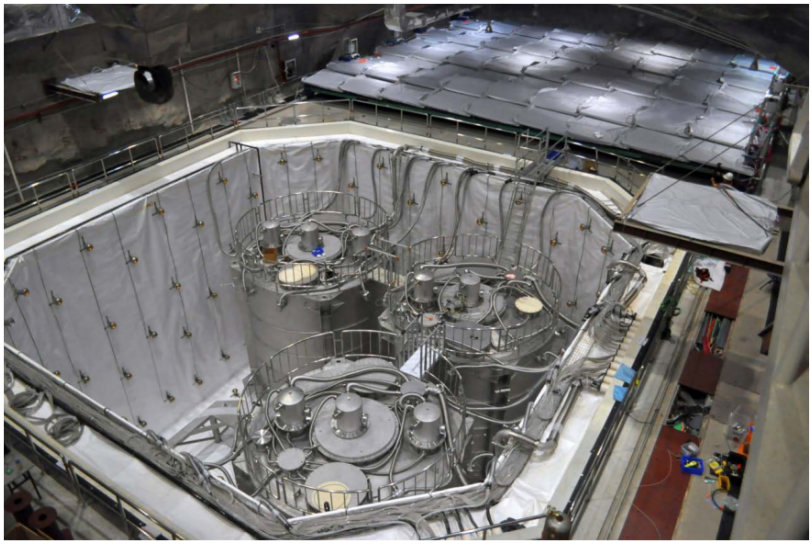

Figure 4.2: A photo showing the antineutrino detectors inside the water pool at the far site.

tagging muons. An array of RPCs are placed over the water pool as an additional muon detection system. Having multiple muon detectors can not only increase muon veto efficiency, but can also allow for a more accurate determination of this efficiency.

4.1 Target Volume and the Gamma Catcher

The target volume, is about 20 tons of GdLS, consists primarily of linear alkylbenzene (LAB), which is used as the scintillator base. 3 g/L of 2,5-diphenyloxazole (PPO) and 15 mg/L of 1,4-bis[2-methylstyryl]benzene (bis-MSB) are added as wavelength shifters (from UV to 430 nm blue light) and 0.1% Gd (as a compound with 3,5,5-trimethylhexanoic acid (TMHA) in the form of $Gd(TMHA)_3$ complex) for capturing neutrons. Except for the absence of Gd, the 20 tons of LS used in the gamma catcher is, otherwise, identical to GdLS. When a charged particle or a high energy photon deposits energy in the GdLS or LS, the scintillator becomes excited, giving out UV light as it de-excites. The UV photons are then shifted to visible light at a wavelength of about 430 nm by the fluors PPO and bis-MSB (Figure 4.3). The light would then be detected by the PMTs. The density of GdLS and LS are about 0.86 g cm^{-3}. The attenuation length of GdLS at 430 nm is measured to be >20 m.

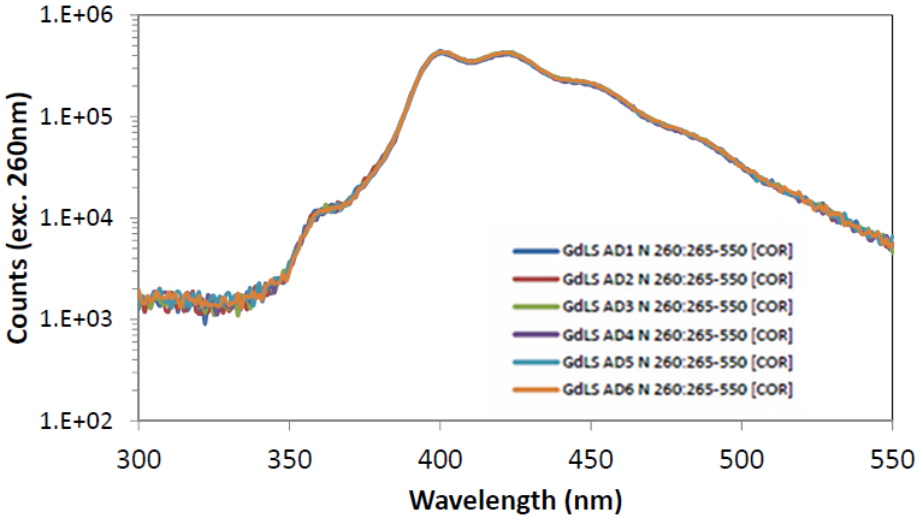

Figure 4.3: Emission spectrum of GdLS for different ADs (in different colors).

4.2 Oil Buffer Region (MO)

The oil buffer region consists of 40 tons of mineral oil. The purpose of having this layer is to shield natural gamma radiation from the PMTs and the surroundings from reaching the scintillating regions. It also helps shield the detector from neutrons generated outside the detector. The density of the mineral oil is about 0.85 g cm^{-3}, which closely matches with that of GdLS and LS to reduce the effect of buoyancy and the stress on the acrylic vessels. The attenuation length is >20 m.

4.3 Photomultiplier Tubes (PMTs)

A total of 192 Hamamatsu R5912 8" low-radioactivity PMTs were installed in each detector in 8 rows (or rings) and 24 columns, each separated by 0.5 m vertically and 15 degrees in azimuth, providing an effective photocoverage of 12%. Structurally, the PMTs were mounted on 8 ladders, each with 3 columns of PMTs. The ladder was covered with black Tyvek panels of low reflectivity mainly to simplify vertex reconstruction due to reflections. Each PMT was wrapped in a 16 μm thick FINEMET® foil to reduce the impact of terrestrial magnetic field on the PMTs.

4.4 Reflective Panels

Two specular reflectors were installed at the top and the bottom of the AD to enhance uniformity and photocoverage. The reflectors are made of a reflective film (Vikuiti® Enhanced Specular Reflector, or ESR), developed by 3M, sandwiched between two acrylic panels. They have reflectivity above 98% across most of the relevant spectrum.

4.5 Calibration System

To better understand the energy response of the detector and to monitor its time variation, two calibration systems were developed. The automated calibration system can deploy radioactive or light sources along 3 axes: the central axis (A), the off-center axis (B) and the gamma catcher region (C). The ACU, which is installed on each axis, contains three deployment capsules: LED, ^{241}Am-^{13}C with ^{60}Co, and ^{68}Ge. The sources in the ACU were deployed weekly. Three LEDs were mounted on the PMT ladders (MOLEDs) and six Hamamatsu R7724 2" PMTs were installed at the top and the bottom of the AD (2" PMTs). These help monitor the clarity of all liquids. To supplement the automated system, the manual calibration system had also been constructed. It consists of a robotic arm with a ^{239}Pu-^{13}C and ^{60}Co attached at the tip. The robotic arm could reach into the AD through the ACU A penetration and would be able to locate the sources essentially anywhere inside the target volume.

Source	Type	Energy	Half-life	Rate [Hz]	Auto/Manual System
LED	visible γ	430 nm	-	500 (adjustable)	Auto
^{68}Ge	e^+	1.022 MeV	270.95 d	10	Auto
^{60}Co	γ	2.5 MeV	1925.28 d	100	Auto and Manual
^{241}Am-^{13}C	n	$\sim$8 MeV*	432.6 y	$\sim$0.5	Auto
^{239}Pu-^{13}C	n	$\sim$8 MeV*	24110 y	$\sim$1000	Manual

Table 4.1: List of calibration sources. (* Energy of the capture gammas.)

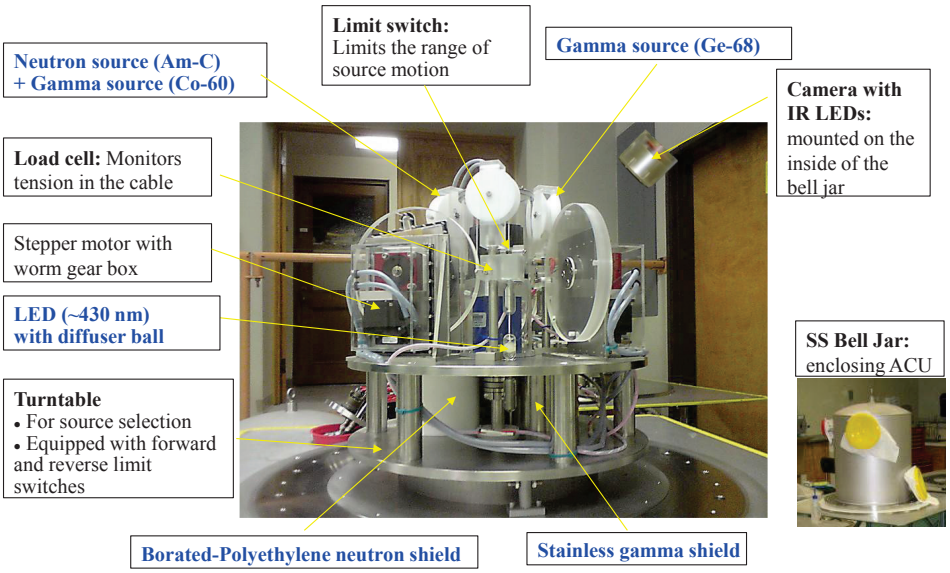

Figure 4.4: An overview picture of an ACU.

4.6 Muon Veto

Some of the major backgrounds are caused by cosmogenic muons. Although the detectors are located under a mountain, energetic muons can still penetrate, triggering the detectors. Two independent muon detectors, a water Cherenkov detector (which is further partitioned into two detectors) and a Resistive Plate Chamber (RPC) detector, are set up to tag muons with an efficiency $> 99.5\%$ and uncertainty $< 0.25\%$.

4.6.1 Water Cherenkov Detectors

Surrounding the ADs is a pool of deionized water. It provides an at least 2.5 m of passive shielding, in addition to serving as a Cherenkov detector. The water pool is partitioned into two regions, the inner water shield (IWS) and the outer water shield (OWS), by a layer of opaque tyvek. A total of 288 8" PMTs were installed in each near sites, and 384 in the far site. Some of these PMTs are recycled from the MACRO experiment [94].

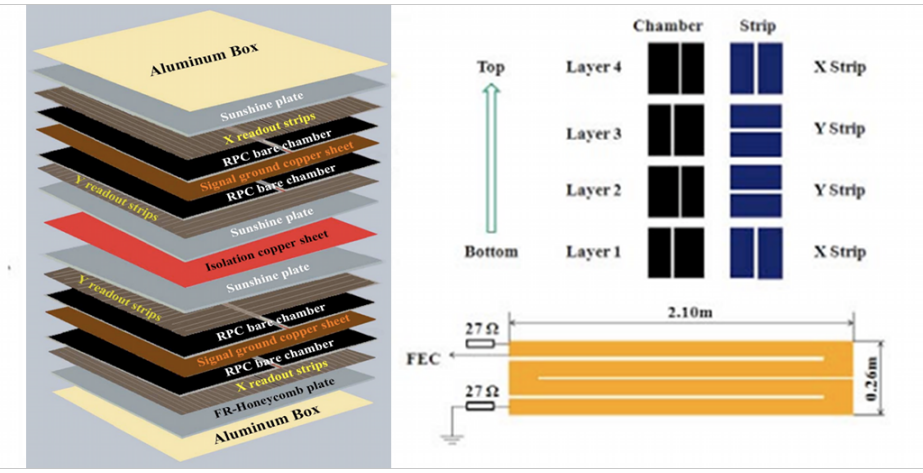

Figure 4.5: Structure of an RPC.

4.6.2 Resistive Plate Chambers (RPC)

To supplement the water Cherenkov detectors and to allow cross-calibration between muon tagging systems, an array of RPC modules are laid on top of the water pool in each site. 54 modules are installed in each of the near sites, and 81 in the far site. In addition, some more RPC modules, known as telescope RPC modules, are also installed about 2.0 m above the RPC arrays for better understand muon direction. An RPC module consists of 4 layers, and each layer contains 8 readout strips which are aligned to either X-direction or Y-direction.

4.7 Target Protons

As discusses in Chapter 2, the number of protons in the target region is one of the major sources of uncertainty. This can be accurately measured during filling and during data taking. By target protons, we mean the number of protons inside the target region: the IAV with radius of ∼3 m and height of ∼3 m. The number of target protons can be written as,

$$N_p = M_{target} \times \rho_{p/kg}$$

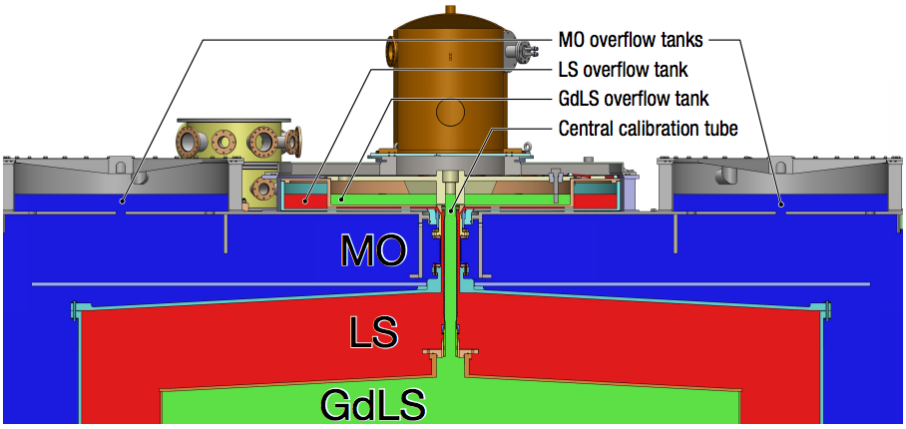

Figure 4.6: Cut-out showing overflow tanks and the bellows [22].

where N_p is the number of target protons, M_{target} the mass in the target volume and $\rho_{p/kg}$ the number of protons per kg of GdLS. The value of $\rho_{p/kg}$ can be measured by chemical means, while the target mass, M_{target} can be broken down into several components:

$$M_{target} = M_{total} - M_{overflow} - M_{bellows}$$

$$M_{overflow} = V_{overflow}(H) \times \rho_{kg/L}$$

$$M_{bellows} = V_{bellows} \times \rho_{kg/L}$$

where, M_{total} is the mass of GdLS being filled into the AD, $M_{overflow}$ and $V_{overflow}(H)$ respectively the mass and the volume of GdLS in the overflow tank filled with GdLS of height H, $M_{bellows}$ and $V_{bellows}$ respectively the mass and the volume of GdLS in the bellows connecting the IAV to the overflow tanks, and $\rho_{kg/L}$ the mass density of GdLS.

In other words, the number of target protons could be deduced by determining these quantities:

- $\rho_{p/kg}$: Number of proton in one kg of GdLS.
- $\rho_{kg/L}$: Mass density of GdLS.
- M_{total}: The total mass of GdLS filled into the detector
- $V_{overflow}(H)$: Volume of GdLS in the overflow tank
- $V_{bellows}$: Volume of GdLS in the bellows

AD	F_P
1	$12.01 \pm 0.42\%$
2	$11.97 \pm 0.47\%$
3	$11.95 \pm 0.66\%$
4	$11.95 \pm 0.46\%$
5	$12.00 \pm 0.30\%$
6	$11.97 \pm 0.46\%$

Table 4.2: Mass fractions of hydrogen atoms determined by combustion analysis.

Proton per kg of GdLS ($\rho_{p/kg}$) The mass fractions of hydrogen atoms, F_P, in AD1 to 6 were determined to be around 12% with combustion analysis (as shown in Table 4.2). The results of these measurements match with the expected number, 11.77%, determined with theoretical calculation. The proton density of GdLS, $\rho_{p/kg}$, can be calculated as,

$$\rho_{p/kg} = \frac{F_P}{m_p}$$

where m_P is the proton mass.

Mass density of GdLS ($\rho_{kg/L}$) The mass density of GdLS, $\rho_{kg/L}$, which changes as a function of temperature (T), can be described as

$$\rho_{kg/L}(T) = \frac{\rho_0}{1 + \beta(T - T_0)}$$

where $T_0 = 19°$C, ρ_0 is the density of GdLS at T_0, β is the volumetric thermal expansion coefficient of GdLS at T_0. With the temperature sensors installed in the overflow tank, the mass density of GdLS is determined with the measured temperature. The uncertainty in $\rho_{kg/L}$ is negligble.

Total mass (M_{total}) The total mass of GdLS, M_{total}, filled into the detector is measured in the filling stage. GdLS is pumped from 5 storage tanks into an intermediate isolation (ISO) tank, equipped with load cells which monitor the weight of the GdLS in the ISO. The flow rate was also measured with a Coriolis flow meter as a crosscheck. The main source of uncertainty comes from the drift in load cell reading. The load cell readings could drift up to 3 kg in several hours [95]. The total uncertainty in M_{total} is estimated to be 0.015%.

Volume of overflow tanks and bellows ($V_{overflow}(H)$, $V_{bellows}$) Given the dimensions, the volume of GdLS in the bellows, $V_{bellows}$, can be accurately calculated, since the bellows are always

completely filled with GdLS. The uncertainty is estimated to be 0.0025%. The volume of GdLS in the overflow tank has to be monitored with various sensors. The measurement of liquid height in the overflow tank is primarily done with an ultrasonic sensor, which infers the distance to the liquid surface from the reflected ultrasonic waves. Knowing the geometry of the overflow tank, the volume of GdLS can be calculated. Some capacitance sensors are employed to cross-check the volume measurement. Tilt sensors are also used to account for any possible non-levelness of the detector. Uncertainties in the overflow tank geometry, sensor calibration and tank tilt are estimated to be 0.0066%, 0.0057% and 0.0068% respectively.

4.7.1 Uncertainty in Target Proton Number

The correlated uncertainty in target proton number is dominated by the uncertainty in the number of protons per kg of GdLS, which is, in turn, due to the uncertainty in mass fraction measurements. However, the uncorrelated uncertainty is largely due to the uncertainty in total mass. The uncertainties related to target proton number is tabulated below:

Quantity	Correlated Uncertainty [%]	Uncorrelated Uncertainty [%]
Protons per kg ($\rho_{p/kg}$)	0.47	negligible
Mass density of GdLS $\rho_{kg/L}$	negligible	negligible
Total mass (M_{total})	0.015	0.015
Overflow tank geometry (part of $V_{overflow}(H)$)	0.0066	0.0066
Overflow sensor calibration (part of $V_{overflow}(H)$)	0.0057	0.0057
Overflow tank tilt (part of $V_{overflow}(H)$)	0.0068	0.0068
Bellows Capacity ($V_{bellows}$)	0.0025	0.0025
Combined	0.47	0.019

Chapter 5

The Automated Calibration System

The calibration system aims to calibrate energy and timing responses of the AD (See Chapter 7 for discussions on event reconstruction). It is also designed to monitor the stability of the AD responses on a regular basis.

The focus of this chapter is on the control software and the performance of the calibration system. (For more details of the calibration system, see [96].

5.1 Design of the Automated Calibration Units (ACU)

Each ACU consists of a stainless steel turntable with three sets of motors and wheels (also known as deployment axes). Each axis is capable of deploying a source (radioactive sources or LED) into the detector along the vertical axis (z-axis). For each ACU, access to the detector is provided through a single port on the lid of the detector.

Each deployment axis is essentially a driving unit (which consists of a motor, a 50:1 gear-box, a main deployment wheel, and an auxillary deployment wheel) attached to a source. Each source is enclosed in an acrylic capsule which is attached to the wire wound into the grooves on the main deployment wheel. To ensure material compatibility with the liquid scintillator, both the coaxial cable for the LED axis and the stainless steel wire are Teflon-coated.

The turntable consists of a stack of three stainless steel plates. Mounted on the top plate are

the driving units, and the middle plate houses shielding cylinders in which the sources are stored. The bottom plate supports the whole ACU and, at the same time, acts as a reservoir for the liquid scintillator that adheres to and drips from the source enclosures.

The top and the middle plates can turn clockwise or counter-clockwise as a single unit and are controlled by a motor mounted at the center on the top plate. The bottom plate has a one-inch diameter penetration through which the ACU sources are deployed into the detector volume.

All these mechanical parts and electronic components are sealed from water by a stainless steel bell jar with double o-ring. Employed between the ACU bottom plate and the support spool on the AD lid is another double O-ring which can be pumped out for leak checking and hence ensuring seal quality.

5.2 Design of the Control Software

In the design of the control software, the main focus was to balance safety and automation. From the safety point of view, the control software has to prevent or stop operations which can cause harm to the system, while, to achieve genuine automation, it cannot completely rely on human intervention when potentially dangerous situations arise. However, whenever there is a conflict, safety always comes first at the expense of automation.

5.2.1 Design

The control software consists of several application modules written in LabVIEW. This modular (as opposed to monolithic) nature of the software minimizes coupling between parts and simplifies the customization for each site. The central piece is the Main Program which consists of two independent but coupled parts (or loops). Each performs a crucial function: the "Monitor Loop" periodically monitor sensor readings and the "Control Loop" direct signals to the electronics to control source motions. The Main Program also provides the main interface for user operation. The Data Fetcher fetches readings from the sensors, e.g. load cells and encoders, and provides such readings to the main program. The Watchdog ensures that the Main Program always duly performs

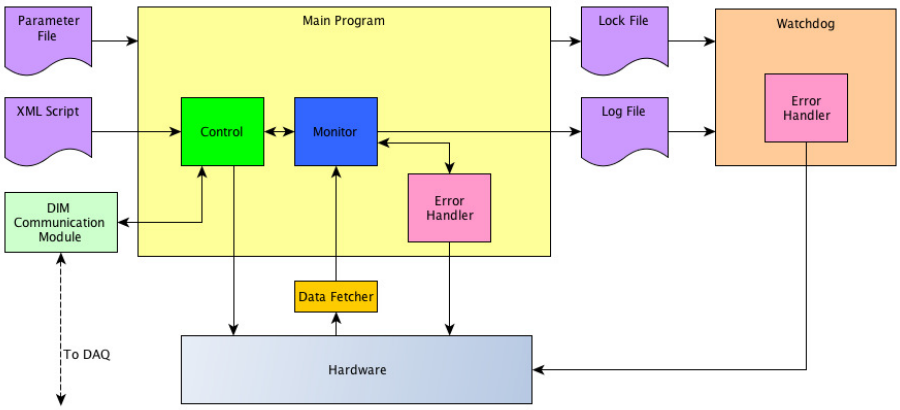

Figure 5.1: Structure of the control software.

its monitoring function. The Distributed Information Management (DIM) Communication Module relays information between the main program and the data-acquisition system (DAQ) over TCP/IP, enabling automatic deployment. The detailed workings of the software will be discussed below from a functional point of view.

5.2.2 Monitoring

Involved in the monitoring function of the software are the Monitor Loop in the Main Program, the Data Fetcher and the Watchdog. The Data Fetcher fetches readings from all sensors (See Table 5.1) from the hardware at the highest possible frequency allowed under computer and hardware contraints. The readings are then transmitted to the Main Program via a local DataSocket server. On receipt of the readings, the Monitor Loop will look for signs of danger and issues alarms if any such signs are observed (see Table 5.2). When an alarm is issued, the Main Program will signal all motors to stop and power down. After processing this set of readings, the Main Program then signals the Data Fetcher to clear the latched set of readings and to read in another set. Such a cycle typically runs at 1 to 2 Hz.

To provide an additional layer of security, the Monitor Loop is constantly watched over by the Watchdog, making sure that the Main Program is running and updates the log file at a fixed frequency (typically 1 Hz). An alarm will be issued when this frequency is not met.

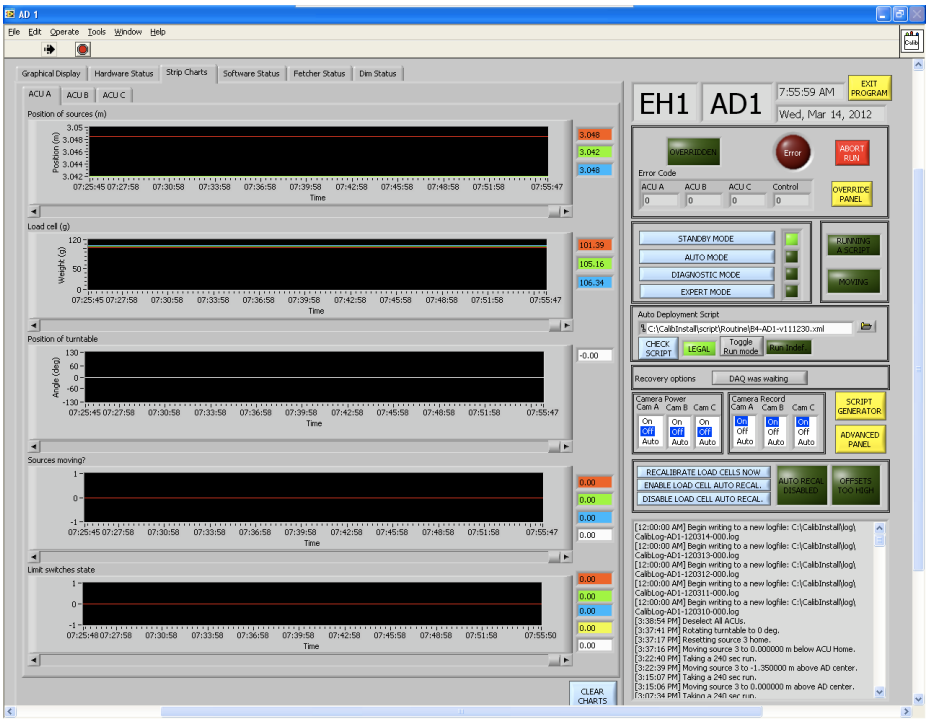

Figure 5.2: Screenshot of the Main Program.

Variable name	Axis	Type	Unit
Stepper count	All	Int	Counts
Encoder count	All	Int	Counts
Load cell reading	All	Double	Volts
Motion status	All	Bool	-
Reverse limit switch status	All	Bool	-
Forward limit switch status	Turntable	Bool	-

Table 5.1: Sensor readings from each ACU.

Bit	Name	Remarks
1	Turntable stepper/encoder mismatch	Tolerance = 0.6 deg
2-4	Source 1-3 stepper/encoder mismatch	Tolerance = 2.5 mm
5-7	Source 1-3 reaches maximum depth	IAV bottom or OAV bottom
8-10	Source 1-3 load cell out of limit	below 50% of or 300 g above nominal weight
11	Source moves when turntable is misaligned	Prevent misoperation
12	Turntable moves when some source is deployed	Prevent misoperation
13	More than one motor move simultaneously	Prevent misoperation
14-18	Inconsistent status	Ensure internal consistency
19-21	Load cell saturated	Load cell offset < -9.0 V

Table 5.2: List of alarms issued by the Main Program

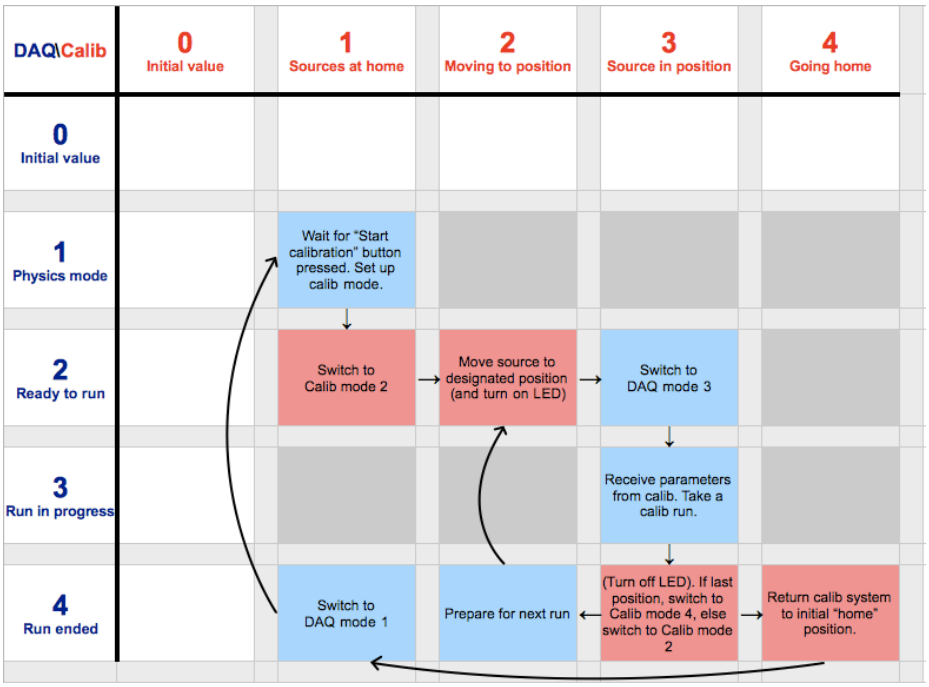

Figure 5.3: Communication protocol between the control software and DAQ. See text for details.

5.2.3 Control

The Control Loop of the Main Program provides 3 modes of operation: Manual, Diagnostic and Auto, for controlling the four axes (1-3 for deployment axes and 4 for turntable) of motion for each ACU, and the voltage and frequency of the LEDs. The Manual mode is restricted to expert use for non-standard deployments, which requires point-and-click by the user. Any possible operation can be performed unless forbidden by the Monitor Loop. The Diagnostic mode and the Auto mode accept an XML script which specifies the sequence of operations to be performed. In Diagnostic mode, the Control Loop simply performs each operation in the XML script sequentially until the end of the file. In the Auto mode, the Control Loop and the Daya Bay DAQ system communicate via DIM. Both systems publish their status on a dedicated DIM server, and listen to the other side with a handshaking protocol depicted in Figure 5.3. Control Loop listens to the DAQ for the shifter's "Start" signal before deploying any source. The Control Loop signals the DAQ to start a run when the source reaches the designated position and the DAQ replies to the Control Loop when the DAQ run is done. The Control Loop then executes the next command (if there is any) in the XML script,

performs the above "handshake" and repeats until the end of the XML script, at which point the Control Loop informs the DAQ of the end of calibration and returns to the initial state. When an error occurs during Auto mode, the DAQ is notified, and after recovery the calibration can resume from the place where it left off without any intervention from the DAQ side in most cases. With this method, after the shifter commences the weekly calibration program, the entire program (typically 5 hours by deploying three sources in each ACU, one at a time, 3-5 stop per round trip) in all three halls and eight ADs are executed simultaneously with fully automated data taking at one data run per source stop in each hall.

5.2.4 Notification and Logging

There are several channels employed in the software for notification. When an alarm is issued, the Main Program signals the detector-control system (DCS) via DIM, which notifies the shifter. On the other hand, the Main Program also sends an email notification to the experts with a summary of alarms issued (See Table 5.2) and recently executed commands, to expedite the recovery process. While all sensor readings are saved onto the local disk, only a subset of monitoring-related readings are saved in the DCS database, while another subset of control-related readings are saved to the online database via DAQ.

5.3 Quality Assurance and Calibration

5.3.1 Mechanical Reliability Tests

The Daya Bay experiment is planned to run for at least three years, with the automated calibration units running on a weekly basis over this period. This amounts to at least 156 full calibration cycles for each ACU. We constructed in total 25 (24 and a spare) ACUs. To ensure the robustness of the ACUs, longevity tests were undertaken at the California Institute of Technology before shipping to Daya Bay. The longevity test involves running the ACU for 200 consecutive full deployment cycles. Each cycle involves deploying each of the three sources to a distance corresponding to the detector

center, and then retracting back to the origin. Each cycle took about half an hour, and a complete longevity test for each ACU took about four days. No noticeable damage was found in any of the parts after the longevity tests.

Two different stress tests were also performed to emulate situations where parts of ACUs are damaged. One stress test, dubbed the "extreme test", targeted the limit switch and the load cell, involves forcefully pulling the source assembly against a disabled limit switch until the stepper counts gets out-of-sync with the encoder counts. This forceful pull was repeated at least 200 times for each of the axes. The objective of this test was to make sure that the functionality of the limit switch and the load cells would not be affected under such an extreme condition. The other, called "load test", aimed at ensuring secure attachment of the sources, involves hanging a weight of about 1 kg (maximum possible pull from the motor) from the source assembly for a duration of at least 15 minutes. No source ever failed any of these tests.

5.3.2 Position Calibration

Source deployment positions are required to have an accuracy of 0.5 cm. The elongation of the stainless steel wire due to the weight of the sources is negligible, this positional accuracy is primarily determined by the accuracy in the diameter of the acrylic wheel. There are also some small effects coming from the depth of the grooves into which the wires are wound and the alignment between the deployment wheel and the auxiliary wheel. Given that a deployment to the center of the detector typically requires 4 turns of the wheel, uncertainty in the deployment length can be more than an order of magnitude greater than that of the wheel diameter. Therefore, a sub-mm uncertainty in the wheel diameter can possibly jeopardize the required accuracy. We devised a method to precisely estimate the effective diameter of the wheel. We constructed a calibration ruler, with accurately measured marks, aligned along the source deployment axis. The positions of the source can then be compared with the marks on the ruler. Hence, an effective diameter of the wheel can be estimated accurately with a linear fit.

The calibration ruler is made of a roughly 6 m long Teflon coated stainless steel wire, with a 50 g

weight attached to one end. Six crimps which served as calibration marks were attached at various measured positions on the wire. The ruler was then lowered into a mock-up detector, a 5.5 m long acrylic tube, on which we marked the positions of the crimps. We then offset the ruler by 200 mm, and a different set of calibration marks were similarly translated onto the tube. We also used the top surface of the turntable as a calibration point.

For each axis, the source was first deployed close to each calibration mark. The source was then made to inch along the axis in steps of about 0.1 mm. The encoder counts of the source motor was recorded when the source was flush with the calibration mark.

The data were then subject to a linear fit of the form $y = kDx + C$, where $k = \frac{\pi}{4000 \times 60}$ (4000 is the encoder count/resolution, and 60 is the gear ratio), x and y are respectively the encoder counts and position of calibration marks, and the fit parameters D and C are respectively the wheel diameter and the offset.

Figure 5.4 shows the distribution of wheel diameters with an average of 227.7 mm. Most of the wheel diameters are in good agreement within 1 mm, except for ACU5A axis 3, which is ∼3 mm smaller in diameter compared to the rest due to machining. One also observes from Figure 5.4 that on average the effective diameter for axis 1 is ∼0.4 mm larger than those for axes 2 and 3, which is consistent with the different diameters of the deployment cables (0.039" for LED, 0.026" for radioactive sources).

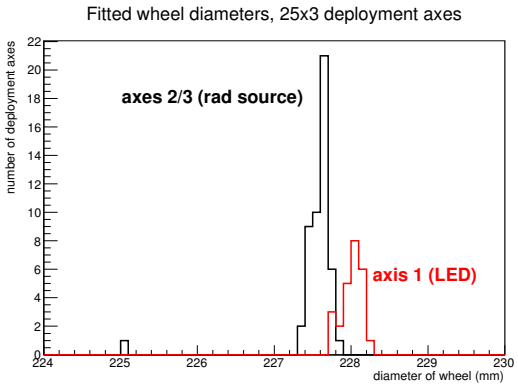

Figure 5.4: Effective wheel diameters of all 25×3 ACU axes obtained by the position calibration.

The expected positions for each encoder reading is calculated using the parameters determined.

For example, the difference between the expected and the actual positions on the ruler for ACU1A, deployment axis 1, as a function of vertical deployment length is shown in Figure 5.5. The variation in this difference (RMS) is used as a measure of the positional accuracy for each deployment axis.

Using such method, the distribution of the position accuracy can be determined for all 25×3 deployment axes, including those on the spare ACU, as shown in Figure 5.6.

The position accuracy of the calibration source to its limit switch is conservatively estimated to be 2 mm. As a final cross-check, the obtained wheel diameters were input into the control software, and each source was deployed to the nominal AD center in the mock detector. The position of the source and the marker on the ruler agree within 3 mm.

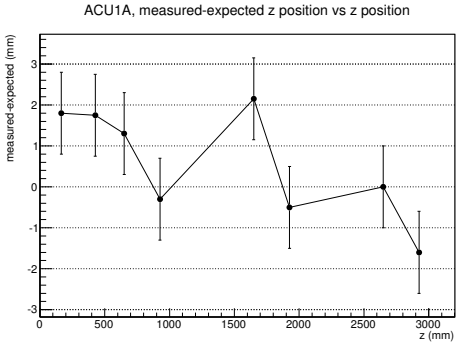

Figure 5.5: Difference between the expected (software) and true position, ACU1A source 1.

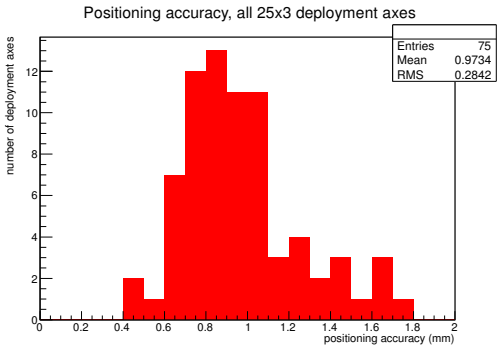

Figure 5.6: Position accuracy for all deployment axes.

The positional accuracy determined above (Figure 5.6) is in the vertical direction only. To find the absolute source accuracy of a deployed source within an AD involves 1) the ACU mounting position relative to its support flange, 2) the AD verticality, and 3) the position of the ACU support flange relative to the general AD coordinate. Given the size of bolt holes on the ACU bottom plate, the accuracy in 1) is $\sim$ 2mm in the horizontal plane. The accuracy in 2) and 3) can be obtained from the AD survey data [97], which translate to an absolute accuracy of $<$1 mm in x, y, and z coordinate. Summing these up in quadrature, we reach a final $\sim$ 4 mm position accuracy of a source in the AD.

5.4 Performance

The performance of the antineutrino detector with calibration sources has been thoroughly described in [28]. In this section, we will show results more directly related to the performance of the calibration system.

5.4.1 Motion/Sensor Performance

All ACUs have been fully functional since the beginning of Daya Bay data taking. Alarms only occur infrequently, at a rate of $\sim$ 2-3 per week for the entire system. All of these alarms were identified as transient noise pick-up by the sensors, for example, load cell readout could pick up noise occasionally and triggered an alarm during motor movement.

Figure 5.7 shows the load cell reading during a typical source deployment. As the source dips into the liquid, the liquid buoyancy would cause a $\sim$ 30 g change in the load cell reading.After the source assembly completely submerged into the liquid, the load cell reading gradually increases as more and more cable unspools and adds to the weight felt by the load cell. It then stops at the target position and data taking begins. After that, the source is retracted by reversing the motor direction, which causes a sudden increase in load by about 10 g. This is due to an additional dynamic friction that has to be overcome. The load gradually reduces as the cable respools until the source assembly emerges from the liquid surface, and is no longer lifted by the buoyant force. The load cell reading then returns to roughly the original level. A small decrease in load can be seen thereafter, due to dripping of liquid back into the detector. The control software then resets the motor to home by moving the source up until the limit switch is activated by the top weight, at which point a spike in the load cell reading can be seen. The source is then "parked" by moving down by 5 cm. The load cell also tends to pick up noise, which typically translates to about a couple of grams, from motors nearby as shown in Figure 5.7.

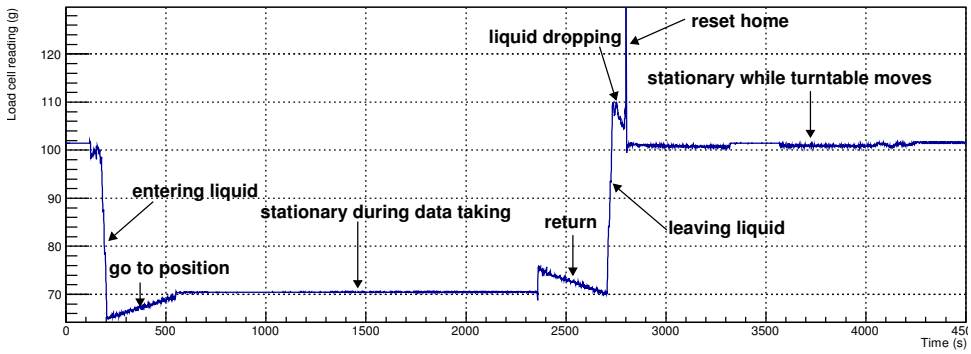

Figure 5.7: Strip chart of the load cell reading for a typical source deployment.

5.4.2 Calibration Runs during the AD Dry Run

The LED source and the ^{137}Cs scintillator ball played an important role in detector commissioning, in particular the "dry run" before liquid scintillator filling.

LEDs can be used to mimic real particle interactions and this allows for a study of detector electronics. Figure 5.8 shows the measured total charge in an LED intensity scan in an AD. Events ranging from gamma-like low energy events to muon-like high energy events could be easily simulated by adjusting the driving voltage of the LED, given a typical AD energy scale of 160 PE/MeV [28].

Low energy events allow for precise determination of PMT gains, and the high energy events allow for the study of the effect on PMT/electronics due to a large pulse, including baseline overshoot, ringing and recovery, as well as retriggering.

Timing calibration is facilitated by the narrow timing distribution of the LED flashes relative to the trigger signal, in particular the rising edge of the light pulse. In Figure 5.9, the TDC distribution of a PMT channel (relative to the trigger signal generated by the TTL command pulse) is plotted for a high (black) and low (red) light intensity run. This narrow (RMS $\sim$ 0.9 ns) TDC distribution in the high intensity run demonstrates that the emitted light pulse has a very sharp rising edge. The timing calibration data for all ADs were collected with LEDs pulsing at high intensity.

The TDC spectrum in the low intensity run reveals the overall emitted photon timing distribution. The primary pulse has a FWHM of 5 ns. The late light from the LED can be observed as a tail which lasts for about 25 ns from the initial edge. The difference in peak time between the two

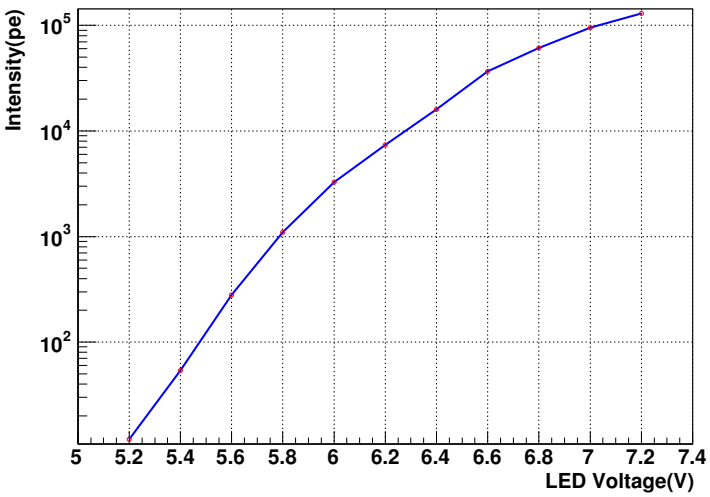

Figure 5.8: Detected light intensity (in number of PEs) as a function of LED control voltage.

distributions is due to time-walk.

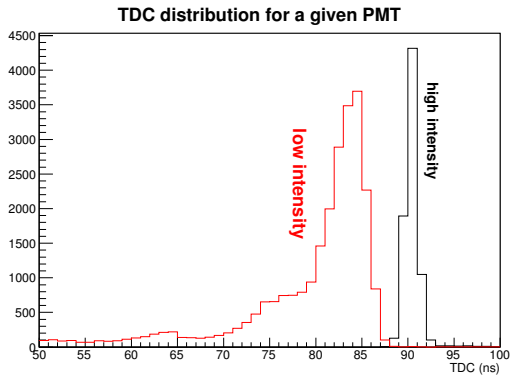

Figure 5.9: TDC distribution of a PMT during a high (black) and low (red) LED intensity run.

However, the LED source is not perfect for all studies. Due to the difference in cable length in the spool, the LED intensity could fluctuate by a few percent as a function of position. Therefore, we need some other stable "candle" for position-dependent uniformity studies of the dry detector and the solution was the ^{137}Cs scintillator ball.

^{137}Cs, which primarily beta-decays into ^{137m}Ba which has a half-life of 2.552 m, is deposited at the center of a spherical scintillator. ^{137}Cs emits K (624 keV) or L (656 keV) shell conversion electrons with a branching ratio of about 10%. The scintillation light produced by these electrons would then provide a stable light source. The source is fabricated at the China Institute of Atomic

Energy with 900 Bq of ^{137}Cs following the design shown in Figure 5.10, as well as a photo of the scintillator ball in real-life during dry-run preparations.

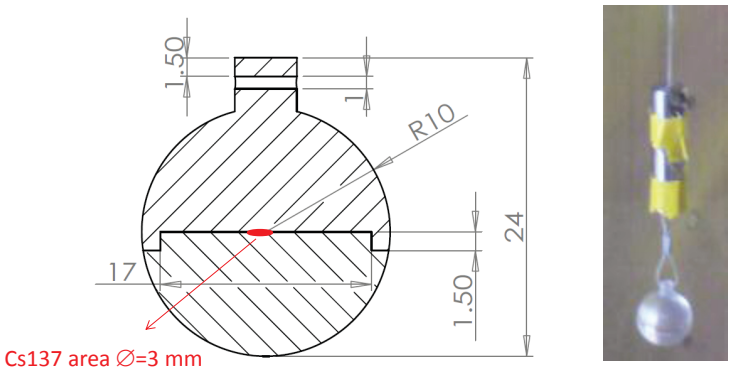

Figure 5.10: (Left) Design of the ^{137}Cs scintillator ball; (right) Photo taken during dry run.

The measured total charge spectrum with the scintillator ball deployed at the detector center is shown in Figure 5.11. A conversion electron peak can be clearly observed around 90 photoelectrons.

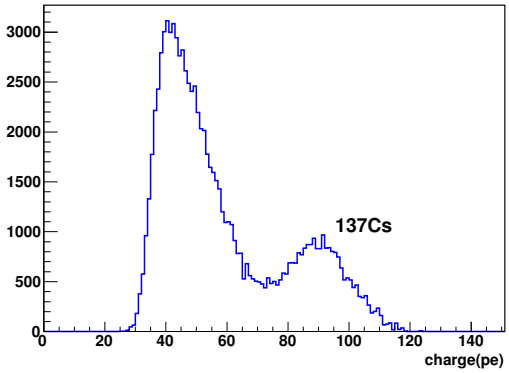

Figure 5.11: Energy spectrum of ^{137}Cs scintillator ball in a dry AD.

5.4.3 Radioactive Sources Calibration in-situ

The ^{241}Am-^{13}C/^{60}Co source and the ^{68}Ge, source spectra in a filled AD are shown in Figure 5.12. On the ^{241}Am-^{13}C/^{60}Co spectrum, the full absorption peak around 2.5 MeV due to ^{60}Co and n-Gd capture gamma peak can be seen. Both of them can be used to calibrate the PE to MeV conversion factor of the ADs. In addition to the n-Gd capture peak, the low energy peaks on the spectrum were also attributed to the gamma lines (662, 722 keV) from ^{241}Am. However, the n-H capture from

the Am-C source cannot be observed on the spectrum due to the dominance of the ^{60}Co decay rate (100 Hz vs 0.7 Hz of Am-C) and the finite energy resolution of the AD. Moreover, effects of the n-H capture have negligible effects on the ^{60}Co 2.5 MeV peak. Note also that low energy shoulders due to non-scintillating material on the source assembly can be seen on both spectra.

The variations of the energy scale among all six ADs have been limited to within 0.5% [28]. A 2.5 MeV peak can be seen in the ^{68}Ge spectrum, which could come from imperfect control of the fabrication environment, where ^{60}Co contaminants were likely introduced. However, it does not affect effective application of this source.

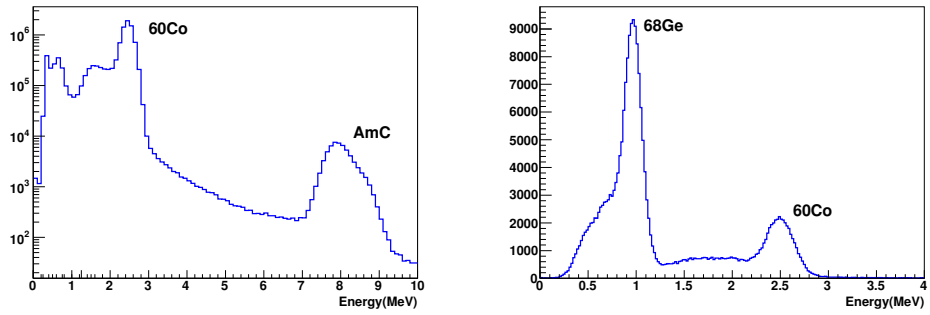

(a) AmC-^{60}Co (b) ^{68}Ge

Figure 5.12: Energy spectrum of the ^{241}Am-^{13}C/^{60}Co source (a) and the ^{68}Ge source (b) when deployed at the AD center.

Accurate knowledge of the true position of the ACU sources provide stringent constraints to the vertex reconstruction (Section 7.3) as well as vertex based energy correction (Section 7.4). These will be discussed in the relevant sections.

Chapter 6

Data readout and data quality

In this chapter, I will describe the data readout chain and data quality checks.

6.1 Data Readout Chain

The data readout chain can be divided into three parts: front-end system, trigger system and the data acquisition (DAQ) software.

The front-end system directly interfaces to the detector components, such as PMTs and RPCs. Raw signals are read out. Partial trigger signals are generated and are sent to the trigger system.

The trigger system determines if the signals from the front-end meet the trigger condition. If so, the trigger system would signal the DAQ software to record the data.

The DAQ software integrates the data from all detectors and save the data into the database for quality check and further processing. It is also responsible for coordinating with other systems in routine calibrations.

6.1.1 Front-end System

The front-end system consists of VME-based front-end electronics boards (FEE).

There are two types of FEE boards, one for the PMTs and the other for RPCs. Here I only discuss the PMT FEE boards.

Every PMT FEE board has 16 channels, each of which serves one PMT. When entering the FEE, the PMT signal first goes through the discriminator. The discrimator threshold is set to be 0.25

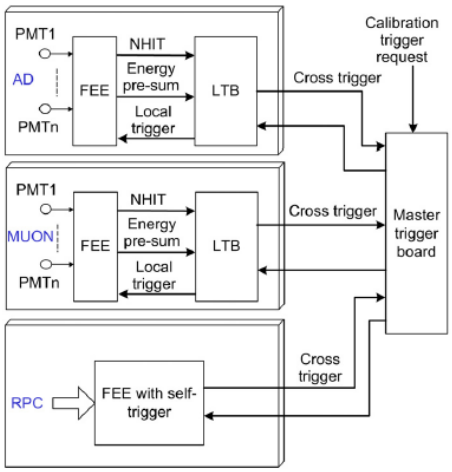

Figure 6.1: Trigger system

photoelectrons (PE). If the PMT charge signal is above the threshold, it is considered a "hit". Each channel is equipped with a TDC in common stop mode for recording the time of arrival of the PMT signal; and two 12-bit ADCs, one fine gain and the other coarse gain, for reading out the charge at 40 MSPS. The TDC has a time resolution of 1.5625 ns. The PMT signals are first amplified and are then sent to the CR-$(RC)^4$ shaping ciruits where the pulse is integrated to give the total number of PEs. Low charge signals ($< 160\ pC$ or 100 PE) are sent to the fine gain ADC, while high charge signals ($> 160\ pC$ or 100 PE) are sent to the coarse gain ADC. The fine gain ADC has a gain of about 19 ADC counts per PE, while the coarse gain ADC gives about 1 ADC count per PE.

The FEE produces two signals: multiplicity (NHIT) and energy pre-sum (ESUM). The NHIT represents the number of coincident PMT hits in each 100 ns time window, while the ESUM contains the analog sum of the 16 PMT signals. These two signal are passed to the local trigger board (LTB) for trigger logic processing.

6.1.2 Trigger System

The trigger system consists of local trigger boards (LTB) and master trigger boards (MTB). The LTBs collect and process signals from the FEEs and would generate triggers that are then sent to the MTB. The MTB at each site relay information among the LTBs and interfaces with external trigger sources.

The trigger system distinguishes between two types of triggers: physical and external.

Examples of physical triggers are the multiplicity (NHIT) trigger and the energy sum (ESUM) trigger. These triggers are generated by the LTB after combining the partial trigger signals from all FEE boards that it serves. An LTB can serve up to 16 FEE boards, meaning that one LTB can accomodate an AD.

External triggers are triggers that are issued by the MTB. These include cross triggers and calibration triggers. Cross triggers are initiated by LTB, requesting readout of other LTBs. Calibration triggers are issued by the calibration system, signaling the LTBs to read out.

6.1.3 DAQ Software

The DAQ software is a set of computer programs that run on a blade server based computing farm. The DAQ software can run under different run modes: physics mode for regular data taking and AD or water shield calibration modes for routine calibrations. Detectors in the same site can be separated into partitions, so that each detector can run in different modes. For example, during AD calibration the muon detectors can continue to run in physics mode, providing an active muon veto.

6.2 Data Readout Performance

The behavior of the data readout chain can have effects on the final θ_{13} analysis in several ways.

6.2.1 Blocked Triggers

When the trigger rate is high, the triggering electronics can become "dead" due to full buffers. As a result, triggers that occur when the buffer is full are blocked and not recorded. This reduces the overall livetime of the experiment.

When the buffer is full, the trigger electronics would still produce triggers if the trigger condition is met, and the number of these blocked triggers is recorded by the DAQ. By taking the ratio of block triggers over the total number of triggers, we can estimate the dead time. This ratio is calculated to be $<0.003\%$, which means this has negligible effects.

6.2.2 Trigger Efficiency

The energy deposition of a particle can have an intrinsic spread. Effects due to detector geometry or electronics also contribute. Therefore, some events which we wish to detect could fail to produce a trigger. This impacts the overall detection efficiency.

The trigger efficiency can be estimated using the source ^{68}Ge [98]. The characteristic 1.022 MeV positron annihilation energy from ^{68}Ge was used as a proxy for the prompt signal of an IBD. By running the detector at two thresholds OR'ed, one at a low level, the other at the level of interest, the ratio of ^{68}Ge events that pass both thresholds to those that only pass the low threshold could be calculated. It was found that an efficiency of $99.9 \pm 0.02\%$ can be achieved.

6.3 Data Quality

All data taken went through the data quality check procedure, in order to reject data deemed unsuitable for physics analysis. The data is organized into runs; and runs are made up of run segments (also known as run files). A run segment, consisting of about 5 minutes of data, is the smallest unit of data that the data quality procedure works on - if a problem is found in a segment, the whole segment is discarded.

6.3.1 Criteria for Good Data

Each run segment is evaluated based on various low-level (electronics) and high-level (physics) quantities. The inclusion of a run segment into the list of good runs is "loose", meaning that segments are discarded only when we are confident that it is bad.

The followings are some general criteria for evaluating the quality of a segment of data.

Trigger rate stability Trigger rate can fluctuate due to interference from other electrical devices, for example, cranes, pumps or other electrically noisy instruments. Run segments showing excessively low or high trigger rates are tagged as "bad", meaning unsuitable for analysis.

Blocked trigger Some run segments with unusually high fraction of blocked triggers are removed from the list of good runs.

Time ordering of events Some run segments are found to have triggers which are not properly ordered in time. These run segments are discarded.

Rates of physics events Some higher-level quantities, such as, IBD rate, spallation neutron rate, flasher rate (See Section 7.2 for discussion on flashers), are also examined. However, extra attention was paid when discarding run segments in which an anomalous high-level quantity is identified, to avoid introducing unnecessary bias. In fact, analysis algorithm further down the analysis chain should be capable of resolving such scenarios.

6.3.2 Synchronicity

For θ_{13} analysis, we should only include data where all three halls are taking data at the same time. Asynchronous data appear because among the three halls, there could be differences in the duration of calibration or the data in one hall is marked as bad, etc. To remove asynchronous data, a synchronization procedure is done to discard the portion of data that were taken when not all three halls are running.

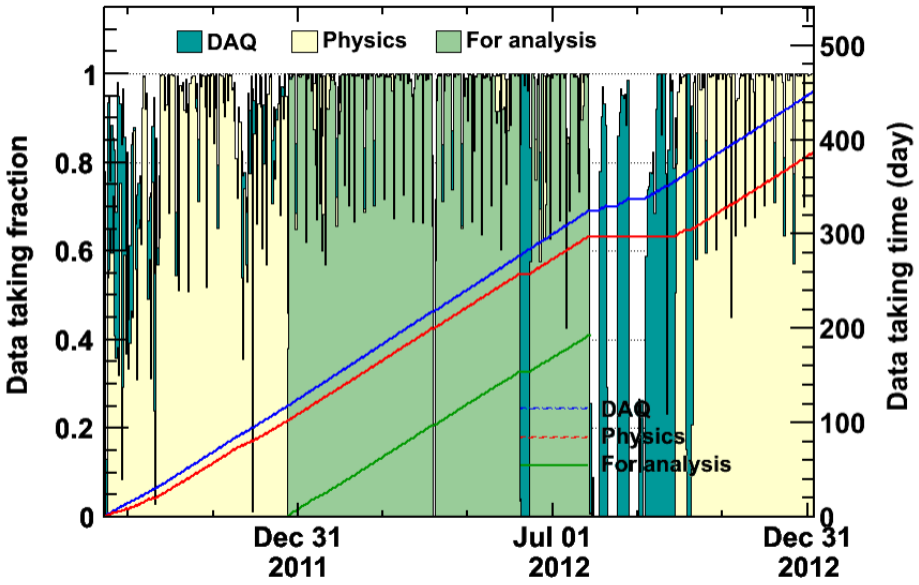

Figure 6.2: Live time in EH1

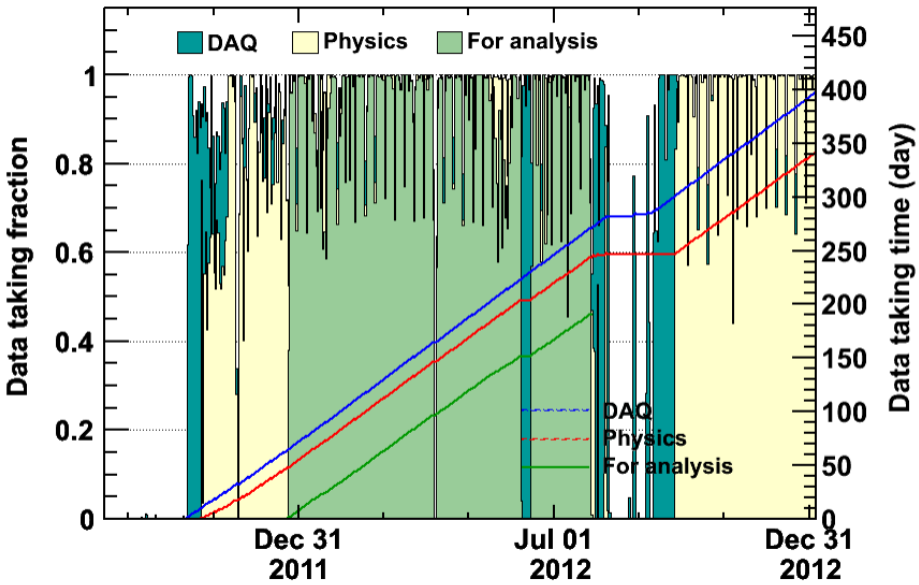

Figure 6.3: Live time in EH2

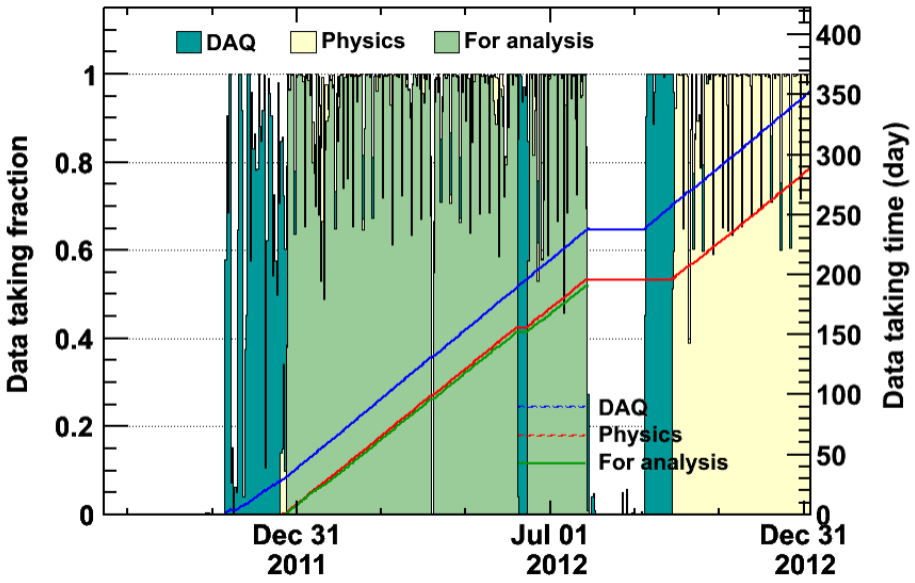

Figure 6.4: Live time in EH3

Chapter 7

Event reconstruction

The raw output of the AD is simply a collection of hits, where a hit is just a pair of ADC and TDC counts. These have little direct physical meaning with regard to antineutrino detection. The purpose of reconstruction is to extract physics events by understanding these hits. The first step involves converting ADC and TDC counts in each trigger into charge and time (Section 7.1 PMT Calibration). Using these charge and time information, we can then determine the energy and vertex of the physical interaction (if it is the case) which caused these triggers (Section 7.4 Energy and Section 7.3 Vertex Reconstruction). Finally, the collections of triggers can be classified into various categories of physics events (See Chapters 8 and 9).

7.1 PMT Calibration

7.1.1 Gain Calibration

In order to reconstruct the charge collected by the PMT from the ADC values read out at the FEE, we need to develop a mapping between the two. This mapping can be closely approximated by a linear function. (This has been confirmed to be accurate up to 200 p.e.) The gain refers to the proportionality constant of this linear function. The purpose of gain calibration is to determine this gain. To determine the gain, we need a model of the PMT.

7.1.1.1 PMT Model

A PMT can be considered to be composed of two parts, the photocathode and the dynode chain [99]. The photocathode converts a photon to photoelectrons with a certain probability. This probability is sometimes called quantum efficiency. This conversion process can be described as a Poisson process,

$$P(n;\mu) = \frac{\mu^n e^{-\mu}}{n!}$$

where n is the number of photoelectrons produced at the photocathode and μ is the quantum efficiency. The dynode chain amplifies the signal in stages. The overall amplification factor is typically 10^7 times. Although this is also a Poisson process, it can be approximated by a Gaussian,

$$G_n(x) = \frac{1}{\sigma_1\sqrt{2\pi n}}\exp(-\frac{(x-nQ_1)^2}{2n\sigma_1^2})$$

where x is the variable charge received at the end of the dynode chain, Q_1 is the mean charge received and σ_1 is the corresponding standard deviation of the charge distribution. Therefore, the overall PMT response can be described as the convolution of these two functions,

$$R(x) = P(n;\mu) \otimes G_n(x) = \sum_{n=0}^{\infty} \frac{\mu^n e^{-\mu}}{n!} \frac{1}{\sigma_1\sqrt{2\pi n}}\exp(-\frac{(x-nQ_1)^2}{2n\sigma_1^2})$$

Now what remains is to select appropriate ADC spectra and perform a model fit. Below are two ways to calibrate the fine gain ADC, and one way to calibrate the coarse gain ADC.

7.1.1.2 Fine Gain ADC: Low-intensity LED

One way to determine the gain involves deploying an LED from the ACU to the center of the AD and let it flash at a low intensity, such that every PMT detects mostly SPE [23]. Hits that lie in the main peak in the TDC distribution are selected. The gains can be obtained by fitting the PMT model to the ADC distribution.

7.1.1.3 Fine Gain ADC: Dark Noise

Another method is to use dark noise [24]. Instead of the main peak in the TDC distribution, we select the region before the mean peak which contains mainly dark noise. This way, dedicated calibration runs are not needed. Similarly, the gains can be obtained by fitting.

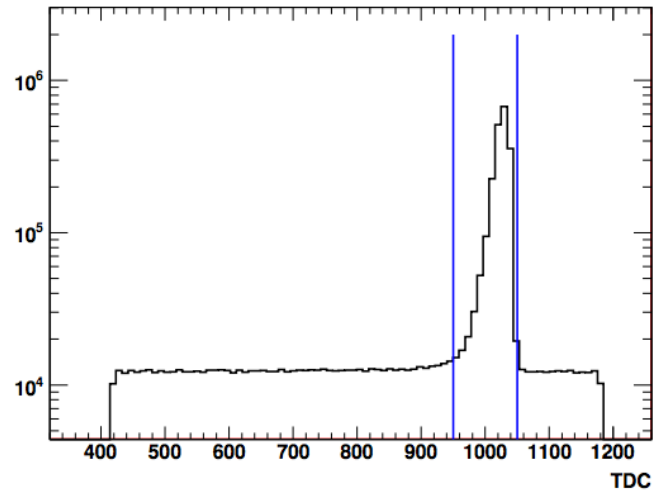

Figure 7.1: TDC distribution of LED calibration runs. The blue lines indicate the peak region. [23]

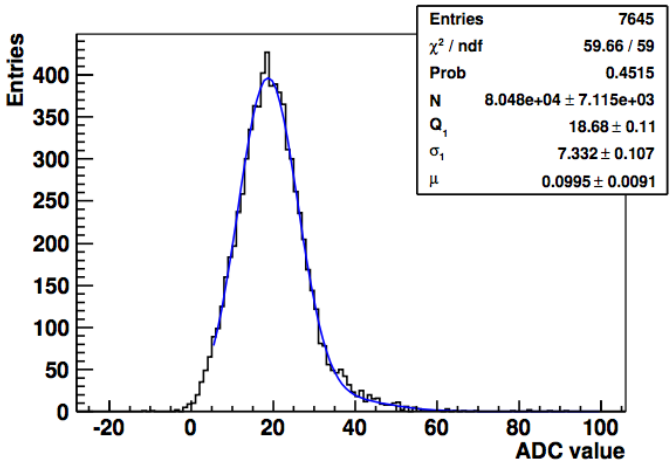

Figure 7.2: An example of SPE ADC spectrum fit using LED data. [23]

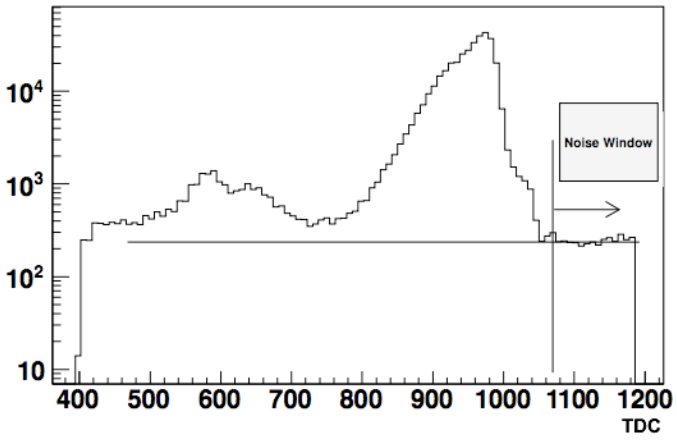

Figure 7.3: The arrow in the above TDC distribution indicates the region to be selected to calculate the rolling gain. [24]

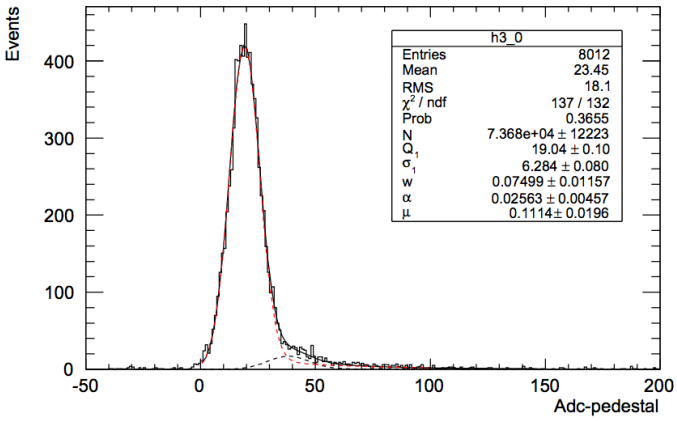

Figure 7.4: An example of SPE ADC spectrum fit using dark noise. [24]

7.1.1.4 Coarse Gain ADC

The coarse gain ADC is responsible for the signals with high energy ($\gtrsim$ 200 p.e.) such as muon events. The coarse gain ADC can be calibrated by using the self-test pulses from the FEE [100]. A range of pulse heights covering both the fine gain and coarse gain ADCs are generated by FEEs. The conversion factor from the pulse height to ADC counts for both ADCs can be determined. The ratio of these two factors can be used to estimate the gain of the coarse gain ADC from that of the fine gain ADC.

7.1.2 Pedestal

Even when the photocathode is not emitting photoelectrons, the ADC would still give a non-zero value. This is called the pedestal. Since the pedestal value fluctuates and drifts over time, periodic measurements are needed. Ususally, we can measure the pedestal with dedicated pedestal runs in which ADCs with no PMT hit are read out. However, using this approach, we will be susceptible to random fluctuations and drifts. To solve this problem, we measure it dynamically right before each ADC hit [101]. This dynamic pedestal, which is called preADC, is the average of 4 ADC values read out at 100ns, 75ns, 50ns and 25ns before the ADC peak, giving almost real time measurement of the pedestal.

7.1.3 Timing Calibration

Timing information is obtained by TDCs. Although the TDCs have high resolutions (1.5625 ns), there is a time offset among TDCs. Timing calibration aims at aligning the TDCs in time. Timing calibration can be performed using an LED deployed at the center of the AD. As the LED flashes, a signal is sent to the FEE as a time reference. The time measured by the ith TDC (t_i) can be described as,

$$t_i = t_0 + t_{\text{tof}} + t_{i,\text{offset}} + t_{\text{time-walk}}(Q)$$

where t_0 is the time reference from the LED pulser, t_{tof} is the time of flight of the photon from the LED to the PMT, $t_{i,\text{offset}}$ is the time offset of the TDC channel, $t_{\text{time-walk}}(Q)$ is the apparent variation in arrival time due to different amount of charge, also known as time-walk effect. The time-walk effect is small relative to the the time offset, and is therefore ignored.

7.1.4 Determining the Nominal Charge

The charge collected in a trigger could come from hits that are not directly related to the physical event that causes the trigger. Since the electronics have rather consistent processing time, the time it takes from forming a trigger to reading out all channels is roughly constant. Hits that are associated to the actual triggering event tend to cluster in time. These hits can be selected by summing the charges of only those hits that lie in the region [-1650,-1250] ns. The charge sum is called "nominal charge", and this is the charge value that is used in subsequent analyses.

7.1.5 Quantum Efficiency

PMT quantum efficiency affects the overall detection efficiency of an AD. In particular, the energy resolution is affected by the variation in quantum efficiency among the PMTs in an AD. A large variation in quantum efficiency would result in a large variation in detector response to events occuring in different parts of the AD. This non-uniformity would worsen the AD energy resolution (More on energy resolution in Section 7.4). Therefore, instead of the actual value, we are more concerned about the relative quantum efficiency (RQE) of the PMTs in an AD. To understand the RQE, a study using the ^{68}Ge source has been performed [102]. The ^{68}Ge source was deployed at various Z positions. The number of ^{68}Ge detected at each PMTs divided by the average of all PMTs can be used to estimate the RQE. It was found that the RMS of the RQE distribution is about 4%.

7.2 Flasher Events

PMTs are known to spontaneously emit light through a mechanism which is not yet fully understood. These can trigger the AD and these events are called flasher events. Flasher events can have an

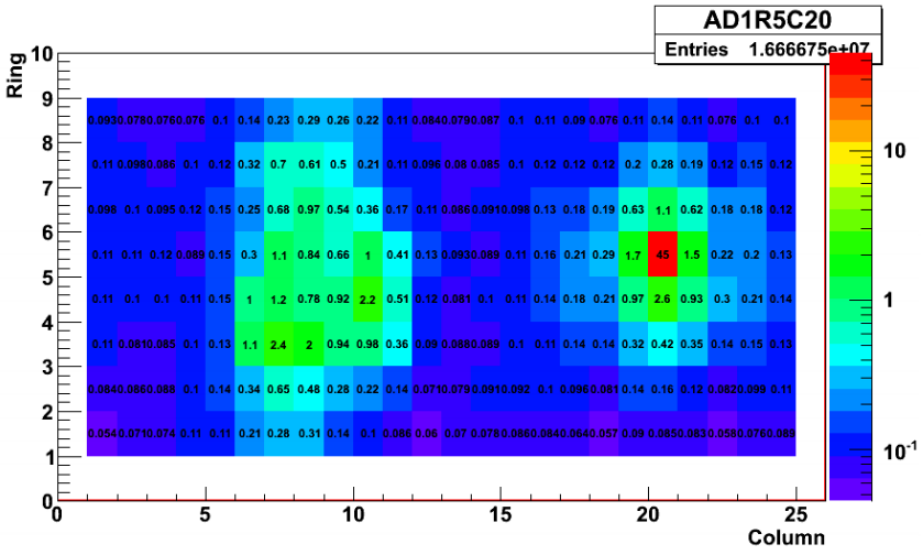

Figure 7.5: Flasher example. [25]

observed energy ranges from right at the trigger threshold to ∼100 MeV and comprises 5% of all triggers. Flasher events have characteristic charge patterns which means they can be easily removed with proper identification scheme.

7.2.1 Identification of Flasher Events

In a flasher event, the flashing PMT typically received the highest number of PEs among all PMTs in the AD, and this flash of light would be seen by the PMTs located on the opposite side of the AD. The PMTs can be divided into 4 static quadrants. Each quadrant consists of 6 columns of PMTs. The quadrant that contains the PMT which receives the highest charge (the potential flasher) is named quadrant 1, and going clockwise the rest of the quadrants are named 2, 3 and 4. Typically in a flasher event, quadrant 1 receives the highest charge, the quadrant 3 the next highest, and the remaining two the least. Using this observation, the charge-based flasher determinant (FID_Q) can be defined as follows:

$$FID_Q = log_{10}[(\frac{Q_3}{Q_2+Q_4})^2 + (\frac{MaxQ}{0.45})^2]$$

where Q_n is the charge receive in quadrant n, with n = 1,2,3 or 4; MaxQ is the charge received by the potential flasher. It is considered to be a flasher event if $FID_Q > 0$. This can be visualized as

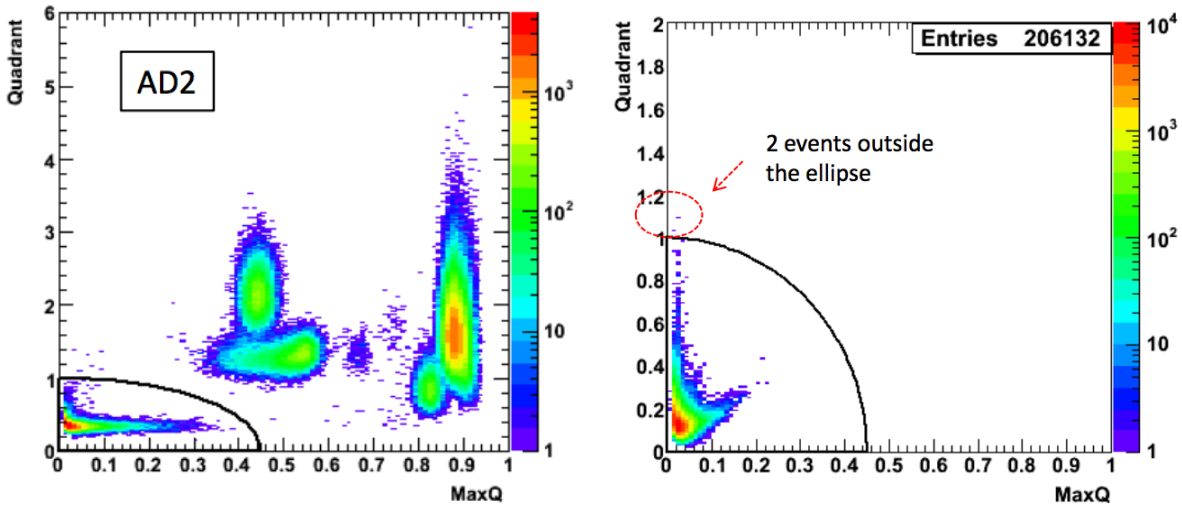

Figure 7.6: Left: $\frac{Q_3}{Q_2+Q_4}$ vs $MaxQ$ (FID_Q) in data (AD2 at Daya Bay near site). Right: Monte Carlo simulation. [26]

an ellipse on the $\frac{Q_3}{Q_2+Q_4}$-$MaxQ$ plane outside of which are all flasher events. For the 2" PMTs, we simply look at the charge: if it receives more than 100 PEs, it is considered as a flasher event.

Timing information can also be used which is ignored in the analysis in [103]. It can be seen that in flasher events, the timing distribution has a thicker tail at later times. Using this feature, another independent timing-based flasher determinant can be defined:

$$FID_T = log_{10}[4(1-t_{PSD})^2 + 1.8(1-t_{PSD1})^2]$$

where t_{PSD} and t_{PSD1} are the ratios of the integrals of timing distribution in [-1650,-1450] ns and [-1650,-1500] ns respectively to the integral over the full range. $FID_T > 0$ indicates a flasher event. Combining the two determinants above, an event is considered as flasher if any of the determinants is greater than one, i.e.

$$\text{Flasher condition: } FID_Q > 0 \text{ or } FID_T > 0$$

7.2.2 Misidentification

The flasher identification method can introduce uncertainties in two ways:

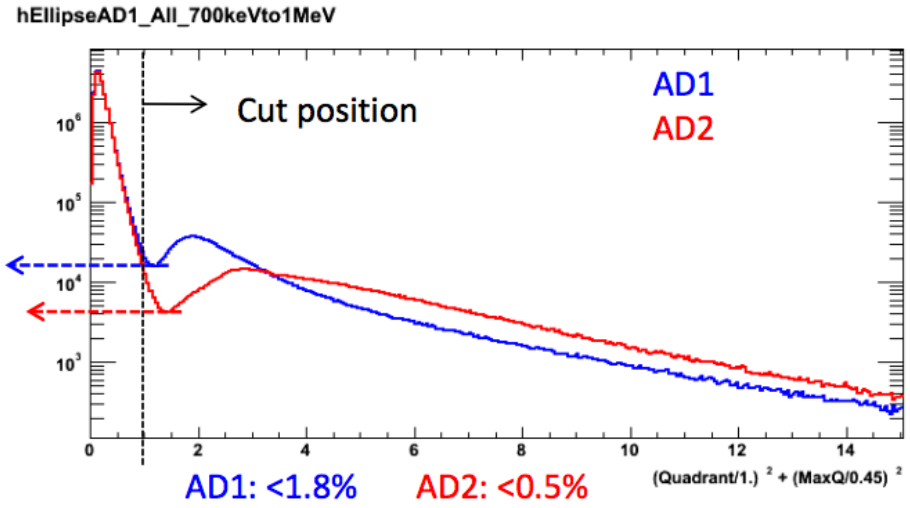

Figure 7.7: The blue and the red lines show the FID_Q distribution for AD1 and AD2, and the arrows indicate extrapolation. [26]

Normal events being misidentified as flasher events. In this case, IBD selection efficiency would be reduced. To estimate this, a Monte Carlo study has been performed [26, 28]. By applying the flasher cuts to simulated data, it was shown that the about 1×10^{-4} of the IBD events were misidentified as flashers.

Flasher events being misidentified as normal events. In this case, flasher events would contaminate the IBD sample. To understand this, we can extrapolate the FID_Q distribution to the region $FID_Q < 0$ with a horizontal line. Similar was done for FID_T. The fraction of flasher events that leaked into the signal region can be conservatively estimated to be about 1×10^{-4}.

7.3 Vertex Reconstruction

Vertex refers to the position in the AD where an event occurs. To reconstruct the vertex position, we make use of charge information. For a given event, the PMTs at different locations would receive different amounts of light. The vertex position can be deduced from this charge distribution. There are two ways to find the vertex position:

Center-of-charge A straightforward way is to use the observation that PMTs closer to the event would receive more charge than those further. The vertex position can be estimate with the average of the PMT coordinates weighted by the received charge.

Charge templates Another way to find the vertex position is to use charge templates [27]. Charge templates are charge distributions that are produced by events occurring at known positions. We can generate these charge templates using Monte Carlo simulation. By comparing the actual detected charge distribution with a set of charge templates, the vertex position can be reconstructed.

7.3.1 Vertex Reconstruction: Center-of-charge

The center-of-charge (COC) is defined as:

$$\overrightarrow{R_{coc}} = \frac{\sum_i^{PMTs} Q_i \overrightarrow{R_i}}{\sum_i^{PMTs} Q_i}$$

where $\overrightarrow{R_{coc}}$ is the COC; Q_i and $\overrightarrow{R_i}$ are respectively the charge received and the position of the ith PMT.

However, using the COC as the reconstructed vertex has a large bias. The COC tends to be closer to the center of the AD then the actual position of the event.

7.3.1.1 Improved Center-of-charge method

This can be corrected by "stretching" the COC to the appropriate position [104] using an empirical model. From the results of Monte Carlo simulations, the true vertex position appears to be a function of $\overrightarrow{R_{coc}}$ which can be modelled as:

$$r_{rec} = c_1 \times r_{coc} - c_2 \times r_{coc}^2$$

$$z_{rec} = (z_{coc} - c_3 \times z_{coc}^3) \times (c_4 - c_5 \times r_{coc})$$

where r_{rec} and z_{rec} are the r and z component of the corrected reconstructed vertex position; r_{coc} and z_{coc} are the r and z component of $\overrightarrow{R_{coc}}$; c_i are the parameters of the model. Using ^{60}Co source data, the parameters were determined to be:

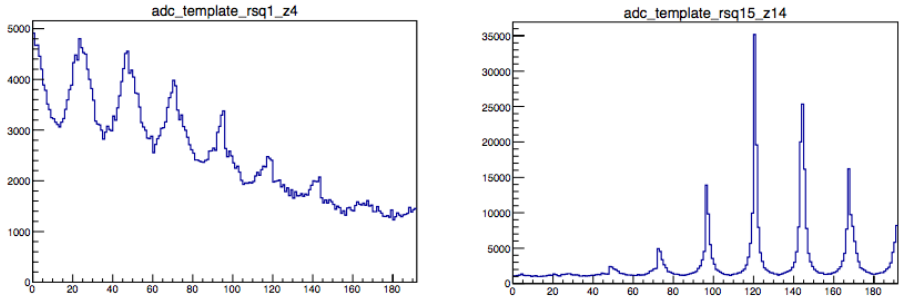

Figure 7.8: Examples of charge templates for vertex reconstruction. The left one is for 0.2 m^2 < r^2 < 0.4 m^2 and -1.2 m < z < -1.0 m, while the right one is for 3.0 m^2 < r^2 < 3.2 m^2 and 0.8 m < z < 1.0 m. [27]

$$c_1 = 1.82,\ c_2 = 1.95 \times 10^{-4}\ c_3 = 1.579 \times 10^{-7},\ c_4 = 3.128,\ c_5 = 9.64 \times 10^{-4}$$

7.3.2 Vertex reconstruction: charge templates

7.3.2.1 Creating charge templates

The region enclosed by the 4m OAV is divided into 20 × 20 × 24 bins in (r^2, z, ϕ) cylindrical coordinates. With the assumption of azimuthal symmetry, we have effectively 400 bins.

Positron events distributed uniformly over the OAV region were simulated. The charge template for each bin was obtained by averaging the charge distributions that were produced by the positron events in that bin.

7.3.2.2 Fitting and interpolation

The first estimate of the vertex position can be obtained by performing a chi-square minimization. Using the actual detected charge and the expected charge from the templates, the following chi-square can be formulated:

$$\chi^2 = 2 \sum_{i}^{PMTs} [N_i^{exp} - N_i^{obs} + N_i^{obs} ln(\frac{N_i^{obs}}{N_i^{exp}})]$$

where N_i^{obs} and N_i^{exp} are respectively the observed and the expected charge (in p.e.) of the ith PMT.

After the bin with minimum chi-square is found, the vertex position can be further refined using a parabolic interpolation. The chi-square values of the bins adjacent to the minimum bin are also

evaluated. In one of the two dimensions (r^2 or z), a parabola that joins the minimum point and the two adjacent points could be drawn. The minimum of the parabola can be analytically calculated. The process was repeated in the other dimension, giving a more accurate reconstruction of the vertex position. This vertex reconstruction is superior to the center-of-charge method and therefore is chosen in this analysis.

7.4 Energy reconstruction

In Section 7.1 on PMT calibration, we reconstructed the charge received by the PMT from the low level ADC and TDC values. Building upon the calibrated charge produced in PMT calibration, energy reconstuction (which is part of the so-called *AdSimple* reconstruction algorithm) aims to provide an estimate of the physical energy of the particle detected [105].

Since the AD is designed to work as a calorimeter, meaning that the particle is expected to deposit all of its energy into the AD. On the other hand, scintillators, the main detection material of the AD, have an approximately linear response. This means that the scintillation light produced would be roughly proportional to the energy of the particle. Therefore, we can scale the calibrated charge with a constant factor (called light yield), giving an estimate of the particle energy. This first approximation is called visible energy (E_{vis}).

The detector response is not only a function of particle energy, but also of vertex position. This non-uniformity of detector response can be corrected for using vertex information. This would give us a (hopefully) better estimate of the particle energy. This improved estimate is called reconstructed energy (E_{rec}).

The following paragraphs describe how the visible energy and the reconstructed were obtained.

7.4.1 Visible energy (E_{vis})

To determine the light yield, we need an anchor point. In principle, we can use any source with known energy and simply divide the detected charge by the particle energy to obtain the light yield. However, Gd-captured spallation neutron events are a natural choice for the following reason. One

of the main source of uncertainty is the energy cut for the delayed neutron signal of an IBD event (See Chapter 8 for details on signal selection). The spallation neutron events are essentially the same as the delayed neutron events. Although the thermalization process could slightly differ due to different neutron energy, what is observed at the AD is still the gamma rays from neutron capture. Moreover, like the delayed neutrons, spallation neutron are expected to distribute uniformly over the AD. This makes spallation neutrons a suitable choice for determining the light yield [106]. The Gd-captured spallation neutron events are selected in two steps: first select the muon event and then the neutron capture event. A trigger is tagged as a muon if,

- Nominal charge $>$ 4000 p.e.,
- Number of PMTs hit in IWS $>$ 10, or
- Number of PMTs hit in OWS $>$ 12.

The n-Gd events are selected by cutting on the time since the last muon (Δt), in the range (20 μs $< \Delta t <$ 200 μs), subtracted by the the background region in the range (2 ms $< \Delta t <$ 3 ms).

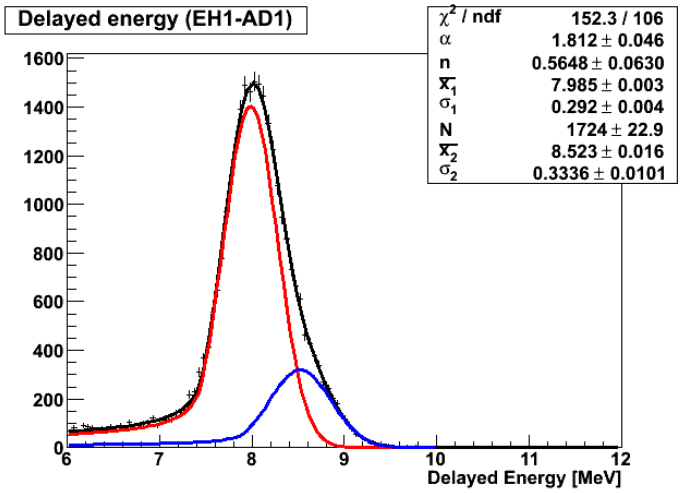

Figure 7.9: Gd neutron capture peak fitted with a sum of two crystal ball functions.

The peak is then fitted with a sum of two crystal ball functions, corresponding to the 8.54 MeV peak from ^{155}Gd and the 7.94 MeV peak from ^{157}Gd. The crystal ball function is defined as,

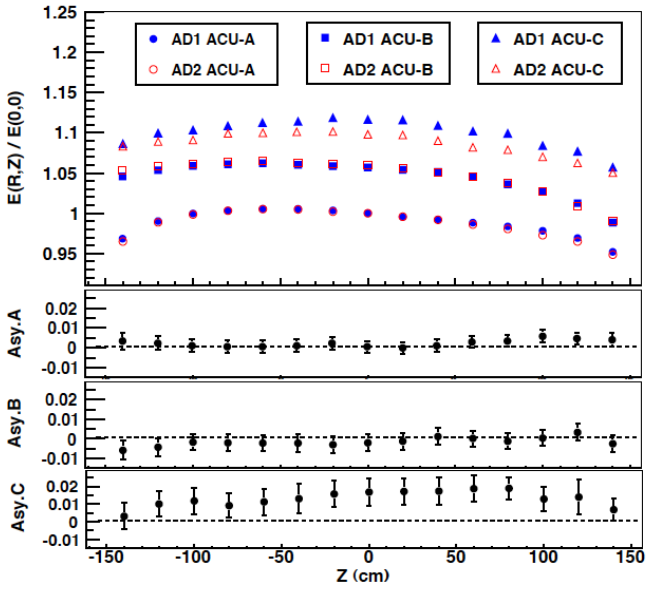

Figure 7.10: Energy response uniformity of AD1 and AD2 [28].

$$f(x;\alpha,n,\bar{x},\sigma) = \begin{cases} Ne^{-\frac{(x-\bar{x})^2}{2\sigma^2}} & \text{if } \frac{x-\bar{x}}{\sigma} > -\alpha \\ NA(B-\frac{x-\bar{x}}{\sigma})^{-n} & \text{otherwise} \end{cases}$$

where A $= (\frac{n}{|\alpha|})^n e^{-\frac{|\alpha|^2}{2}}$ and B $= \frac{n}{|\alpha|} - |\alpha|$. The light yield is calculated by requiring that the ^{157}Gd peak locates exactly at 7.94 MeV (i.e. the anchor point). The calculated light yield is about 170 pe/MeV.

7.4.2 Reconstructed energy (E_{rec})

To correct for the non-uniformity in detector response and to arrive at E_{rec}, we want to find a correction function ($f(r,z)$) such that,

$$E_{rec} = f(r,z)E_{vis}$$

where r, z are the r and z components of the vertex position (in meters). For simplicity, this correction function is assumed to be separable,

$$f(r,z) = f_r(r)f_z(z)$$

There are different ways to determine the correction function. Below are two ways: one uses the calibration source ^{60}Co, and the other uses spallation neutrons.

7.4.2.1 Uniformity correction: ^{60}Co source

The r and z components of the correction function are assumed to be respectively a linear function and a third degree polynomial [104]:

$$f_r(r) = 1 + c_r r$$
$$f_z(z) = c_{z0} + c_{z1} z + c_{z2} z^2 + c_{z3} z^3$$

The coefficients were determined empirically using ^{60}Co source data taken along the three caibration axes. They are found to be:

$$c_r = 3.3762 \times 10^{-8}, c_{z1} = 1.0005, c_{z2} = -1.002 \times 10^{-5},$$
$$c_{z3} = -1.894 \times 10^{-8}, c_{z4} = -1.758 \times 10^{-13}.$$

7.4.2.2 Uniformity correction: Charge template method with spallation neutrons

The r and z components of the correction function are assumed to be the reciprocals of third degree polynomials [105],

$$f_r(r) = \frac{8.05}{c_{r0} + c_{r1} r + c_{r2} r^2 + c_{r3} r^3}$$
$$f_z(z) = \frac{8.05}{c_{z0} + c_{z1} z + c_{z2} z^2 + c_{z3} z^3}$$

The coefficients were determined empirically using spallation neutrons data. They are found to be:

$$c_{r0} = 7.74687, c_{r1} = -0.129958, c_{r2} = -0.355034, c_{r3} = -0.0337578,$$
$$c_{z0} = 8.09949, c_{z1} = -0.11702, c_{z2} = -0.124515, c_{z3} = -0.0245703.$$

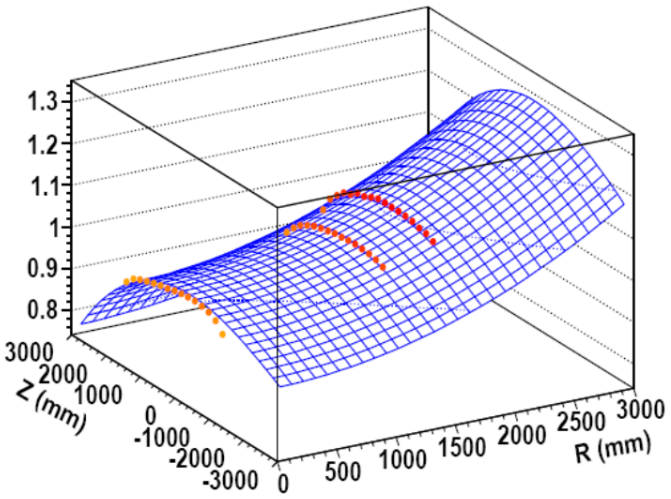

Figure 7.11: E_{rec} vs r and z. [29]

7.4.2.3 Comparison

The advantages and disadvantages of using ^{60}Co and spallation neutrons for uniformity correction are summarized below:

	^{60}Co	Spallation neutrons
Location	Precisely known ($\lesssim$ 5 mm)	Reconstructed
Statistics	High	Low
Availability	Require dedicated calibration runs	Extracted from physics runs
Identicality across ADs	Good	Depends mainly on overburden
Uniformity over AD	Only on the 3 calibration axes	Uniform

A direct comparison shows that the reconstructed energy produced by the above two methods are in fact consistent with each other. The method using spallation neutron was chosen since, arguably, it is slightly better because of the uniformity of spallation neutron events. This would give a more accurate estimate of the energy of the IBD neutron.

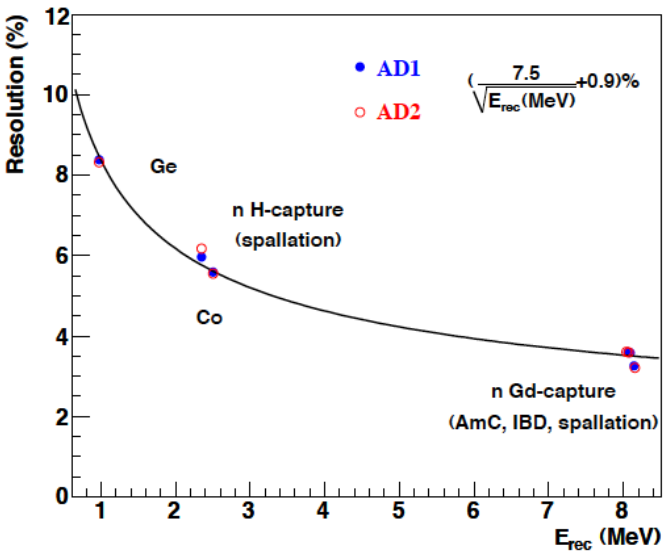

Figure 7.12: Energy resolution fit [28].

7.4.3 Energy Resolution

Energy resolution refers to the uncertainty in determining the energy of the event. This is mainly due to the Poisson error in counting the number of photoelectrons, which is proportional to $\sqrt{E}$. The energy resolution can be modeled as:

$$\frac{\sigma}{E} = \sigma_0 + \frac{\sigma_1}{\sqrt{E(MeV)}}$$

By fitting this model to calibration data, it is shown that $\sigma_0 = 0.9\%, \sigma_1 = 7.5\%$

Chapter 8

Signal selection

Now, having developed event reconstruction, we can make use of the reconstructed information to select IBD events. To devise a set of selection rules or cuts, there are three important considerations:

Selection efficiency Selection efficiency refers to the fraction of true IBD events being selected by the cuts. A large selection efficiency is favorable, because it reduces statistical uncertainty.

Background contamination An efficient cut sometimes comes together with a high background contamination, meaning that non-IBD events could be mistaken as IBDs. Obviously, we need to minimize background contamination.

Uncertainties After arriving at a set of cuts, we need to estimate the selection efficiency and background contamination. Equally importantly, their uncertainties.

In the following sections, the IBD selection cuts are described. Their efficiencies and the associated uncertainties are estimated. The discussions in this and the next two chapters largely follow those in [107].

8.1 IBD Selection

The IBD events can be selected with the following cuts,

- Prompt energy cut: 0.7 MeV $< E_p <$ 12 MeV. (See Section 8.1.1)
- Delayed energy cut: 6 MeV $< E_d <$ 12 MeV. (See Section 8.1.1)

- Time correlation cut: 1 μs $< \Delta$t $<$ 200 μs (See Section 8.1.2)
- Flasher cut: Both the prompt and the delayed candidate are not tagged as flashers. (See Section 7.2)
- Muon cut (See Section 8.1.3)
- Multiplicity cut (See Section 8.1.5)

where E_p and E_d are respectively the reconstructed energy of the prompt and the delayed candidate and Δt is the time separation between them.

8.1.1 Energy Cuts

8.1.1.1 Prompt Energy Cut

As seen in the expected prompt energy spectrum, it is not difficult to see that the energy cut 0.7 MeV $< E_p <$ 12 MeV would capture most of the prompt hits. It only has a small effect on efficiency. From Monte Carlo simulation, the efficiency of such a cut is $99.90\% \pm 0.10\%$.

8.1.1.2 Non-ideal IBD Events

Before estimating the selection efficiency, we need to understand a bit more about how the delayed signal is detected. In "ideal" IBD event, the $\bar{\nu_e}$ is captured by a proton in the target volume, and the delayed neutron is captured by Gd in the target volume. Consider the following deviations from this ideal event:

Name	Prompt event location	Neutron capture location	Neutron capture target
Ideal case	Target volume	Target volume	Gd
Gd capture ratio	Target volume	Target volume	^1H or some other isotope
Spill-out	Target volume	Outside of target volume	^1H or some other isotope
Spill-in	Outside of target volume	Target volume	Gd

Gd capture ratio A neutron in the target volume can be captured by some isotope other than Gd, for example, by ^1H, which has a relatively large neutron capture cross-section. The neutrons captured by ^1H gives out a gamma ray of only 2.2 MeV, evading the delayed energy window [6,12] MeV.

Spill-out The neutron can drift away from the target volume, avoiding capture by Gd. The spill-out effect can be evaluated together with the Gd capture ratio effect, since both of them result in missing Gd capture signal.

Spill-in The neutron from an IBD event happening outside of the target volume can drift into the target volume and be detected. This would increase the efficiency in selecting the delayed event, since the apparent target volume becomes larger.

The impacts of the above effects on the detection efficiency can be evaluated using Monte Carlo simulation. The efficiency due to selecting only Gd capture events and the spill-out effect is found to be $83.8\% \pm 0.8\%$ and the spill-in effect causes an enhancement of $5.0\% \pm 1.5\%$.

8.1.1.3 Delayed Energy Cut

After correcting for the factors in the previous section, we are left with the "ideal" events. However, inefficiencies still exists. Some of the gamma rays from the neutron capture by Gd can escape the target volume and the gamma catcher, so that the total detected energy fall below the delayed energy window [6,12] MeV. The finite energy resolution of the AD would also affect the delayed energy cut efficiency. The delayed energy cut efficiency can be estimated by modeling the Gd capture peaks by a sum of two crystal ball functions (See Section 7.4.1). By comparing the delayed spectrum in data and in MC aftering, the efficiency of the delyed energy cut was estimated to be $92.24\% \pm 0.51\%$. The absolute uncertainty of 0.51% was estimated based on the difference in efficency before and after MC tuning, while the uncorrelated uncertainty among detectors has two components: one due to the energy scale uncertainty and the other due to the uncertainty in the low energy tail shape. The energy scale unceratinty at 6 MeV is estimated to be 0.7% which translates into 0.18% uncertainty

in delayed energy cut. The variation among detectors in the relative size of the low energy tail can be interpreted as the tail shape uncertainty and was estimated to be 0.19%. Coombining the two gives a total uncorrelated uncertainty of 0.26%.

8.1.2 Time Correlation Cut

Before being captured, the delayed neutron from IBD would undergo thermalization: the neutron elastically scatters mainly on hydrogen and slows down to thermal energies. The neutron capture cross-section increases as the neutron energy decreases. This means, as the neutron thermalizes, the probability of neutron capture increase over time. Once the neutron is around thermal energy, the cross-section of neutron capture by Gd roughly stays constant. The probability of neutron capture then decreases over time as less and less neutrons remain. The time distribution of neutron capture can be modelled as:

$$N(t) = -N_0 e^{-\frac{t}{t_0}} + N_1 e^{-\frac{t}{t_1}} + N_{bg}$$

where the three terms denote respectively thermalization stage, drifting stage and a constant accidental background. The observed time distribution can be fitted to the model to find the neutron capture time t_1, which is found to lie in the range from 25.0 μs to 28.5 μs in different ADs, which is a 0.5% variation. (A 1 μs cut is included to reduce electronics effects.) This variation in neutron capture time among ADs can be attributed to the fluctuation in Gd capture ratio among ADs and this translates to a 0.1% relative uncertainty in Gd capture ratio.

By comparing data with MC, the efficiency of the time correlation cut can then be estimated to be $98.6\% \pm 0.19\%$.

8.1.3 Muon Cut

Muons are known to produce spallation neutrons, long-lived isotopes such as ^{9}Li/^{8}He, which can cause severe background. We can identify muons with the AD and the water shields.

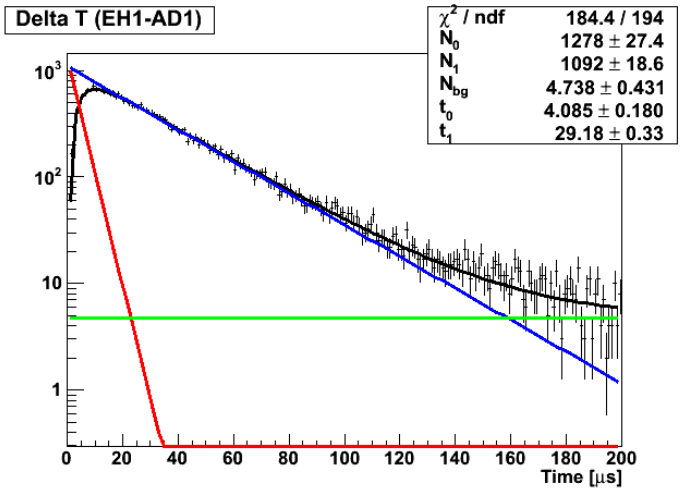

Figure 8.1: A fit of the time between prompt and delayed event. The red line is the negative of the thermalization component, the blue line is the drifting component and the green line is the background.

Muons Muons are characterized by large energy deposition along its track. They are readily identified by the high energy observed in the AD and the water shields. This large amount of energy causes spurious triggers. Its effects can be reduced by vetoing the AD for several microseconds.

Spallation neutrons A spallation neutron and an IBD neutron are practically indistinguishable. Since neutron capture time in the target region is about 30 μs, a sufficiently long muon veto can reject a large fraction of these spallation neutron.

^{9}Li/^{8}He ^{9}Li/^{8}He beta decays with a half-life of 178.3 ms/119.1 ms and a Q-value of 13.6 MeV/10.7 MeV, into ^{9}Be/^{8}Li, which can emit a neutron. Because of their relatively long half-lives, we need a muon veto of at least hundreds of milliseconds long. This would significantly reduce the efficiency of the muon cut. Fortunately, since ^{9}Li/^{8}He are mostly produced by muons which deposit more-than-average energy to the AD, we could apply this long muon veto only to "brighter" muons identified by the AD. These are called shower muons. Three types of muons can be defined as follows:

- WS Muon: IWS PMTs Hit $>$ 12 or OWS PMTs Hit $>$ 12
- AD Muon: Total charge in AD $>$ 3000 PEs but less than 3 $\times 10^5$ PEs
- Shower Muon: Total charge in AD $>$ 3 $\times 10^5$ PEs

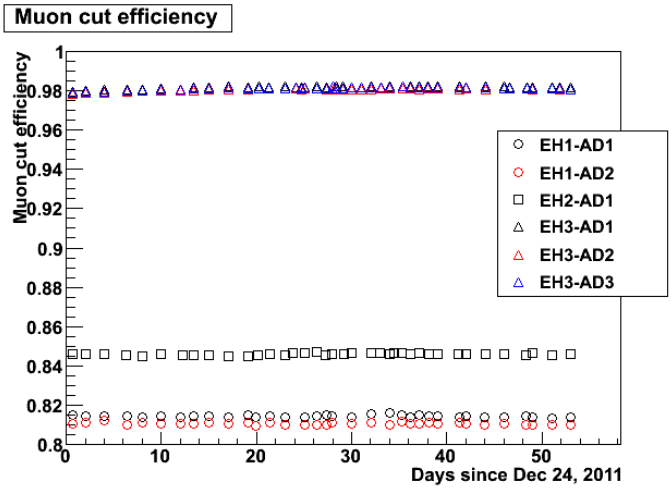

Figure 8.2: Muon cut efficiency over time.

For each type of muons, the following cuts can be applied:

- WS Muon: 200 μs following muon hit.
- AD Muon: 1 ms following muon hit.
- Shower Muon: 0.4 s following muon hit.

(These cuts are applied to the delayed signal only. This is to decouple muon cut efficiency with neutron capture time.) However, some modifications to these cuts are needed. Due to the time misalignments between the detectors, a $2\mu s$ veto before a muon is needed. In addition, as we will see in Section 8.1.5, an additional $400\mu s$ veto after a muon is required to decouple muon cut efficiency from multiplicity cut efficiency. The final muon cuts are then modified to be:

- WS Muon: [-2 μs, 600 μs] relative to muon hit.
- AD Muon: [-2 μs, 1.4 ms] relative to muon hit.
- Shower Muon: [-2 μs, 0.4 s] relative to muon hit.

(Notice that the veto times differ from the analysis in [103].) The muon cut efficiency can be estimate by simply adding up the total veto time.

8.1.4 Flasher Cut

Flashers are identified using the FID metric discussed in Section 7.2. Both the prompt and the delayed signal are required to be a non-flasher. The efficiency is estimated to be 99.93% [108].

8.1.5 Multiplicity Cut

The signature of an IBD event consists of exactly one prompt positron and one delayed neutron. Sometimes, a cluster of three or more events are identified as possible candidates of a prompt-delayed pair. A simple way is to discard all such multiplets. However, the efficiency of such a selection rule would be diffuclt to estimate, because it would depend on the neutron capture time and the antineutrino energy. To eliminate this problem, we can remove extra prompt or delayed candidates that fall winthin fixed time windows relative to the delayed candidate. (Notice that this method differs from the analysis in [103].) More concretely, the selection rule can be described as follows: (Times are relative to the delayed candidate)

- Only one prompt candidate in [-200 μs, 0]
- No prompt candidate in [-400 μs, -200 μs]
- No delayed candidate in [0, 200 μs]

This way, the efficiency can be easily evaluated by using Poisson distribution. If we write the Poisson distribution as $P(k;\lambda) = \frac{\lambda^k e^{-\lambda}}{k!}$, then the efficiency of this selection rule can be calculated to be:

$$P(0; 400\mu s \times R_p) P(0; 200\mu s \times R_d)$$

where R_p and R_d are the singles rates of prompt-like and delayed-like events.

8.1.6 Summary

	DYB AD1	DYB AD2	LA AD1	Far AD1	Far AD2	Far AD3
DAQ Live time [days]	49.5527	49.5527	49.4968	48.9453	48.9453	48.9453
$\bar{\nu_e}$ candidate [events]	28692	28857	22169	3536	3464	3461

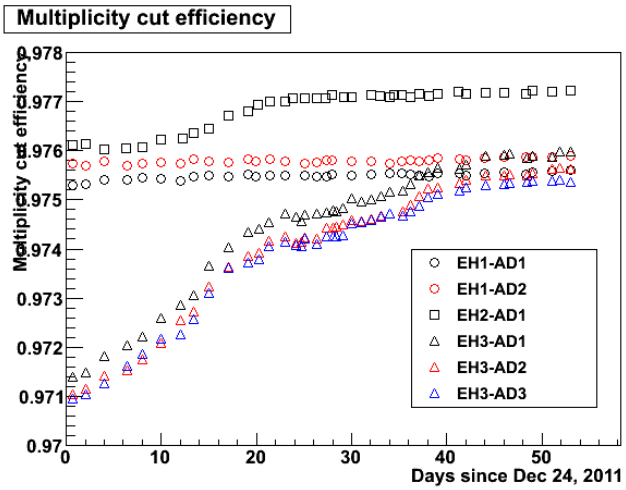

Figure 8.3: Multiplicity cut efficiency over time.

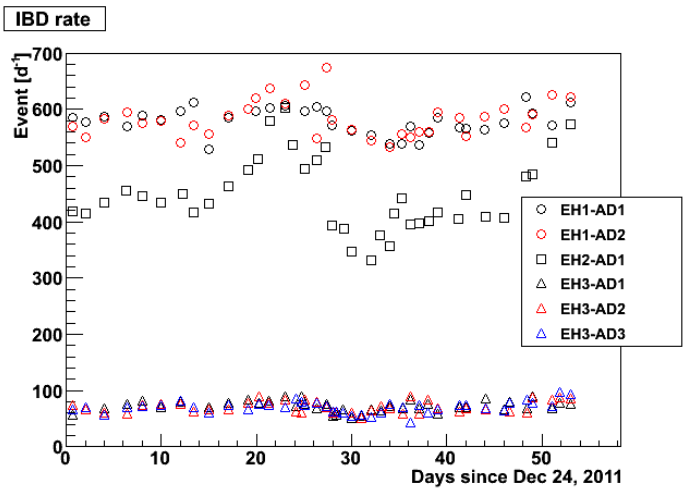

Figure 8.4: IBD candidate over time.

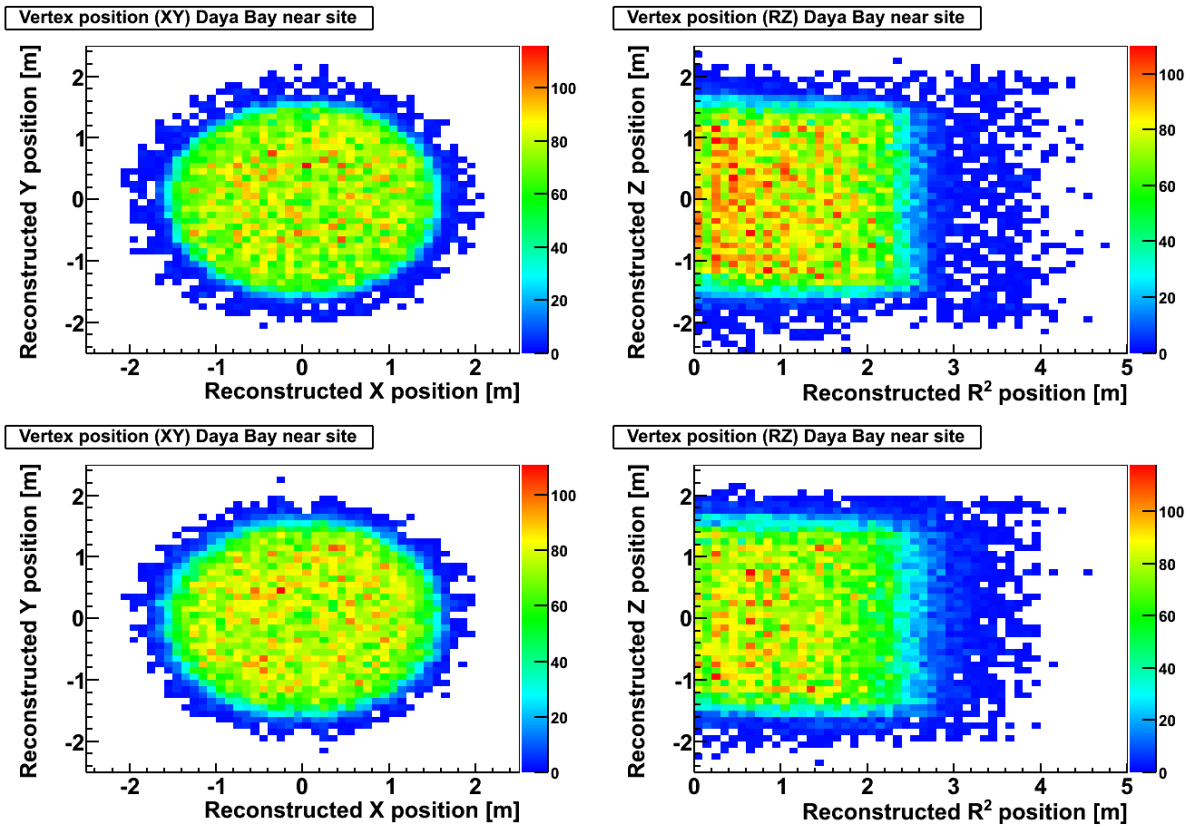

Figure 8.5: Reconstructed vertex position for the IBD candidates at the Daya Bay near site. (First row) prompt signal, (Second row) delayed signal.

Below is a summary of the cut efficiencies.

Cut	Efficiency	Correlated Uncertainty	Uncorrelated Uncertainty
Prompt energy cut	0.9990	0.10%	0.01%
Gd capture ratio	0.8383	0.60%	0.10%
Spill-in	1.0503	0.10%	0.02%
Delayed energy cut	0.9224	0.51%	0.26%
Time correlation cut	0.9857	0.19%	0.02%
Flasher cut	0.9991	0.02%	0.01%
Total	0.7990	0.94%	0.28%

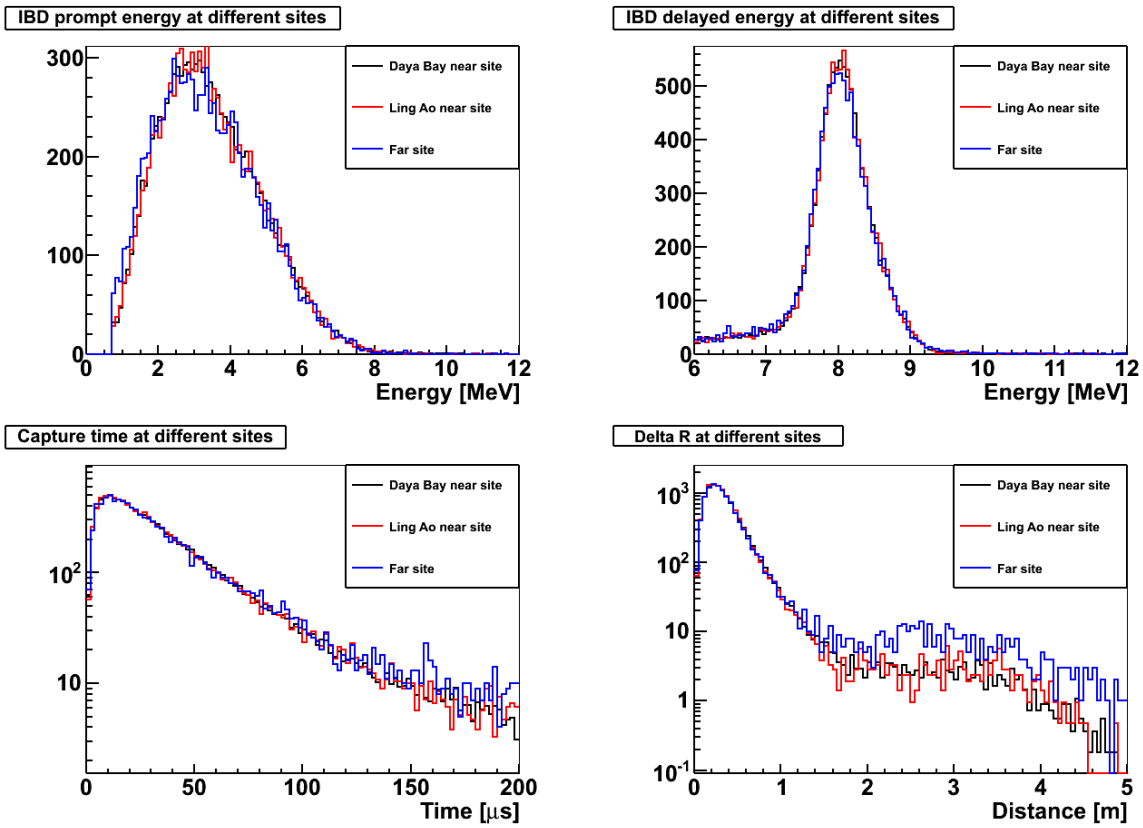

Figure 8.6: Comparison among all three sites. Plots for the near sites are normalized to the one for far site.

Chapter 9

Backgrounds

As discussed earlier in Section 2.4, various sources of background can affect θ_{13} measurement. Residual backgrounds will inevitably be included in the selected antineutrino sample. Therefore, we need to estimate their rates in the selection region. This chapter is devoted to estimating the residual background leaking into the antineutrino sample selected according to the rules in Chapter 8.

9.1 Accidental Background

Uncorrelated events can sometimes accidentally coincide in such a way that the pair passes all the selection cuts, and end up being wrongly considered as an antineutrino candidate. Of course, we cannot individually identify such misidentified pairs. However, we can statistically subtract the the fraction of accidentals from the set of antineutrino candidates. More concretely, an accidental would be included as an antineutrino candidate when the followings are satisfied:

- A delayed-like event happens in the time window [1μs, 200 μs] after a prompt-like event.
- No prompt-like events happen in the time window [200 μs, 400 μs] before the delayed-like event.
- No delayed-like events happen within 200 μs after the delayed-like event.
- The events are uncorrelated events. (Pure singles events)
- The events survive the flasher cut and the muon cut.

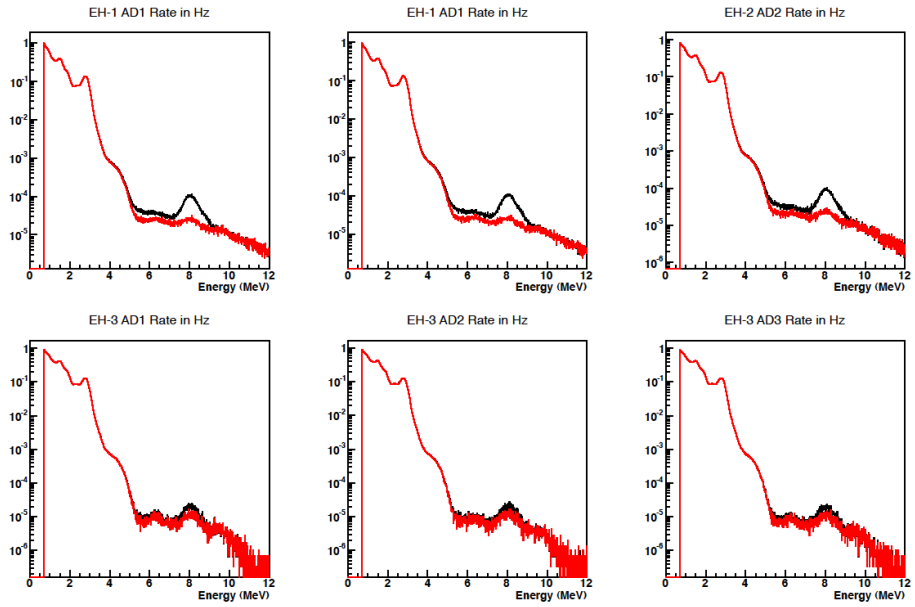

Figure 9.1: The black line shows the singles rates after muon cut and flasher cut, while the red line shows the pure singles rate in which correlated hits are also removed, in addition to muon cut and flasher cut.

The rates of the events satifying the first three conditions can be easily calculated with probabilities once we obtain the set of pure singles events. This can be found by applying the same selection rules as antineutrino events, but with time cut and multiplicity cut modifed as follows:

- No prompt-like events within the previous 400 μs.
- No delayed-like events within the following 200 μs.

These are essentailly logical complements to the original time cut and multiplicity cut. Now we obtain pure singles

The accidental rates can then be calculated as,

$$R_{acc} = P(1; 199\mu s R_p)P(0; 200\mu s R_p)P(0; 200\mu s R_d)R_d$$

It turn out that R_{acc} is about 10 per day at the near sites, 4 per day at the far site.

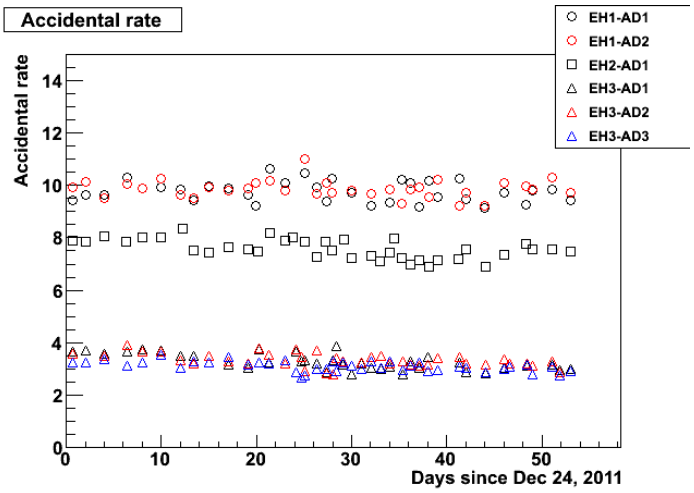

Figure 9.2: Accidental rates over time.

9.2 Cosmogenic Background

9.2.1 ^{9}Li/^{8}He

The electron emitted by the beta emitters ^{9}Li/^{8}He can be mistaken as an IBD prompt signal. ^{9}Li/^{8}He can beta-decay into some excited states of ^{9}Be/^{8}Li with branching ratios of (50.8±0.9)%/(16± 1)% [109]. These excited states are at energy levels higher than the neutron binding energy of the respective nucleus (^{9}Be: 1.67 MeV, ^{8}Li: 2.03 MeV), making neutron emission energetically favorable. The prompt beta and the delayed neutron can be mistaken as an IBD event. Given that the half-lives of ^{9}Li/^{8}He are 119.1 ms/178.3 ms, the shower muon cut of 0.4 s should have rejected most of these backgrounds. The remaining background which leaks into the IBD sample can be estimated by modeling the distribution of the time since the preceding muon [110].

We can first derive the probability $P_i(t)$ of observing a spallation product i (e.g. ^{9}Li/^{8}He) after a duration of t following a muon event. Suppose λ_μ is the muon rate, λ_i is the lifetime of the spallation product. Also, define $t = 0$ to be the time at which the spallation product is observed. Now, we can consider two cases:

Case 1: The preceding muon produced the spallation product. In this case, $P_i(t)$ can be written as,

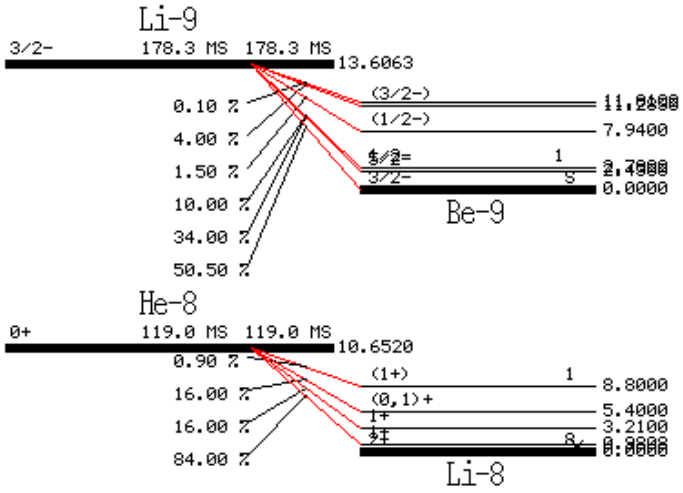

Figure 9.3: Decay schemes for ^{9}Li and ^{8}He [30].

$$dP_i(t) = \text{P(Observing } i \text{ in the interval } [0, dt]) \times \text{P(Not observing } i \text{ in the interval } [-t, 0])$$
$$\times \text{P(Not observing any muons in the interval } [-t, 0])$$

Recall that the Poisson distribution can be written as $f(k;\lambda) = \frac{\lambda^k e^{-\lambda}}{k!}$,

$$\begin{aligned} dP_i(t) &= f(1;\lambda_i dt) \times f(0;\lambda_i t) \times f(0;\lambda_\mu t) \\ &= \lambda_i dt e^{-\lambda_i dt} \times e^{-\lambda_i t} \times e^{-\lambda_\mu t} \\ &\approx \lambda_i e^{-(\lambda_i + \lambda_\mu)t} dt \end{aligned}$$

Case 2: The preceding muon did not produce the spallation product. In this case, the mother muon is not the preceding muon, but is actually located further back in time, say $-t'$. That means, $-t'$ can be anywhere between $-\infty$ and $-t$. The probability then becomes,

$$dP_i(t) = \int_{-\infty}^{-t} [\text{P(Observing } i \text{ in the interval } [-t', -t' + dt']) \times \text{P(Not observing } i \text{ in the interval}$$
$$[-t', 0])]\text{dt' } \times \text{P(Observing a muon in the interval } [-t, -t + dt]) \times \text{P(Not observing other muons in}$$
$$\text{the interval } [-t, 0])$$

Therefore,

$$\begin{aligned} dP_i(t) &= [\int_t^\infty f(1;\lambda_i dt')f(0;\lambda_i t')] \times f(1;\lambda_\mu dt) \times f(0;\lambda_\mu t) \\ &\approx \int_t^\infty e^{\lambda_i t'}\lambda_i dt' \times \lambda_\mu dt \times e^{-\lambda_\mu t} \\ &= \lambda_\mu e^{-(\lambda_i+\lambda_\mu)t} dt \end{aligned}$$

Combining the two cases,

$$dP_i(t) = (\lambda_\mu + \lambda_i)e^{-(\lambda_i+\lambda_\mu)t}dt$$

Apart from spallation products, there can also be some other background b that is uncorrelated with muons. Using similar arguments, we can derive the probability $P_b(t)$ corresponding to this background,

$$dP_b(t) = \lambda_\mu e^{-\lambda_\mu t}dt$$

Therefore, the total probability can be written as,

$$\begin{aligned} \frac{dP}{dt} &= \sum_i^n N_i \frac{dP_i}{dt} + N_b \frac{dP_b}{dt} \\ &= \sum_i^n N_i(\lambda_\mu + \lambda_i)e^{-(\lambda_i+\lambda_\mu)t} + N_b\lambda_\mu e^{-\lambda_\mu t} \\ &\approx \sum_i^n N_i\lambda_i e^{-\lambda_i t} + N_b\lambda_\mu e^{-\lambda_\mu t} \qquad (\because \lambda_\mu \ll \lambda_i) \end{aligned}$$

Now we can invert the shower muon cut to obtain the ^{9}Li/^{8}He background, which means that we look for IBD candidates within the shower muon veto. However, apart from shower muons, muons that deposit less energy in the AD can also produce ^{9}Li/^{8}He. To estimate that, the muons are divided into three energy bins: $E_\mu > 1.75\ GeV$ (shower muons), $0.5\ GeV < E_\mu < 1.75 GeV$ and $E_\mu < 0.5\ GeV$. Then, the muons are further divided into two categories:

- Muons with detected neutrons ($n-\mu$): Muons which have Gd capture neutron like events in the following [20,200]μs window after the muons.

- Muons without detected neutrons (non $n-\mu$): Muons which do not have Gd capture neutron like events in the following [20,200]μs window after the muons.

For the shower muons in each site, the number of ^{9}Li/^{8}He produced by $n-\mu$ as a fraction of the total number of ^{9}Li/^{8}He produced by both categories of muons was calculated. This fraction was assumed to be constant over all E_μ, and was used to estimate the ^{9}Li/^{8}He production by lower energy muons. After considering the muon cuts, the remaining ^{9}Li/^{8}He per AD at each site was determined to be: 2.74 ± 0.64 d^{-1} at EH1, 1.45 ± 0.89 d^{-1} at EH2 and 0.16 ± 0.08 d^{-1} at EH3.

9.2.2 Fast Neutrons

Fast neutrons can mimic a positron prompt signal, when it causes proton recoil which has an energy similar to a prompt signal. Depending on the neutron energy, the energy deposited by the recoiled proton varies and can reach tens of MeV, while the prompt energy spectrum from true IBD events hardly extends to energy higher than 8.5 MeV. Therefore, IBD candidates with high prompt energy ($\gtrsim$ 10 MeV) contain mostly proton recoils. We can then extrapolate the proton recoil spectrum to the prompt energy region.

There are two approaches to estimating the proton recoil spectrum in the high energy region [111]. First, we can raise the muon threshold and look for IBD candidates with high prompt energy. It can be seen that the prompt energy is roughly constant at high energy. Another way is to look at IBD candidates which are coincident with muons (i.e. a triple coincidence: muon, prompt, delayed). Muons can be tagged by IWS or RPC. Either way, we see a flat prompt energy spectrum. The background in the [0.7,12] MeV range can then be estimated by simply extrapolating the flat spectrum. The fast neutron background per AD at each site was determined to be: 0.95 ± 0.28 d^{-1} at EH1, 0.71 ± 0.22 d^{-1} at EH2 and 0.07 ± 0.02 d^{-1} at EH3.

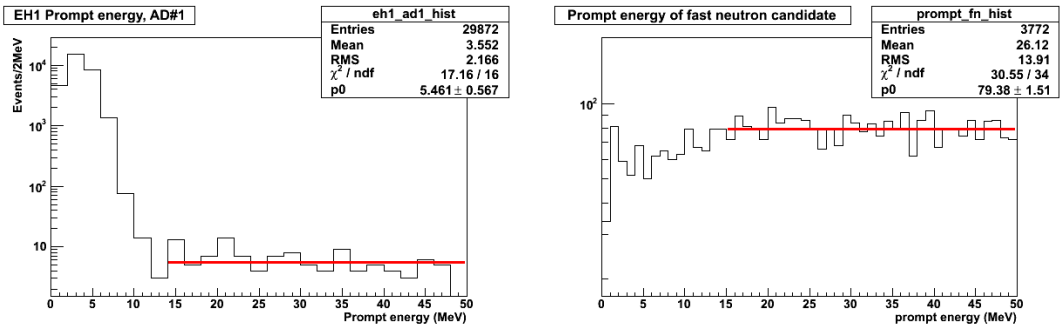

Figure 9.4: The energy spectrum of the fast neutron candidates identified using (left) AD and (right) water pool.

9.3 Calibration Source: ^{241}Am^{13}C

Although the neutron source ^{241}Am^{13}C is designed to emit no correlated gamma, the neutron itself can also produce correlated background by interacting with stainless steel. One possible scenario is: a neutron first inelastically scatter on ^{56}Fe giving a high energy gamma as ^{56}Fe de-excites, and then be captured by ^{57}Fe, giving another high energy gamma. A Monte Carlo study is performed to estimate this correlated background [31]. Comparing with the uncorrelated background as measured from data, the correlated background from ^{241}Am^{13}C can be determined to be $0.2 \pm 0.2\ d^{-1}$ for each AD [112].

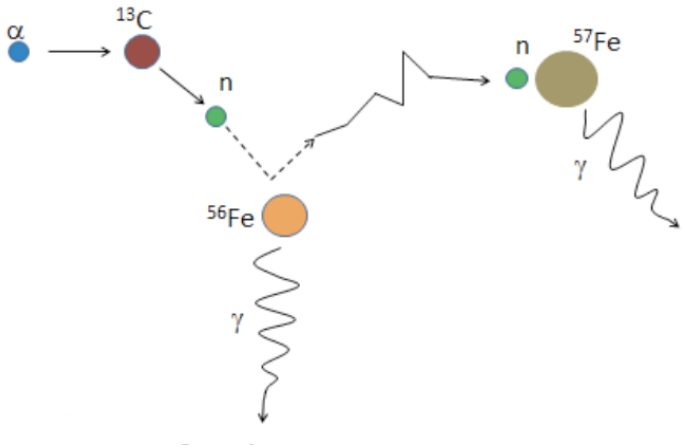

Figure 9.5: A possible scenario of ^{241}Am^{13}C causing correlated background [31].

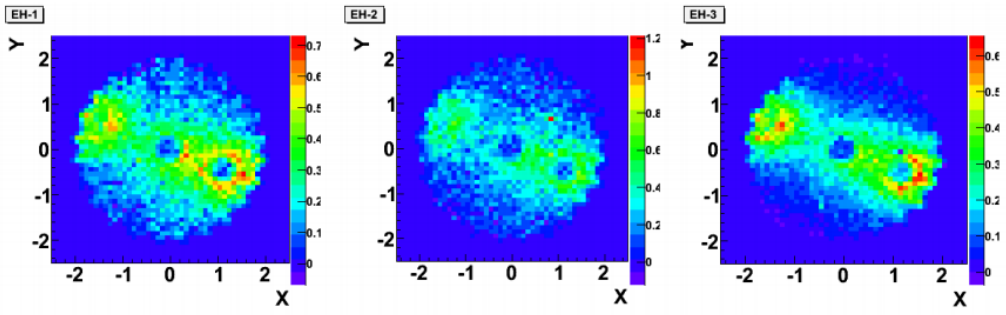

Figure 9.6: Background caused by ^{241}Am^{13}C [32].

9.4 ^{13}C(α,n)^{16}O

Natural radioactive isotopes, which emit α particles, are present in the detector. Most of them are part of the ^{238}U or the ^{232}Th chain. These α particles can trigger (α,n) reaction. One of them is ^{13}C(α,n)^{16}O. There are several mechanisms which can produce correlated background:

Mechanism	^{16}O state	Prompt	Delayed
1	Ground	Neutron elastically scattering on proton causing proton recoil	Neutron capture on Gd
2	Ground	Neutron inelastically scattering on γ ^{12} C giving 4.4 MeV	Neutron capture on Gd
3	1st excited	^{16}O de-excites to ground state giving 6.049 MeV e^-e^+ pair	Neutron capture on Gd
4	2nd excited	^{16}O de-excites to ground state giving a 6.129 MeV γ	Neutron capture on Gd

The α rate is measured from data. With the knowledge of the (α,n) cross-section, the background rate can be estimted. The ^{13}C(α,n)^{16}O background rate per AD in each site was measured to be: 0.04 ± 0.02 d^{-1} at EH1, 0.035 ± 0.02 d^{-1} at EH2 and 0.03 ± 0.02 d^{-1} at EH3 [113].

9.5 Summary

Below is a summary of all backgrounds.

	DYB AD1	DYB AD2	LA AD1	Far AD1	Far AD2	Far AD3
DAQ Live time [days]	49.5527	49.5527	49.4968	48.9453	48.9453	48.9453
$\bar{\nu_e}$ candidate [events]	28692	28857	22169	3536	3464	3461
Accidentals [events]	393.6	396.4	317.4	157.7	160.3	150.1
^{9}Li/^{8}He [events]	107.9	107.4	59.3	7.5	7.5	7.5
Fast Neutron [events]	37.4	37.2	29.0	3.3	3.3	3.3
Correlated ^{241}Am^{13}C [events]	7.9	7.8	8.2	9.4	9.4	9.4
^{13}C(α,n)^{16}O [events]	1.6	1.6	1.4	1.4	1.4	1.4
Total Expected Bkg [events]	548.3	550.5	415.4	179.2	181.8	171.6
Background Uncertainty [events]	28.3	28.2	38.2	10.3	10.2	10.2

Chapter 10

θ_{13} Analysis

Now we can proceed to determine θ_{13}. In Chapter 3, we estimated the expected antineutrino spectrum from the reactor[1]; and in Chapter 4, we estimated the number of target proton in the AD. Together with the selection cuts developed in Chapter 8 and the background estimation in Chapter 9, we can calculate the expected number of antineutrinos detected by the ADs. Finally, using a likelihood model with pull terms, we can deduce the value of θ_{13}.

10.1 Signal Estimation

The expected antineutrino flux $S_{jk}(E_\nu)$ at the detector j due to reactor core k can be estimated as,

$$S_{jk}(E_\nu) = T_j \epsilon_j \sigma(E_\nu) \frac{P_{ee}(E_\nu, L_{jk})}{4\pi L_{jk}^2} S_k(E_\nu)$$

where T_j is the number of target protons in detector j; ϵ_j is the efficiency of detector j; $\sigma(E_\nu)$ is the IBD cross-section; L_{jk} is the distance between detector j and reactor core k; $P_{ee}(E_\nu, L_{jk})$ is the survival probability of $\bar{\nu_e}$; $S_k(E_\nu)$ is the antineutrino flux from the reactor core k.

The survival probability P_{ee} can be written as,

$$P_{ee} = 1 - cos^2\theta_{12} sin^2 2\theta_{13} sin^2\Delta_{31} - sin^2\theta_{12} sin^2 2\theta_{13} sin^2\Delta_{32} - cos^4\theta_{13} sin^2 2\theta_{12} sin^2\Delta_{21}$$

where $\Delta_{ij} \equiv 1.267 \times 10^3 \delta m_{ij}^2 (eV^2) \frac{L(km)}{E(MeV)}$. With the approximation $\delta m_{31}^2 \approx \delta m_{32}^2$,

$$P_{ee} = 1 - sin^2 2\theta_{13} sin^2\Delta_{31} - cos^4\theta_{13} sin^2 2\theta_{12} sin^2\Delta_{21}$$

[1]Reactor power provided by Xin Qian in the form of weekly averages.

To perform a rate-only analysis, we are interested the total expected detection rate of $\bar{\nu_e}$,

$$\begin{aligned} R_{jk} &= \int S_{jk}(E_\nu) dE_\nu \\ &= \frac{T_j \epsilon_j}{4\pi L_{jk}^2} \int P_{ee}(E_\nu, L_{jk}) \sigma(E_\nu) S_k(E_\nu) dE_\nu \\ &= T_j \epsilon_j \bar{F}_k \frac{\bar{P}_{ee,jk}}{4\pi L_{jk}^2} \end{aligned}$$

where $\bar{F}_k \equiv \int \sigma(E_\nu) S_k(E_\nu) dE_\nu$ and $\bar{P}_{ee,jk} \equiv \frac{1}{\bar{F}_k} \int P_{ee}(E_\nu, L_{jk}) \sigma(E_\nu) S_k(E_\nu)$. Since we are given only a weekly average of reactor power output by the reactor company, we can only determine a weekly average rate. The total number of $\bar{\nu_e}$ detected at detector j can be expressed as,

$$\begin{aligned} N_j &= \sum_k \sum_l R_{jk} \Delta t_l \\ &= \sum_k \sum_l T_j \epsilon_j \bar{F}_k \frac{\bar{P}_{ee,jk}}{4\pi L_{jk}^2} \Delta t_l \end{aligned}$$

where l denotes week number and Δt_l is the live time in week l.

The expected numbers of $\bar{\nu_e}$ events without oscillation can be estimated and are summarized in the following table:

	DYB AD1	DYB AD2	LA AD1	Far AD1	Far AD2	Far AD3
Expected number of $\bar{\nu_e}$	28248.1	28680.2	21986	3557.53	3559.94	3526.5
Measured $\bar{\nu_e}$ candidates	28692	28857	22169	3536	3464	3461

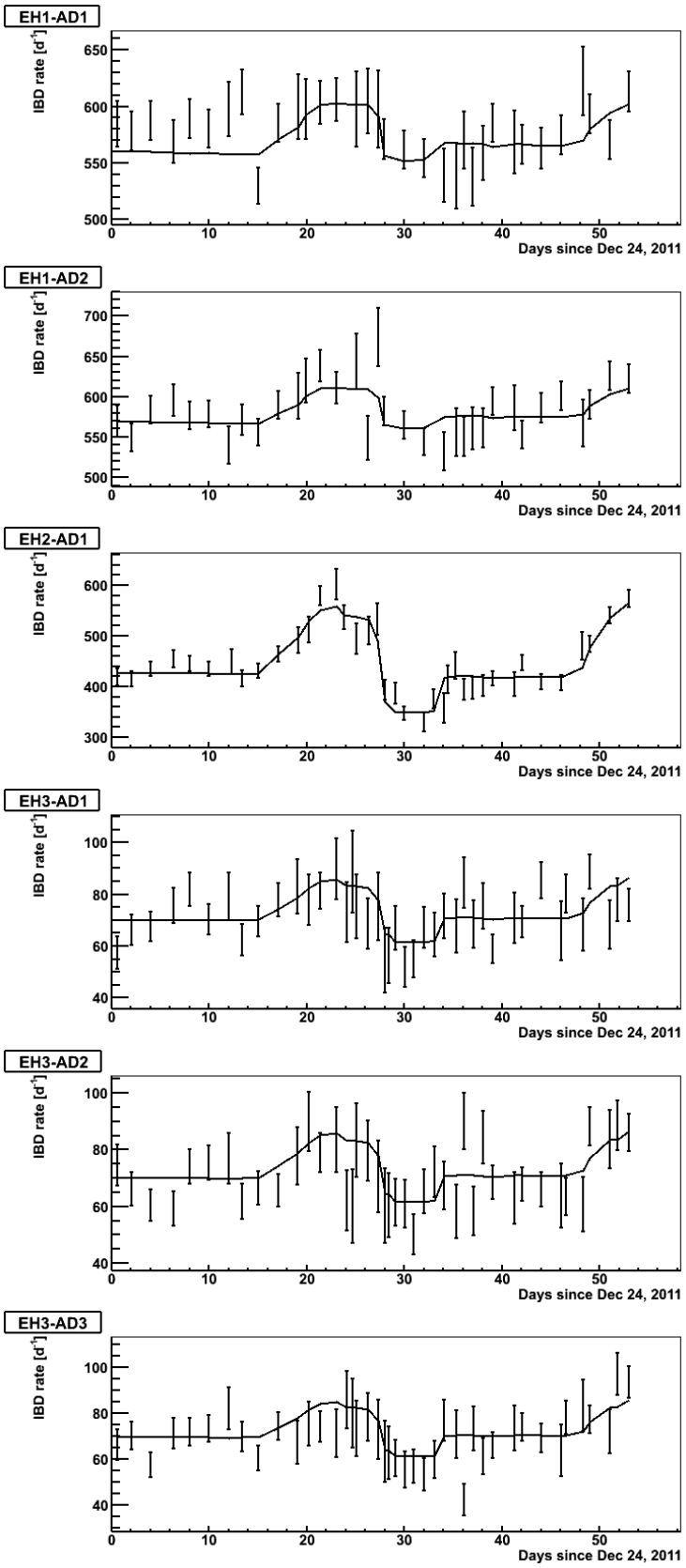

Figure 10.1: Expected (shown as line) and measured (shown as markers) IBD rates over time.

10.2 Rate-only θ_{13} Analysis

10.2.1 Model

The basis of the model is the Gaussian likelihood function:

$$\chi^2(\theta) = \sum_{j}^{\text{Detectors}} \frac{(N_j^{\text{obs}} - N_j^{\text{exp}}(\theta) - B_j)^2}{(\sigma_j^{\text{obs}})^2 + (\sigma_j^B)^2}$$

where N_j^{obs} is the observed $\bar{\nu_e}$ rate at detector j, $N_j^{\text{exp}}(\theta)$ is the expected $\bar{\nu_e}$ rate at detector j for a given θ, B_j is the background rate at detector j, σ_j^{obs}) is the uncertainty in N_j^{obs} and σ_j^B is the uncertainty in B_j.

To account for the systematic uncertainties, the rates are modified to include some penalty terms (δ) as follows:

$$\tilde{R}_{jk} = R_{jk}(1 + \delta^{\text{norm}}\sigma^{\text{norm}})(1 + \delta^{\text{eff}}\sigma^{\text{eff}})(1 + \delta_j^{\text{target}}\sigma_j^{\text{target}})(1 + \delta^{\text{flux}_k}\sigma_k^{\text{flux}})$$

where σ^{eff} is the uncertainty in detection efficiency, σ_j^{target} is the uncertainty in target mass of detector j, σ_k^{flux} is the uncertainty in flux from reactor core k, σ^{norm} is the uncertainty in overall flux and the δ's are the corresponding penalty terms.

Likewise, the backgrounds are also modified:

$$\tilde{B}_j = B_j(1 + \delta^B\sigma_j^B)$$

The expected number of detected $\bar{\nu_e}$ becomes:

$$\tilde{N_j^{\text{exp}}} = \sum_l \sum_k \tilde{R_{jk}}\Delta t_l$$

Penalty terms (δ_m^{osc}) for other oscillation parameters are also included to account for their uncertainties. All of these penalty terms are added to the likelihood function and are allowed to vary. Now the model becomes,

$$\chi^2(\theta) = \sum_{j}^{\text{Detectors}} \frac{(N_j^{\text{obs}} - \tilde{N}_j^{\text{exp}}(\theta) - \tilde{B}_j)^2}{(\sigma_j^{\text{obs}})^2 + (\sigma_j^B)^2} + \chi^2_{\text{penalty}}$$

where

$$\chi^2_{\text{penalty}} \equiv (\delta^{\text{eff}})^2 + (\delta^B)^2 + \sum_j (\delta_j^{\text{target}})^2 + \sum_k (\delta_k^{\text{flux}})^2 + \sum_m (\delta_m^{osc})^2$$

Notice that δ^{norm} is not included in χ^2_{penalty} since it represents overall flux normalization. To make a relative measurement, δ^{norm} is allowed to vary unconstrained.

10.2.2 Results

The fit to this model using MINUIT shows that $sin^2 2\theta_{13} = 0.092 \pm 0.017$, with $\chi^2_{min}/ndf = 2.21/4$ and a p-value of 0.697. The best fit values are tabulated below:

$sin^2 2\theta_{13}$	0.0920823 ± 0.0169349		
δ^{norm}	0.219966 ± 0.888893		
δ^B	-0.00649651 ± 0.981296	δ_1^{flux}	-0.0949647 ± 0.936669
δ^{eff}	-0.00089939 ± 0.982688	δ_2^{flux}	-0.0939421 ± 0.934799
δ^{target}	$-0.000215358 \pm 0.981614$	δ_3^{flux}	0.0386323 ± 0.97416
$sin^2 2\theta_{12}$	0.00023398 ± 0.99652	δ_4^{flux}	0.0373293 ± 0.974754
Δm^2_{31}	0.000383165 ± 0.217099	δ_5^{flux}	0.0500322 ± 0.96886
Δm^2_{21}	0.000216072 ± 0.981585	δ_6^{flux}	0.0630689 ± 0.961314

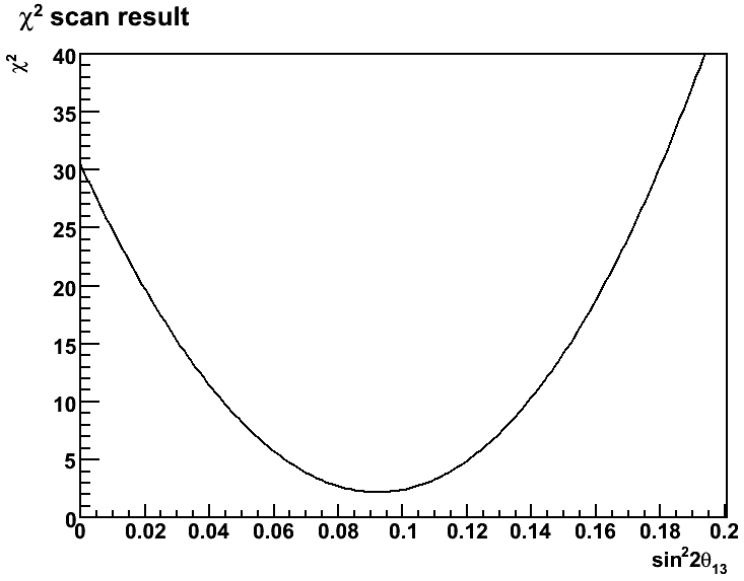

Figure 10.2: Chi-square plot for nearby $sin^2 2\theta_{13}$ values.

Chapter 11

Summary and prospects

The Daya Bay Reactor Neutrino Experiment has measured $sin^2 2\theta_{13}$ to an unprecedented precision, using 55 days of data obtained from six 2.9 GW_{th} reactor cores. The value of $sin^2 2\theta_{13}$ has been measured to be:

$$sin^2 2\theta_{13} = 0.092 \pm 0.017(\text{stat}) \pm 0.004(\text{syst})$$

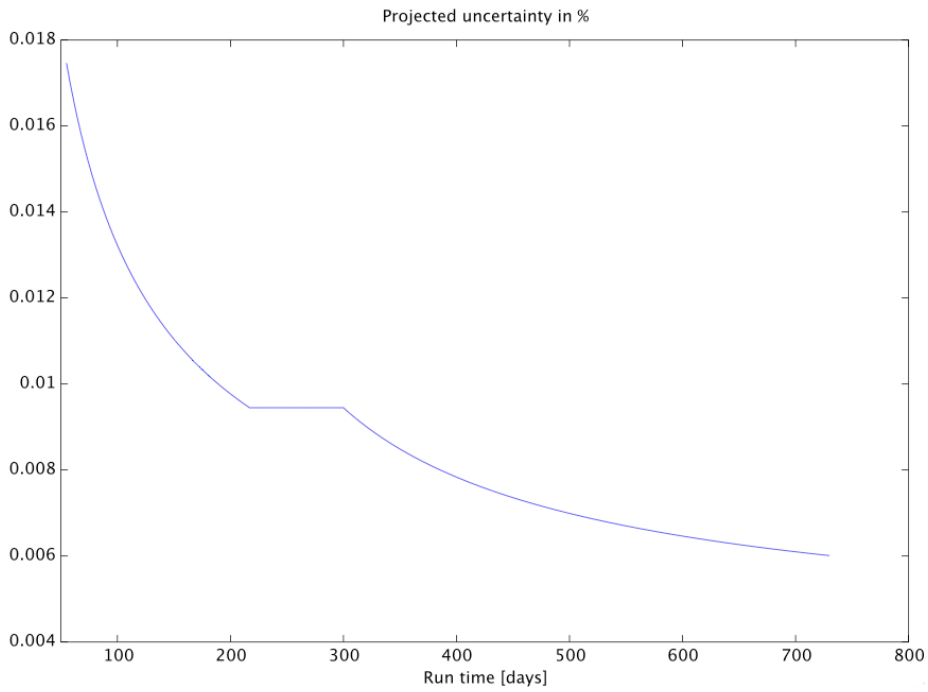

Figure 11.1: Projected uncertainty in $sin^2 2\theta_{13}$ over two years of total run time assuming no improvements in systematic uncertainties. The plateau from day 217 to day 300 is due to the temporary shutdown during the installation of the remaining 2 ADs (Jul 28, 2012 to Oct 19, 2012) and the data taking rate is assumed to increase by 33% after that.

In the current analysis, statistical uncertainty still dominates. With increased statistics, the uncertainty will be further reduced to about 0.006% when two years of total run time has been accumulated. At that point, systematic uncertainty becomes more important. Better understanding of the systematics and shape analysis are necessary to further improve the precision.

11.1 Future Prospects

The neutrino mass hierarchy and the value of δ_{CP} still remain unknown. With this relatively large value of θ_{13}, experiments aimed at resolving thse two puzzles become feasible. There are a number of proposed experiments with the goal of resolving the mass hierarchy and/or measuring δ_{CP}. Here I will describe a possible extension of Daya Bay. Daya Bay II is a proposed experiment aimed at resolving the mass hierarchy in addition to further improve the precision of the known mixing parameters [33, 114]. There will possibly be a new 20-50 kton LS detector, located several tens of kilometers from various reactor complexes along the southern coast of China. Daya Bay II would attempt to observe disappearance of $\bar{\nu}_e$. The survival probability of $\bar{\nu}_e$ can be written as,

$$P(\bar{\nu}_e \to \bar{\nu}_e) = 1 - 4s^2_{13}c^2_{13}(c^2_{12}sin^2\Delta_{31} + s^2_{12}sin^2\Delta_{32}) - 4c^4_{13}s^2_{12}c^2_{12}sin^2\Delta_{21}$$

where $s_{ij} = sin\theta_{ij}$, $c_{ij} = cos\theta_{ij}$ and $\Delta_{ij} = \Delta m^2_{ij}\frac{L}{E}$. Figure 11.2 shows the survival probability of $\bar{\nu}_e$ as a function of $\frac{L}{E}$. We can see that the difference in oscillation pattern between normal hierarchy and inverted hierarchy is tiny. Considering the finite energy resolution of the detector and its non-linearity in energy response, the "wiggles" could be smeared out, further reducing our ability to distinguish the two scenarios. Moreover, the uncertainty in $|\Delta m^2_{32}|$ could even create a degeneracy, meaning that the two hierarchy scenarios each coupled with different values of $|\Delta m^2_{32}|$ would create (statistically) identical spectra that are indistinguishable given limited statistics. With optimal placement of the detectors and better understanding of the detector response, these challenges can, hopefully, be overcome.

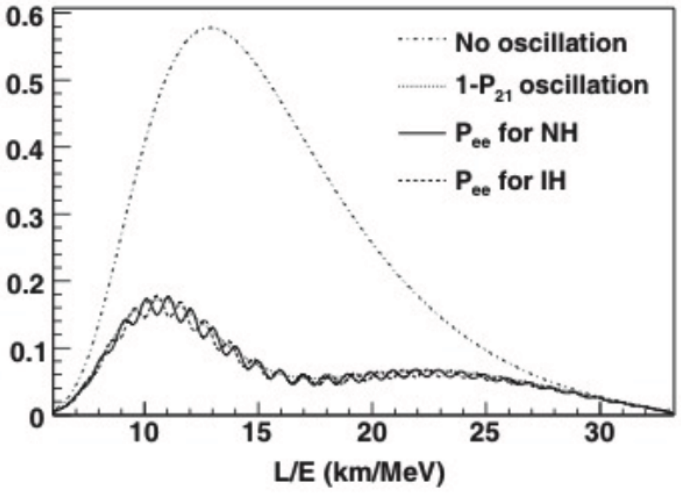

Figure 11.2: Survival probability of $\bar{\nu}_e$. [33]

Bibliography

[1] F. Boehm and P. Vogel, *Physics of Massive Neutrinos*, Cambridge University Press, 2nd edition, 1992.

[2] The Reines-Cowan Experiments: Detecting the Poltergeist, *Los Alamos Science*, (25), 1997.

[3] J. N. Bahcall, A. M. Serenelli, and S. Basu, New solar opacities, abundances, helioseismology, and neutrino fluxes, *Astrophys. J.*, 621(L85-L88), 2005.

[4] H. Kwon et al., Search for neutrino oscillations at a fission reactor, *Phys. Rev. D*, 24(1097-1111), 1981.

[5] Yu. V. Kozlov et al., Antineutrino deuteron experiment at Krasnoyarsk reactor, *Phys. Atom. Nucl.*, 63:1016–1019, 2000.

[6] M. Apollonio et al., Limits on neutrino oscillations from the CHOOZ experiment, *Phys. Lett. B*, 466:415–430, 1999.

[7] F. Boehm et al., Search for Neutrino Oscillations at the Palo Verde Nuclear Reactors, *Phys. Rev. Lett.*, 84:3764–3767, 2000.

[8] Y. Fukuda et al., Evidence for oscillation of atmospheric neutrinos, *Phys. Rev. Lett.*, 81:1562–1567, 1998.

[9] J. Boger et al., The Sudbury Neutrino Observatory, *Nucl. Instrum. Meth. A*, 449:172–207, 2000.

[10] Q. R. Ahmad et al., Direct evidence for neutrino flavor transformation from neutral current interactions in the Sudbury Neutrino Observatory, *Phys. Rev. Lett.*, 89(011301), 2002.

[11] G. L. Fogli et al., Getting the most from the statistical analysis of solar neutrino oscillations, *Phys. Rev. D*, 66(053010), 2002.

[12] KamLAND website, http://kamland.lbl.gov/Detector/.

[13] K. Eguchi et al., First Results from KamLAND: Evidence for Reactor Anti-Neutrino Disappearance, *Phys. Rev. Lett.*, 90(021802), 2003.

[14] S. Abe et al., Precision Measurement of Neutrino Oscillation Parameters with KamLAND, *Phys. Rev. Lett.*, 100(221803), 2008.

[15] M. H. Ahn et al., Measurement of Neutrino Oscillation by the K2K Experiment, *Phys. Rev. D*, 74(072003), 2006.

[16] P. Adamson et al., Measurement of the neutrino mass splitting and flavor mixing by MINOS, *Phys. Rev. Lett.*, 106(181801), 2011.

[17] K. Abe et al., Indication of Electron Neutrino Appearance from an Accelerator-produced Off-axis Muon Neutrino Beam, *Phys. Rev. Lett.*, 107(041801), 2011.

[18] K. Abe et al., Evidence of Electron Neutrino Appearance in a Muon Neutrino Beam, *arXiv:1304.0841 [hep-ex]*, 2013.

[19] P. Vogel and J. F. Beacom, The angular distribution of the reaction $\bar{\nu}_e + p \to e^+ + n$, *Phys. Rev. D*, 60(053003), 1999.

[20] J. K. Ahn et al., RENO: An Experiment for Neutrino Oscillation Parameter $theta_{13}$ Using Reactor Neutrinos at Yonggwang, *arXiv:1003.1391 [hep-ex]*, 2010.

[21] United States Nuclear Regulatory Commission, Pressurized Water Reactors, http://www.nrc.gov/reactors/pwrs.html.

[22] H. R. Band et al., Target Mass Monitoring and Instrumentation in the Daya Bay Antineutrino Detectors, *arXiv:1206.7082 [physics.ins-det]*, 2012.

[23] Z. Yu, PMT Gain Calibration TechNote, *Daya Bay Doc-7093*, 2012.

[24] Z. Wang, RollingGain Note, *Daya Bay Doc-7198*, 2011.

[25] X. Qian et al., Summary of Flasher Events Rejection, *Daya Bay Doc-7434*, 2012.

[26] L. Wen et al., Full control of the flashers, *Daya Bay Doc-7143*, 2011.

[27] Y. Nakajima, Vertex reconstruction using charge templates for AdSimple reconstruction package, *Daya Bay Doc-7536*, 2012.

[28] F. P. An et al., A side-by-side comparison of Daya Bay antineutrino detectors, *Nucl. Instrum. Meth. A*, 685:78–97, 2012.

[29] Z. Yu et al., Energy Calibration/Reconstruction, *Daya Bay Doc-7418*, 2011.

[30] F. Ajezenberg-Selove, Energy levels of light nuclei A, *Nuclear Physics A490 1 (1988)*, 1988.

[31] W. Gu and J. Liu, AmC background note, *Daya Bay Doc-6779*, 2012.

[32] X. Qian, Investigation of ACU single Neutron Rate, *Daya Bay Doc-7950*, 2012.

[33] C. Zhang, Daya Bay II, http://www.phy.bnl.gov/.

[34] V. I. Kopeikin et al., Reactor as a source of antineutrinos: Thermal fission energy, *Physics of Atomic Nuclei*, 67(10):1892, 2004.

[35] J. Cao, Baselines for EH1-2-3 from Survey, *Daya Bay Doc-7637*, 2012.

[36] J. Beringer et al. (Particle Data Group), The Number of Light Neutrino Types from Collider Experiments, *Phys. Rev. D*, 86(010001), 2012.

[37] K. Zuber, *Neutrino Physics*, CRC Press, 2nd edition, 2012.

[38] L. Wolfenstein, Neutrino oscillations in matter, *Phys. Rev. D*, 17(2369), 1978.

[39] B. Kayser, Lecture 4: Neutrino Physics, *SLAC Summer Institute on Particle Physics 2004 (SSI04)*, 2004.

[40] J. N. Bahcall, M. H. Pinsonneault, and S. Basu, Solar Models: Current Epoch and Time Dependences, Neutrinos, and Helioseimological Properties, *Astrophys. J.*, 555:990–1012, 2001.

[41] J. Chadwick, *Verh. d. deutschen Phys. Ges.*, 16:383, 1914.

[42] E. Fermi, *Ricercha Scient.*, 2:12, 1933.

[43] E. Fermi, *Z. Physik*, 88:161, 1934.

[44] F. Reines and C. L. Cowan, Detection of the free neutrino, *Phys. Rev.*, 92:830–831, 1953.

[45] F. Reines and C. L. Cowan, The Neutrino, *Nature*, 178:446, 1956.

[46] B. T. Cleveland et. al., Measurement of the Solar Electron Neutrino Flux with the Homestake Chlorine Detector, *Astrophysical Journal*, 496:505–526, 1998.

[47] G. Zacek et al., Neutrino oscillation experiments at the Gösgen nuclear power reactor., *Phys. Rev., D*, 34:2621–2636, 1986.

[48] A. I. Afonin et al., Anti-electron-neutrino spectra at two distances from the reactor of the Rovno nuclear power plant: Search for oscillations., *JETP Lett.*, 45:247–251, 1987.

[49] S. N. Ketov et al., Reactor experiments of a new type to detect neutrino oscillations., *JETP Lett.*, 55:564–568, 1992.

[50] J. F. Cavaignac et al., Indication for neutrino oscillation from a high statistics experiment, *Phys. Lett., B*, 148:387–394, 1984.

[51] Y. Declais et al., Search for neutrino oscillations at 15-meters, 40-meters, and 95-meters from a nuclear power reactor at Bugey, *Nucl. Phys., B*, 434:503–534, 1995.

[52] K. S. Hirata et al., Real time, directional measurement of B-8 solar neutrinos in the Kamiokande-II detector, *Phys. Rev. D*, 44:2241–2260, 1991.

[53] Y. Fukuda et al., Solar neutrino data covering solar cycle 22, *Phys. Rev. Lett.*, 77:1683–1686, 1996.

[54] D. A. Dwyer, *Precision Measurement of Neutrino Oscillation Parameters with KamLAND*, PhD thesis, University of California, Berkeley, 2007.

[55] M. Apollonio et al., Initial results from the CHOOZ long baseline reactor neutrino oscillation experiment, *Phys. Lett., B*, 420:397–404, 1998.

[56] F. Boehm et al., Final results from the Palo Verde neutrino oscillation experiment, *Phys. Rev., D*, 64(112001), 2001.

[57] F. Boehm et al., Results from the Palo Verde Neutrino Oscillation Experiment, *Phys. Rev. D*, 62(072002), 2000.

[58] Y. Fukuda et al., Measurements of the solar neutrino flux from Super- Kamiokande's first 300 days, *Phys. Rev. Lett.*, 81:1158–1162, 1998.

[59] S. Fukada et al., Constraints on neutrino oscillations using 1258 days of Super-Kamiokande solar neutrino data., *Phys. Rev. Lett.*, 86:5656–5660, 2001.

[60] S. Fukuda et al., Determination of solar neutrino oscillation parameters using 1496 days of Super-Kamiokande-I data, *Phys. Lett. B*, 539:179–187, 2002.

[61] M. B. Smy et al., Precise measurement of the solar neutrino day/night and seasonal variation in Super-Kamiokande-I, *Phys. Rev. D*, 69(011104), 2004.

[62] J. Hosaka et al., Solar neutrino measurements in Super-Kamiokande-I, *Phys. Rev. D*, 73(112001), 2006.

[63] Q. R. Ahmad et al., Measurement of the charged current interactions produced by B-8 solar neutrinos at the Sudbury Neutrino Observatory., *Phys. Rev. Lett.*, 87(071301), 2001.

[64] Q. R. Ahmad et al., Measurement of day and night neutrino energy spectra at SNO and constraints on neutrino mixing parameters., *Phys. Rev. Lett.*, 89(011302), 2002.

[65] S. N. Ahmed et al., Measurement of the total active B-8 solar neutrino flux at the Sudbury Neutrino Observatory with enhanced neutral current sensitivity., *Phys. Rev. Lett.*, 92(181301), 2004.

[66] B. Aharmim et al., Electron energy spectra, fluxes, and day-night asymmetries of B-8 solar neutrinos from the 391-day salt phase SNO data set., *Phys. Rev., C*, 72(055502), 2005.

[67] K. Eguchi et al., A High Sensitivity Search for $\bar{}_e$'s from the Sun and Other Sources at KamLAND, *Phys. Rev. Lett.*, 92(071301), 2004.

[68] T. Araki et al., Measurement of Neutrino Oscillation with KamLAND: Evidence of Spectral Distortion, *Phys. Rev. Lett.*, 94(081801), 2005.

[69] A. Suzuki et al., Design, construction, and operation of SciFi tracking detector for K2K experiment, *Nucl. Instrum. Meth. A*, 453:165–176, 2000.

[70] S. H. Ahn et al., Detection of Accelerator-Produced Neutrinos at a Distance of 250 km, *Phys. Lett. B*, 511:178–184, 2001.

[71] M. H. Ahn et al., Indications of Neutrino Oscillation in a 250 km Long-baseline Experiment, *Phys. Rev. Lett.*, 90(041801), 2003.

[72] M. H. Ahn et al., Search for Electron Neutrino Appearance in a 250 km Long-baseline Experiment, *Phys. Rev. Lett.*, 93(051801), 2004.

[73] E. Aliu et al., Evidence for muon neutrino oscillation in an accelerator-based experiment, *Phys. Rev. Lett.*, 94(081802), 2005.

[74] D. G. Michael et al., Observation of muon neutrino disappearance with the MINOS detectors and the NuMI neutrino beam, *Phys. Rev. Lett.*, 97(191801), 2006.

[75] P. Adamson et al., Measurement of Neutrino Oscillations with the MINOS Detectors in the NuMI Beam, *Phys. Rev. Lett.*, 101(131802), 2008.

[76] M. Apollonio et al., Search for neutrino oscillations on a long base-line at the CHOOZ nuclear power station, *Eur. Phys. J. C*, 27:331–374, 2003.

[77] Y. Declais et al., Study of reactor anti-neutrino interaction with proton at Bugey nuclear power plant, *Phys. Lett. B*, 338:383, 1994.

[78] J. K. Ahn et al., Observation of Reactor Electron Antineutrino Disappearance in the RENO Experiment, *Phys. Rev. Lett.*, 108(191802), 2012.

[79] Z. Djurcic et al., Uncertainties in the anti-neutrino production at nuclear reactors, *J. Phys. G.*, 36(045002), 2009.

[80] J. Cao, Determining Reactor Neutrino Flux, *Nucl. Phys. B Proc. Suppl.*, 229–232:205–209, 2012.

[81] S. Rauck, SCIENCE V2 nuclear code package - qualification report (Rev A), *Framatome ANP Document*, NFPSD/DC/89(14), 2004.

[82] R. Sanchez et al., APOLLO2 Year 2010, *Nucl. Eng. Tech.*, 42(474), 2010.

[83] R. R. G. Marleau, A. Hebert, and R. Roy, A User Guide for DRAGON, Report IGE-236 Rev. 1, 2001.

[84] W. G. K. Schreckenbach et al., Determination of the antineutrino spectrum from ^{235}U thermal neutron fission products up to 9.5 MeV, *Phys. Lett. B*, 160B:325, 1985.

[85] A. F. von Feilitzsch and K. Schreckenbach, Experimental beta-spectra from ^{239}Pu and ^{235}U thermal neutron fission products and their correlated antineutrino spectra, *Phys. Lett. B*, 118:162, 1982.

[86] A. A. Hahn et al., Antineutrino spectra from ^{241}Pu and ^{239}Pu thermal neutron fission products, *Phys. Lett. B*, 218:365, 1989.

[87] B. Achkar et al., Comparison of anti-neutrino reactor spectrum models with the Bugey 3 measurements, *Phys. Lett. B*, 374:243–248, 1996.

[88] P. Huber, Determination of antineutrino spectra from nuclear reactors, *Phys. Rev. C*, 84(024617), 2011.

[89] P. Vogel et al., Reactor antineutrino spectra and their application to antineutrino-induced reactions. II, *Phys. Rev. C*, 24:1543–1553, 1981.

[90] T. Mueller et al., Improved predictions of reactor antineutrino spectra, *Phys. Rev. C*, 83(054615), 2011.

[91] F. P. An et al., Systematic impact of spent nuclear fuel on θ_{13} sensitivity at reactor neutrino experiment, *Chin. Phys. C*, 33:711, 2009.

[92] B. Zhou et al., A study of antineutrino spectra from spent nuclear fuel at Daya Bay, *Chin. Phys. C*, 36:1, 2012.

[93] J. Cao et al., Update on Baselines for 6 ADs And Spent Pool Locations, *Daya Bay Doc-8432*, 2012.

[94] G. Giacomelli and A. Margiotta, The MACRO Experiment at Gran Sasso, *arXiv:0707.1691 [hep-ex]*, 2007.

[95] D. Passmore et al., Testing and Characterizing Load Cells for the AD Target Mass Measurement, *Daya Bay Doc-2203*, 2008.

[96] J. Liu et al., Automated Calibration System for a High-Precision Measurement of Neutrino Mixing Angle θ_{13} with the Daya Bay Antineutrino Detectors, *arXiv:1305.2248 [physics.ins-det]*, 2013.

[97] J. Cherwinka et al., AD Survey Results, *Daya Bay Doc-5819*, 2011.

[98] S. Jetter, AD trigger efficiencies from ^{68}Ge source data, *Daya Bay Doc-7477*, 2012.

[99] E. H. Bellamy et al., Absolute calibration and monitoring of a spectrometric channel using a photomultiplier, *Nucl. Instrum. Meth. A*, 339:468–476, 1994.

[100] L. Lebanowski, FEE Coarse Range Gain Calibration, *Daya Bay Doc-7408*, 2012.

[101] Z. Wang, Pedestal, *Daya Bay Doc-5362*, 2010.

[102] G. Cao, Relative Quantum Efficiency, *Daya Bay Doc-7317*, 2011.

[103] F. P. An et al., Observation of electron-antineutrino disappearance at Daya Bay, *Phys. Rev. Lett.*, 108(171803), 2012.

[104] Z. Yu et al., Anti-neutrino Detector Energy Response, *Daya Bay Doc-7314*, 2011.

[105] C-J Lin et al., The AdSimple Reconstruction, *Daya Bay Doc-7334*, 2012.

[106] D. Dwyer et al., Energy Scale Calibration with Spallation Neutrons, *Daya Bay Doc-7463*, 2012.

[107] C. Zhang, Theta13 Oscillation Analysis, *Daya Bay Doc-7621*, 2012.

[108] X. Qian et al., Double Check of Flasher Cut Efficiency, *Daya Bay Doc-7677*, 2012.

[109] D. R. Tilley et al., Energy levels of light nuclei A = 8, 9, 10, *Nucl. Phys. A*, 745:155–362, 2004.

[110] X. Qian et al., Some Discussions about Event's Timing Separation, *Daya Bay Doc-7278*, 2011.

[111] J. Ling and X. Qian, Fast Neutron study with P12A+P12B data, *Daya Bay Doc-7539*, 2012.

[112] F. Wu and X. Qian, Estimation of Correlated Bg from ACUs, *Daya Bay Doc-7568*, 2012.

[113] Z. Yu et al., Alpha-n background study, *Daya Bay Doc-7509*, 2012.

[114] X. Qian et al., Mass Hierarchy Resolution in Reactor Anti-neutrino Experiments: Parameter Degeneracies and Detector Energy Response, *arXiv*, (1208.1551v2), 2012.

[115] Q-J Li et al., Front-End Electronics System of PMT Readout for Daya Bay Reactor Neutrino Experiment, *IEEE*, N25(240), 2009.

[116] B. Pontecorvo, Neutrino Experiments and the Problem of Conservation of Leptonic Charge, *Zh. Eksp. Teor. Fiz.*, 53:1717, 1957.

[117] J. Liu et al., Gamma-less and Low Rate Neutron Source for the Daya Bay Experiment, *in preparation*, 2013.

[118] J. S. Kapustinsky et al., A fast timing light pulser for scintillation detectors, *Nucl. Instrum. Meth. A*, 241:612–613, 1985.

[119] National Instruments, http://www.ni.com.

[120] J. Goett et al., Optical attenuation measurements in metal-loaded liquid scintillators with a long-pathlength photometer, *Nucl. Instrum. Meth. A*, 637:47–52, 2011.

[121] P. Adamson et al. (MINOS Collaboration), Improved search for muon-neutrino to electron-neutrino oscillations in MINOS, *Phys. Rev. Lett.*, 107(181802), 2011.

[122] R. D. McKeown and P. Vogel, Neutrino Masses and Oscillations: Triumphs and Challenges, *Phys. Rept.*, 394:315–356, 2004.

[123] C. Zhang, Absolute IBD Efficiency - IBD MC Revisited, *Daya Bay Doc-7548*, 2012.

[124] W. R. Leo, *Techniques for Nuclear and Particle Physics Experiments: A How-to Approach*, Springer-Verlag, 2nd revised edition, 1994.

[125] G. F. Knoll, *Radiation Detection and Measurement*, Wiley, 3rd edition, 2000.

[126] L. Lebanowski, An energy non-linearity overview, *Daya Bay Doc-8798*, 2013.

[127] D. W. K. Ngai et al., A Summary of PMT Test at DGUT during August - September 2008, *Daya Bay Doc-2721*, 2008.

[128] Z. Wang L. Lebanowski, AD PMT saturation and linearity measurements, *Daya Bay Doc-5562*, 2010.

[129] L. Lebanowski and W. Zhong, PMT & FEE Linearity Update, *Daya Bay Doc-6605*, 2011.

[130] X. Wang, *A Design Study of the Trigger System for Daya Bay Reactor Neutrino Experiment*, PhD thesis, Tsinghua University, 2011.

[131] H. Gong et al., Design of the Local Trigger Board for the Daya Bay Reactor Neutrino Experiment, *Nucl. Instrum. Meth. A*, 637:138–142, 2011.

[132] F. Li et al., DAQ Architecture Design of Daya Bay Reactor Neutrino Experiment, *IEEE Transactions on nuclear science*, 58(4):1723, 2011.

[133] X. Guo et al., A precision measurement of the neutrino mixing angle θ_{13} using reactor antineutrinos at Daya Bay, *arXiv*, (hep-ex/0701029), 2007.

[134] E. Majorana, Teoria simmetrica dell'elettrone e del positrone, *Nuovo Cimento*, 14(171), 1937.

[135] F. Ardellier et al., Double Chooz: A Search for the Neutrino Mixing Angle θ_{13}, *arXiv:hep-ex/0606025*, 2006.

[136] Y. Abe et al., Reactor electron antineutrino disappearance in the Double Chooz experiment, *Phys. Rev. D*, 86(052008), 2012.

[137] R. A. Dunlap, *The Physics of Nuclei and Particles*, Thomson, 2004.

[138] J. N. Bahcall and M. H. Pinsonneault, What do we (not) know theoretically about solar neutrino fluxes?, *Phys. Rev. Lett. 92 (2004)*, 92(121301), 2004.

[139] J. N. Bahcall, Solar Models and Solar Neutrinos: Current Status, *Phys. Scripta*, T121:46–50, 2005.

[140] Z. Maki, M. Nakagawa, and S. Sakata, Remarks on the Unified Model of Elementary Particles, *Prog. Theor. Phy.*, 28(5):870–880, 1962.

[141] B. Pontecorvo, Mesonium and anti-mesonium, *Zh. Eksp. Teor. Fiz.*, 33:549–551, 1957.

[142] G. Danby et al., Observation of high-energy neutrino reactions and the existence of two kinds of neutrinos, *Phys. Rev. Lett.*, 9(1):36–44, 1962.

[143] B. Pontecorvo, Electron and muon neutrinos, 1960, In K. Winter, editor, *Neutrino Physics*, Cambridge University Press, 2000.

[144] W. Pauli, On the earlier and more recent history of the neutrino, 1957, In K. Winter, editor, *Neutrino Physics*, Cambridge University Press, 2000.

[145] L. Meitner, *Z. Physik*, 9, 11, 35, 101, 145, 1922.

[146] C. D. Ellis, *Proc. Roy. Soc. (A)*, 101(1), 1922.